Dissertation
submitted to the
Combined Faculties for the Natural Sciences and for Mathematics
of the Ruperto-Carola University of Heidelberg, Germany
for the degree of
Doctor of Natural Sciences

presented by
Diplom-Physicist Alessandro Berton
born in Castelfranco Veneto, Italy
Oral examination: December 13^{th} 2006

Detecting Extrasolar Planets using IFS-based Simultaneous Differential Imaging

Referees: Prof. Dr. Thomas Henning
Prof. Dr. Reinhard Mundt

Zusammenfassung

Beobachtungen extrasolarer Planeten mit Integral Field Spectroscopy (IFS), in Verbindung mit extremer adaptiven Optik und der Simultaneous Differential Imaging (SDI) Methode, sind bestens geeignet, um Planeten direkt zu detektieren und zu charakterisieren; Sie verbessern das detektierte Signal des Planeten, während sie gleichzeitig den Einfluß des Sternenlichts und wichtiger Rauschquellen, wie z.B. Speckles, reduzieren. Um die Wirksamkeit einer solchen Methode zu untersuchen, wurde ein Simulationsprogramm entwickelt, das die Leistungfähigkeit der IFS-SDI Methode für verschiedene Typen von extrasolaren Planeten und Teleskopen testet. Hierzu wurden verschiedene atmosphärische und instrumentelle Rauschquellen modelliert. Das angewandte Verfahren für die Simulation der IFS Beobachtungen wird im Folgenden detailliert dargestellt. Speziell wird erläutert wie Abschätzungen für Speckle-Rauschen, Korrekturen der adaptiven Optik und spezielle instrumentelle Eigenschaften abgeleitet wurden, und wie die Effizienz der SDI Methode zur Verbesserung des Signal-zu-Rauschen Verhältnisses bei der Planetensuche getestet wurde. Die ersten Ergebnisse der Simulationen zeigen, daß zahlreiche Detektionen extrasolarer Planeten in der Tat zu erwarten sind, selbst wenn man bestehende 8m-Teleskope mit wenigen Stunden Belichtungszeit nutzt. In einer weiteren Analyse wird abgeschätzt, welche Auswirkung ein extrem grosser Teleskopdurchmesser auf die Detektion von extrasolaren Planeten mit IFS-SDI hat.

Abstract

Observations of extrasolar planets using Integral Field Spectroscopy (IFS), if coupled with an extreme Adaptive Optics system and analyzed with a Simultaneous Differential Imaging technique (SDI), are a powerful tool to detect and characterize planets directly; they enhance the signal of the planet and, at the same time, reduces the impact of stellar light and consequently important noise sources like speckles. In order to verify the efficiency of such a technique, we developed a simulation code able to test the capabilities of this IFS-SDI technique for different kinds of planets and telescopes, modelling the atmospheric and instrumental noise sources. The procedure adopted to simulate IFS observations is presented here in detail, explaining in particular how we obtain estimates of the speckle noise, Adaptive Optics corrections, specific instrumental features, and how we test the efficiency of the SDI technique to increase the signal-to-noise ratio of the planet detection. The first results obtained by the simulations show that many significant extrasolar planet detections are indeed possible using the present 8m-class telescopes within a few hours of exposure time. Furthermore, we provide here an estimation on the impact of extremely large telescope diameters on the detection of planets with IFS-SDI.

Contents

Introduction

In the last years the search of extra solar planets has become one of the most important and active branches of astronomy. The detection of a new Earth, around a star other than the Sun, was always one of the dreams of the astronomers, but only now it starts seeming possible. The development of technology, together with the genial intuitions and the hard work of the scientists, led to new techniques that allowed, in only 10 years, the detections of around 200 Jupiter-like (down to Neptune-like) planets. This has been done mainly using the indirect observations of the perturbations to the light of the host star due to the presence of the planet. This number is going to increase continuously in the next years.

Today the scientific community, although it still recognize the extreme importance of these indirect detections, also realizes that some important informations, e.g. the temperature of the companion, the composition of its atmosphere, etc., need a direct detection to be achieved, that is, anyway, a very challenging goal to reach. To detect directly the light of a planet around a star, we have to deal with the enormous contrast between the intensities of star and companion. To resolve the planet, and to distinguish it among the various noises, a very large telescope and an extremely efficient Adaptive Optic system (AO) is probably not enough. Other tricks are required to reduce the noise and make the planet finally visible.

In the work presented here we analyzed in detail a specific method, hereafter called IFS-SDI (Integral Field Spectroscopy - Simultaneous Differential Imaging), that combines together the 3-D information given by integral field spectroscopy and the differential imaging at various wavelength, to enhance the signal of the planets. The method is studied in relation to the specific case of SPHERE (Dohlen et al., 2006) at VLT, but can be applied to every kind of large telescope or extremely large telescope (ELT, diameter $D \geq 20\,\mathrm{m}$). The goal of this work was to use detailed numerical simulations to understand what advantages IFS-SDI provides if compared with other techniques for planetary detection, in particular the dual-band differential imaging; moreover, we wanted to see how deep we can go with detections, assuming the possibility of using telescopes 20, 30, 50 or even 100 m wide, to finally estimate whether the dream of the Earth-like planet detection is feasible or not.

After a short introduction to some general physical properties of low mass companions (brown dwarfs and planets, Chapter 1), in this thesis we present the most important techniques used up to now for detection of planets, divided in two groups: indirect methods (Chapter 2) and direct methods (Chapter 3). The IFS-SDI technique is discussed in detail in Chapter 4. In Chapter 5 the software we developed to simulate IFS-SDI observations is briefly presented, while in the following chapters the results of simulations are presented and discussed, in detail for the 8 m class telescope case (Chapter 6), more in general for the cases of larger diameters (ELTs, Chapter 7).

Finally, results are discussed in a general conclusion.

Chapter 1

General properties of very low mass companions

Since the main goal of this study is the detection and characterization of faint companions of apparently bright stars, it is important to define in detail which are the various classes of objects that will be the target of the search. Generally, we can divide the family of low mass companions in Brown Dwarfs (hereafter BDs), warm planets and cold planets.

1.1 Definition of Brown Dwarf

BDs are intermediate mass objects, that can be defined basing on their mass, which is included between the deuterium-burning limit (13 M_J) and the hydrogen-burning limit (73 M_J , around 0.08 $M_\odot$). This definition shows that a BD is able to produce energy by thermonuclear reactions (deuterium and lithium) but it cannot reach the temperature and density needed for burning hydrogen in the main sequence: so, it is not a star. A more physical definition distinguish then BDs from planets because they form in the same way as stars through the collapse of molecular clouds, while planets form by coagulation processes in accretion disks surrounding young stars. It is, anyway, unclear if the two classes overlap. The general properties of Brown Dwarfs are described in detail in the reviews made by Allard et al. (1997), Chabrier & Baraffe (2000) and Burrows et al. (2001).

Secondary BDs close to their parent stars are already within reach of available instrumentation for targets with favorable luminosity contrast. New instruments and techniques can provide much more complete census of BDs as companions of nearby stars. Anyway, we will focus our attention in particular on planetary objects which will be the primary targets of our simulated observations.

1.2 Definition of planet

To define a planet, it is not enough to describe it as an object with a mass lower than 13 M_J . We assume in this work the definition of planet given by the IAU Working Group on Extrasolar Planets[1]:

- "Objects with true masses below the limiting mass for thermonuclear fusion of deuterium (currently calculated to be 13 Jupiter masses for objects of solar metalicity) that orbit stars or stellar remnants are 'planets' (no matter how they formed). The minimum mass/size required for an extrasolar object to be considered a planet should be the same as that used in our Solar System."
- "Substellar objects with true masses above the limiting mass for thermonuclear fusion of deuterium are 'brown dwarfs', no matter how they formed nor where they are located."
- "Free-floating objects in young star clusters with masses below the limiting mass for thermonuclear fusion of deuterium are not 'planets', but are 'sub-brown dwarfs' (or whatever name is most appropriate)."

Following this definition, any object orbiting a star with mass between a rocky planet like Mercury and the brown dwarf regime has to be called planet. But we still can distinguish different categories of planets: the warm and young planets, and the cold and old ones, are described in detail in the next paragraphs, and are differentiated by the mechanism of emission. The distinction between earth-like planets and Jupiter-like one, often used at present, is given by the mass and consequently by the gravity and the elements that compose the atmospheres.

1.2.1 Young and warm planets

We define warm planets as those objects with masses below 13 M_J for which the emitted flux is principally intrinsic thermal radiation, and with separations larger than ~0.2 AU from the host star. Closer planets, like 51 Peg b, are usually called

---

[1] *http://www.dtm.ciw.edu/boss/definition.html*

hot planets or roasters, and they have to be distinguished from the warm planets because their high temperature is due to stellar irradiation alone (Seager & Sasselov, 1998). We expect a similar number of warm planets both in wide orbits and in close-in orbits. Considering that the signal from the planet is independent from the separation, because it is intrinsic, the observation is favorable in wide orbits where noises due to the PSF of the star are less affecting the detection.

The strong intrinsic flux from warm planets depends on their young age, because they are still contracting and possibly even accreting. We expect two important phases in the life of a planet: an accretion phase, which has a very short duration (only within the first 10 million years), and a cooling phase. Planets during the accretion phase can theoretically reach luminosities larger than $10^{-3}\ L_\odot$, up to a million times brighter than the same planets at old ages; but the short duration of this phase makes them very difficult to sample. In the cooling phase the luminosity and temperature of isolated planets evolve on the cooling time scale according the rule $L \sim M^2/t$, where L is in solar luminosities, M in Jupiter masses and t in years. Therefore, the luminosity contrast star/planet is more favorable at young ages. The cooling of the planet will continue regularly with a continuous decrement of luminosity, as shown in Fig.1.1, without the ignition of thermonuclear reactions that characterize the luminosity evolution for stars and BDs.

1.2.2 Old and cold planets

Cold planets shine mostly thanks to the reflected light from parent star. They are consequences of the cooling phase seen for warm objects, when the age is old enough to make the intrinsic emission negligible. The separation limit between warm and cold planets is not easy to define, because it depends on many factors: wavelength, mass of the companion, orbital separation, albedo and age. The luminosity of the host star is also important, because the irradiation can alter the atmospheric structure and temperature. Fig.1.2 shows how different can appear the spectrum of a planet at the boundary between cold and warm planets at two different separations, as a function of the heating due to the host star: both of these spectra are different from an average G0V star spectrum (Fig.1.3), which is almost free of strong absorption features at low resolution.

The reflected luminosity is dependent on the distance between star and planet and on the wavelength dependent albedo. Since the radius of the planet does not

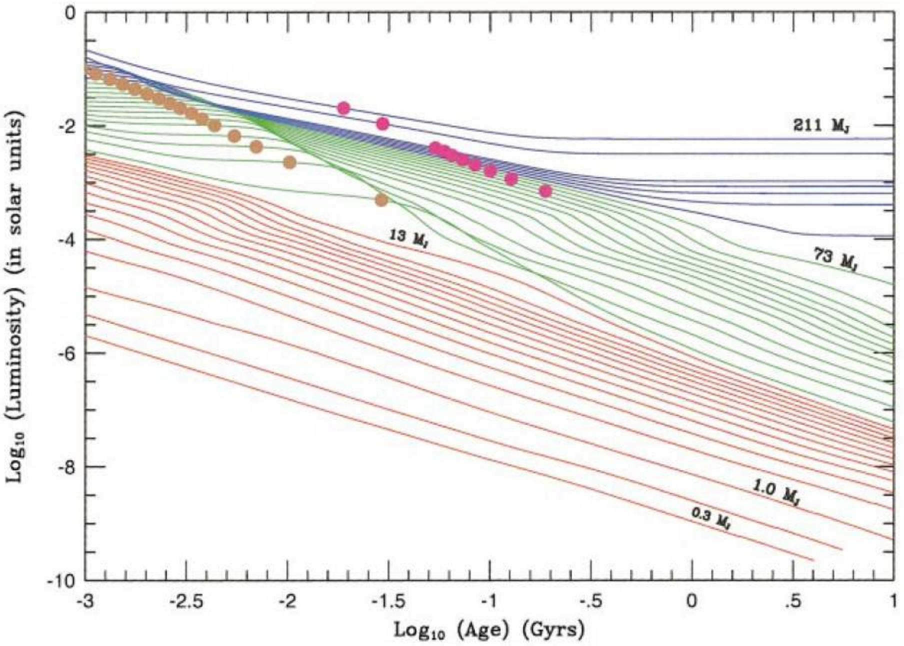

Figure 1.1: Evolution of the luminosity of isolated solar-metalicity red dwarf stars and substellar-mass objects versus age. The stars are shown in blue, the BDs above 13 M_J in green and the BDs/giant planets below 13 M_J are shown in red. Yellow dots mark when 50% of the deuterium has burned, while magenta dots mark when 50% of the lithium has burned. Figure taken from Burrows et al. (2001).

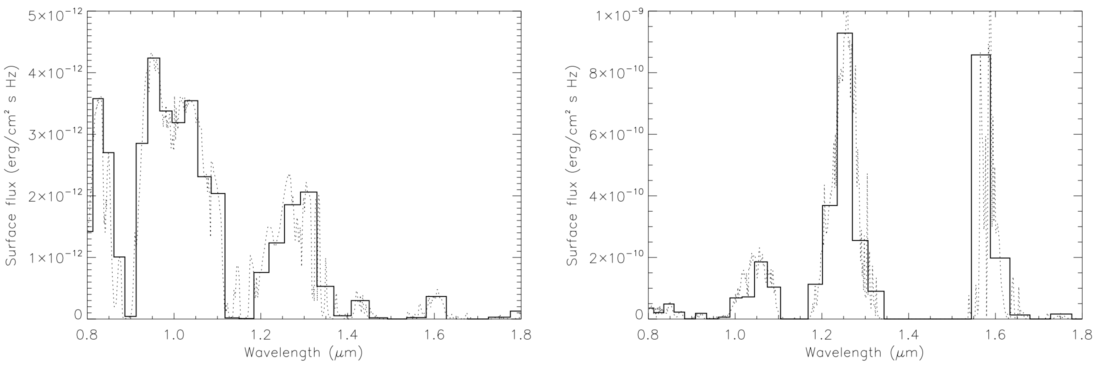

Figure 1.2: At left: Near-infrared spectrum (between 0.8 and 1.8μm) of a 1 M_J planet orbiting a solar-type star (G2V) 1 Gyr old, with a separation of 10 AU. At right: The spectrum of the same planet but at a separation of 1AU. For both these planets we considered the spectral emission mainly intrinsic, with a negligible component of reflected light. The solid spectrum has a spectral resolution of 30, the dotted line of 750. Data taken from Burrows et al. (2004).

change with mass for objects in substellar regime[2] (Burrows et al., 2001), similar contrasts are expected for planets of different masses. Also the spectral features should be not very different: so, in general, the signal coming from a cold giant planet is weakly dependent on the mass.

Old stars represent the largest fraction of nearby stars; on the other hand, the star-planet contrast is less favorable than for the young-warm case. An interesting advantage of the reflected light is its polarization, that provides further diagnostic for planets identification (see Sec.3.2.3).

To understand the behavior of the reflected light with the wavelength, Sudarsky et al. (2000) presented a set of theoretical models of albedo and reflection spectra. Giant gaseous planets are divided into classes, according to the effective temperature which for old planets corresponds to a sequence of orbital separations (the higher the temperature, the closer the planet to its host star):

- Class I: $T_{eff} < 150$ K; CH_4 and NH_3 are the most prominent molecular absorptions; bond albedo is ranging from 0.4 to 0.65. An example is Jupiter.

- Class II: $T_{eff} \sim 250$ K; molecular absorptions of CH_4 and H_2O; they can have a large albedo (0.9) in case of high levels of condensation. Examples are 16 Cyg b, 47 Uma b, υ And d, ϵ Eri b.

---

[2] This is true only for giant gaseous planets, down to 0.3 M_J: obviously for a rocky planet, or Earth-like planet, there is a much different relation between mass and radius, and also different spectral features!

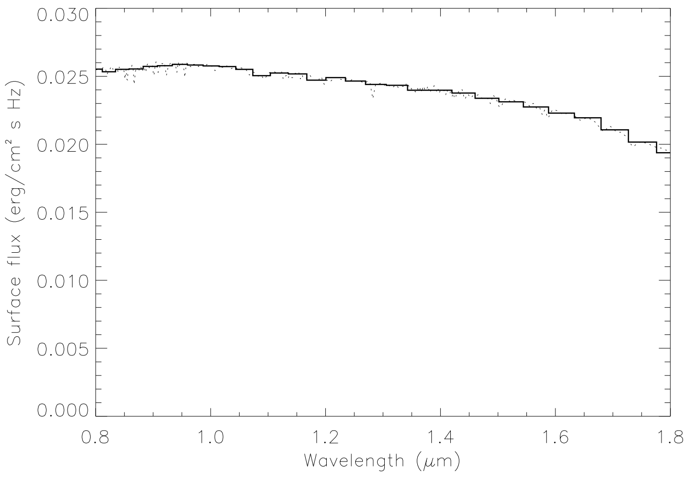

Figure 1.3: Near-Infrared spectrum (between 0.8 and 1.8μm) of a G2V star at the spectral resolution of 30 (solid line) and 750 (dotted line). In this plot are not included the absorptions caused by terrestrial atmosphere. Data taken from Burrows et al. (2004).

- Class III: T$_{eff}$ $\sim$ 350 K; alkali absorptions, and consequently low albedo. Examples are 55 Cnc b, 70 Vir b, υ And c.
- Class IV: 900 $<$ T$_{eff}$ $<$ 1500 K; roasters; extreme absorption by alkali, in particular Na and K, causes a very low albedo. Examples are 51 Peg b, υ And b, GL229 b.
- Class V: T$_{eff}$ $>$ 1500 K; very high albedo because of a silicate layer high in the atmosphere; presence of alkali, CO, H_2O, but no CH_4. Some examples are HD 209458 b and, uncertain, τ Boo b.

The albedos for the five classes are presented in Fig.1.4, as functions of wavelength in optical and near-infrared range. In these plots two cases are considered: the "isolated" planets and the planets whose pressure-temperature profile has been modified as a function of the stellar insolation (Seager & Sasselov, 1998).

In general, we expect higher albedos in the optical range than in the non-thermic infrared ($<$1.8μm), because of the large amount of absorption bands, in particular CH_4, NH_3 and H_2O. Nevertheless, there are many spectral regions with high reflectivity between 1.0 and 1.8μm. The presence of these alterning regions at high and low reflectivity at high contrast can be used as an indicator of the physical properties of the planet.

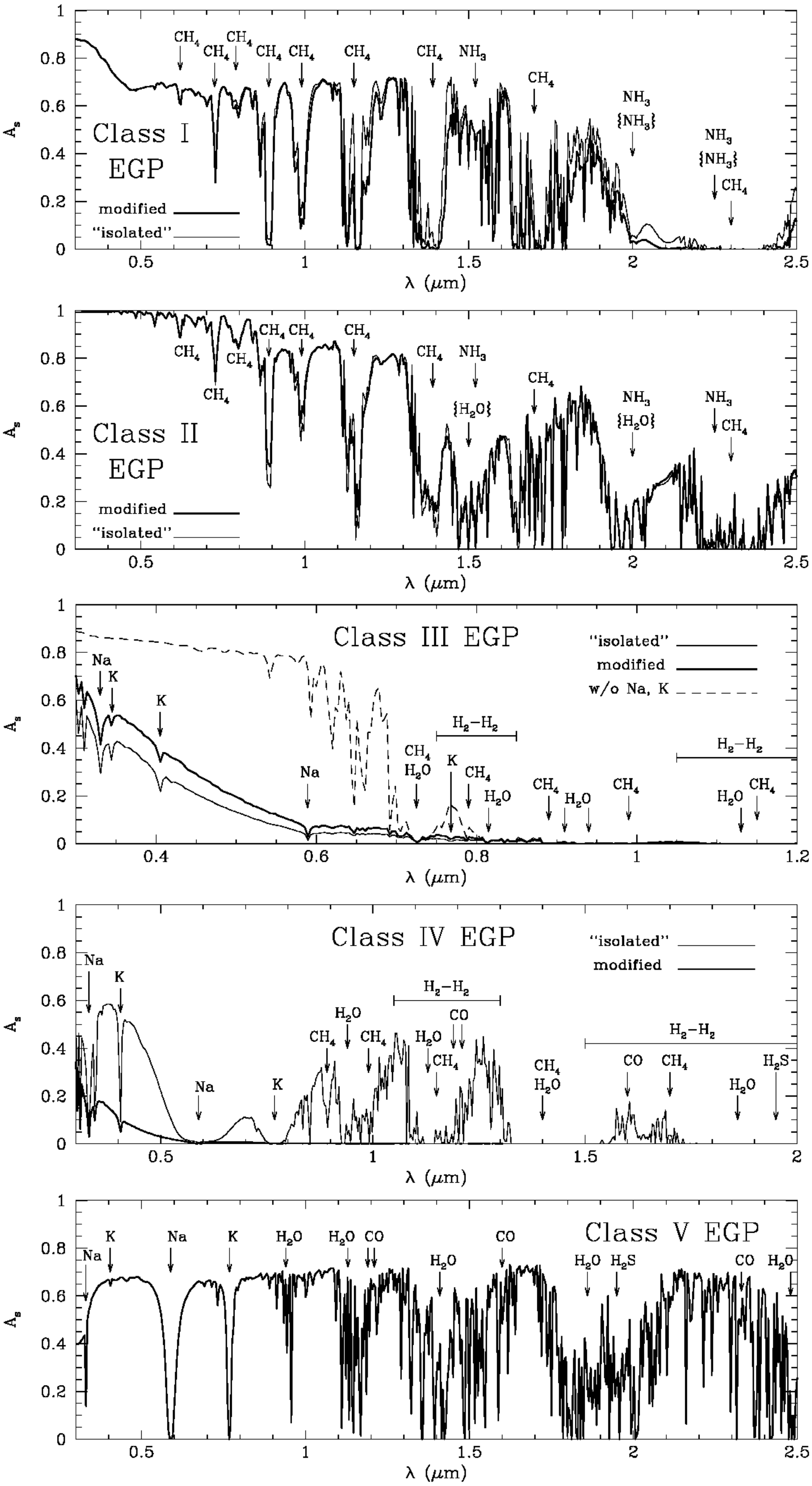

Figure 1.4: Spherical albedos for giant planets of classes I, II, II, IV and V (from top to bottom); from Sudarsky et al. (2000). More details can be found in the text.

Chapter 2

Detection of extrasolar planets

Today, more or less ten years after the detection of the first giant planet around a Sun-like star by Mayor & Queloz (1995), the astronomers know around 200 planets outside the Solar System, and they need always new scientific instruments in order to go into the details of these new discovered worlds. Most of them have been detected using the measurement of periodic residual in radial velocities; and there is a large number of astronomers still working at the moment with this technique; but the scientific community is continuously suggesting new ideas and new concepts for a more detailed study of extrasolar planets.

Perryman (2000) presents a diagram on which some of the most important methods are graphically shown (Fig.2.1): they are many, articulated and sometimes quite complicated. Therefore in our description of detection techniques we decided to not go into detail of all the possibilities, but just to present the main ideas of the most important ones. For a complete review see Perryman (2000) and, more recently, Seager (2003) and Trimble (2004).

First of all, we split the detection methods in two important categories: the ones based on *indirect* measurements, some of which are presented in this chapter, and the others based on *direct* detection, presented in Chapter 3. Indirect methods are based on the assumption that a system composed by a giant planet orbiting around a star could be considered a binary system with very low mass ratio: therefore, the well known techniques devoted to identify and study binaries can also be used to search for planets (obviously if they are pushed to the required precision). In general these techniques aim to detect periodic variation of the light from the host star due to the influence of the planet. Although they are extremely popular, because all the confirmed detections till now have been achieved using them, these methods cannot allow a complete investigation of the planets. That's the reason

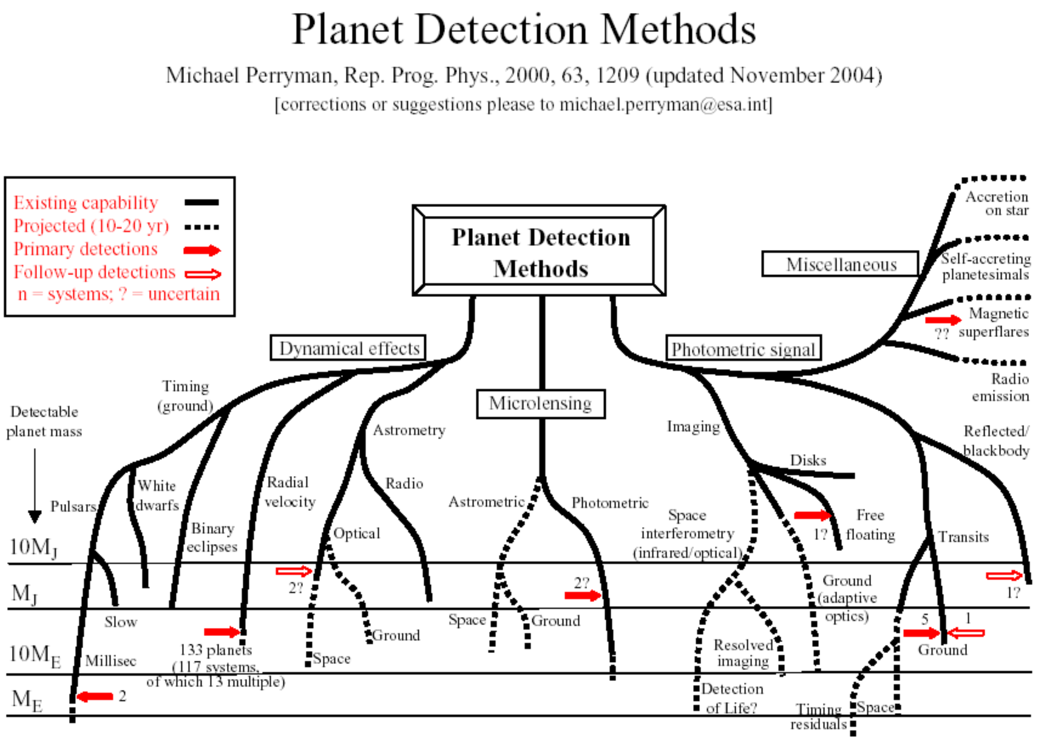

Planet Detection Methods

Michael Perryman, Rep. Prog. Phys., 2000, 63, 1209 (updated November 2004)

[corrections or suggestions please to michael.perryman@esa.int]

Figure 2.1: Detection methods for extrasolar planets, from Perryman (2000) and updated in November 2004. The number of planets actually detected by each method is reported.

why great attention now is focused on the direct methods, which aim to detect the photons coming directly from the planet, but which also have given till now very few confirmed detections because of the extreme faintness of the planetary light.

2.1 Radial velocity measurements

Radial Velocity (RV) semi-amplitude K of a star due to the presence of a companion with negligible mass with respect to the primary is given by

$$K = \left(\frac{2\pi G}{P}\right)^{\frac{1}{3}} \frac{m \sin i}{M^{\frac{2}{3}}\sqrt{1-e^2}} \qquad \mathrm{m/s}, \tag{2.1}$$

where P is the orbital period, m the mass of the planet, M the mass of the star, i the inclination of the orbital plane and e the eccentricity.

The $\sin i$ dependence means that orbital systems seen face on ($i = 0$) cannot be detected in this way; at the same time RV measurements can determine only $m \sin i$ rather than m. For this reason, RV can provide only a lower limit to the planet mass

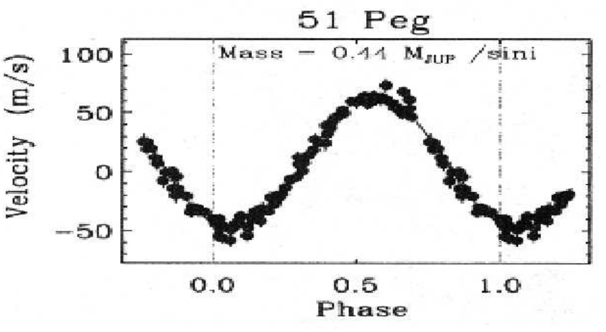

Figure 2.2: The radial velocity curve of 51 Peg, revealing the presence of the first giant extrasolar planet detected. Adapted from Marcy et al. (2000).

since the orbital inclination is generally unknown[1].

Not any stars are good targets for RV studies: stars earlier than mid F have too few and too shallow spectral lines, while young stars and red giants are characterized by intrinsic radial velocity variations (spots, flares, convective granulation) that could mask keplerian variations (Saar et al., 1998). Best targets are old main sequence and slightly evolved G-K stars. M stars are more difficult, because of the large number of active objects in this category and because of the faintness of M dwarfs. In any case, even old solar-like stars are not expected to be stable at a level better than 1 m/s: this can be considered the fundamental astrophysical limit of RV technique (Butler & Marcy, 1998).

At present, more than 90% of the found extrasolar planets has been detected using this method; and the development of new spectrographs and new instruments had brought to a progressive decrement of the lower mass limit of detections, down to tens of earth masses (see, e.g., McArthur et al., 2004; Santos et al., 2004a, : both these planet are around 14 $M_\oplus$). This is surely the most productive way to search for planets, and for this reason there are many projects devoted to RV measurements: some of them, chosen between the ones that detected the largest number of objects, are presented in Tab.2.1. All the programs for RV detections are from the ground, at present.

---

[1] Theoretical considerations about probability to get certain inclinations give us that 87% of random inclinations should have $\sin i > 1/2$, implying that in most cases real masses should not be very different from $m \sin i$

2.2 Astrometry

The angular displacement of a star due to the presence of a companion is given by

$$\Theta = \frac{m}{M}\frac{a}{d} \qquad \text{arcsec} \tag{2.2}$$

where m and M are the planetary and stellar mass respectively, a the orbital semi axis in AU and d the distance of the star in parsecs.

The astrometric method is essentially independent from inclination, so it can derive the mass of the planet unambiguously, and then it can be used with any kind of stars because it is not very sensitive to intrinsic stellar variations. On the other hand, it is really useful only with large orbital radii, and it is strongly dependent on the distance of the target: thus the method is limited to nearby stars. Astrometry can be considered complementary to RV method, which is more sensitive to inner orbits.

At the moment, at least one planet has been seen using astrometry; however it was not a discovery, but an independent measurement of Gl 876b (already discovered with RV observations) using the Fine Guidance Sensor on Hubble Space Telescope HST (Benedict et al., 2002). Although many projects for ground-based observation of astrometric detection are under study at the moment, the best way to astrometrically search for planet seems to be from space, and various space missions have been planned with this purpose (see Tab.2.1 for some examples).

2.3 Transits

High precision photometric monitoring could reveal the temporary luminosity drop of a star when a planet transits the stellar disk. This drop follows this relation:

$$\frac{\Delta L}{L} \simeq \left(\frac{R_p}{R_*}\right)^2 . \tag{2.3}$$

L is the luminosity and ΔL the luminosity drop; R_p is the radius of the planet, while R_* is the radius of the star.

Since the geometric probability of observing a transit is $p \sim R_*/a$, where a is the orbital semi axis, close-in giant planets like 51 Peg are strongly favored to be detected ($p \sim 10\%$); at 1 AU this probability is dropped at around 0.5$\%$ (Sackett, 1999).

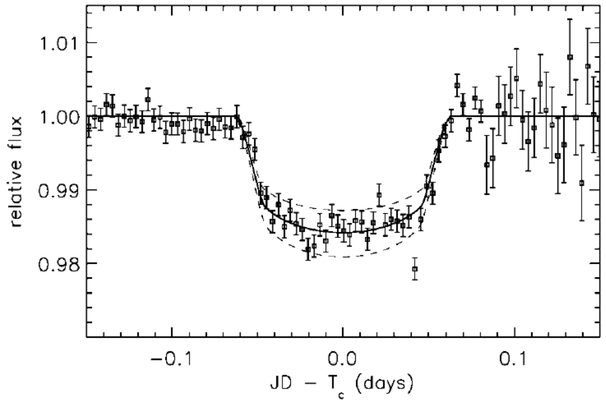

Figure 2.3: The transit oh HD209458b: the light curve shows clearly a minimum due to a planetary companion. From Charbonneau et al. (2000).

Using this technique some planets have been actually observed: in particular HD 209458b (Charbonneau et al., 2000), already detected using RV, whose light curve is shown in Fig.2.3. The other planet detections have been based on the OGLE experiment (Optical Gravitational Lensing Experiment, Udalski et al., 2004, see Tab.2.1), with few significant exceptions like TReS-1 (Alonso et al., 2004), the first planet detected by a wide-field, bright-star survey.

If the radius of the star can be estimated (e.g. from spectral classification) then R_p is also known from Eq.2.3. With knowledge of period and an estimation of the mass of the star (again obtained from spectra) also a can be derived. The minimum inclination where transits can occur is given by $i_{min} = \cos^{-1}(R_*/a)$: evaluation of i for realistic cases demonstrates that i must be very close to 90^o; thus, a combination of RV and transit observations can give a quite precise determination of the mass and the density of the planet.

Another interesting advantage of transit method is the dependence of ΔL on the wavelength: this can lead to a first spectral analysis of the planet atmosphere. Also looking for small distortions of stellar spectral line profiles during ingress or egress can allow to recognize chemical components of the planetary atmosphere: see, e.g., the detection of oxygen and carbon on HD 209458b in Vidal-Madjar et al. (2004). The principal disadvantage of this method is that it requires configuration in which the viewing direction to the earth lies in orbital plane of the planet. This contribute strongly to keep very low the probability of detection, even if at least this orientation is more probable than any other. On the other hand, a large number of stars can be followed at once.

It has been recently noticed that the use of integral field spectroscopy can allow higher signal-to-noise ratios in detecting the minima of the light curve during a transit, in particular if the star is appropriately de-focused: this because the number of collectable photons can be increased avoiding saturation even in case of large integration times (Arribas et al., 2006; Angerhausen et al., 2006).

The sensitivity of ground-based transit searches is set largely by atmospheric changes: thus an earth crossing a sun, which blocks only about 10^{-4} of the light, can be caught this way only by space missions. Nevertheless, a vast number of ground-based projects are under going or under construction aiming to detect planets with observations of transits (see Tab.2.1).

2.4 Gravitational Microlenses

Microlensing events happen when a foreground compact object and a distant background star are well aligned with the observer. The light of the star can be magnified several times. When the lens is a binary system, strong deviations on magnification curves arise. In particular, if the lens has planets, deviations occur as well and their identification could be attempted. Such deviations have short timescales, so dense temporal sampling is required.

The photometric precision required is around 1%, feasible even in the bulge crowded fields, where planet searches concentrate on. Microlensing anomalies are expressed in terms of mass ratio $q = M_p/M_l$, (mass of the planet over mass of the lens) and of the Einstein radius:

$$\Theta_E = \sqrt{\frac{4G}{c^2}\frac{M_l}{d_{rel}}} \tag{2.4}$$

where d_{rel} is the lens-source relative distance. The planetary mass and orbital semi axis can be derived only in statistical sense, using for M_l and d_{rel} typical values for bulge lenses: 0.3 $M_\odot$ and 6 kpc.

A disadvantage of microlensing observations is that they are unique and confirmations or follow-up observations are not possible. On the other hand, this method is able to search for planets very far from the solar neighborhood and even extra-galactic planets. In addition, it doesn't need big telescopes for detections.

The most important searches for microlensing detections are MOA and OGLE III (see Tab.2.1): the project OGLE, already cited for transit detections, was born in order to search for microlensing events (Udalski et al., 1993), and now it's working

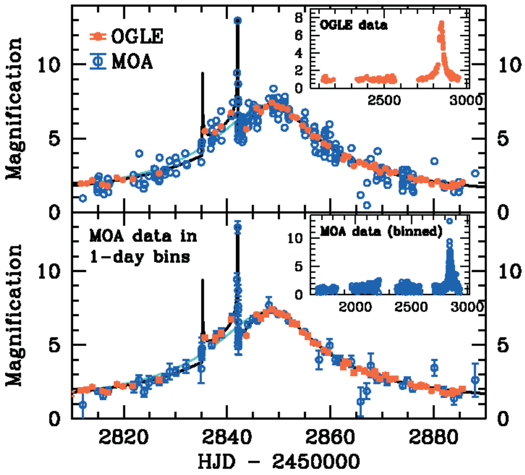

Figure 2.4: Light curve of the observation of the object OGLE 2003-BLG-235/MOA 2003-BLG-53 with OGLE and MOA. The top panel presents the complete data set during 2003 (main) and the 2001-2003 Ogle data (insert). The bottom one is the same of the top panel, but with the MOA data grouped in 1 day bins. Is it clearly visible the strong and steep magnification due to the planet both for OGLE and for MOA. From Bond et al. (2004).

on both the directions. A collaboration between OGLE and MOA has led recently to the cleanest case of microlensing so far, described in Bond et al. (2004); the light curve measured in that case is presented in Fig.2.4.

2.5 Periodic residuals in pulsar timing

This method allows to detect earth-like planets, but it is limited only to pulsars. Actually it was used to detect the first extrasolar planet ever discovered (PSR 1257+12, Wolszczan & Frail, 1992).

Besides position and velocity, an orbital motion affects also light travel time of the objects involved; for most astronomical targets there are not time reference to measure such effect, but for pulsars very accurate timing measurements can be performed, down to 10^{-19} s/s for a millisecond pulsar. The amplitude τ_p of timing residuals due to a companion in edge-on orbit is given, assuming M_{pulsar} = 1.35 $M_\odot$, by

$$\tau_p = 1.2 M_p P^{\frac{2}{3}} \qquad \text{ms,} \tag{2.5}$$

where M_p is the mass of the planet in $M_\oplus$ and P the period in years (Wolszczan, 1997).

At the moment, very few planets have been detected using this method, and the lack of detections indicates that planets around pulsars are rather rare.

2.6 Other indirect methods with Future Potential

Many new ideas have been developed in last years, with the goal of detecting new planets. We are presenting here only some examples, but a more complete list could be found in Trimble (2004).

- **Distortions and disturbances of disks**: Some structure and features of planet-forming disks (e.g. gaps, belts etc) have been suggested as planet signatures in many cases. In particular β Pic was the first one whose warp was advanced as evidence for a planet in formation (Brunini & Benvenuto, 1996), and the idea persists till now (e.g. Okamoto et al., 2004; Telesco et al., 2005). Anyway, no clear detection has been confirmed.

- **Periodic residuals in timing of eclipsing binaries**: Considering a well known eclipsing binary star, we can try to detect periodic variations of the minima time due to the orbit of a giant planet. Deeg et al. (2000) have perhaps seen this in CM Dra, but further confirmations are needed.

- **Phase reflection variations method**: It should be possible to detect, in particular with space telescopes, the sinusoidal variation of the light coming from a planetary system due to the light reflected by the planet, which changes periodically because of the orbital phase (Jenkins & Doyle, 2003). This method requires, anyway, the detection of variations in amplitude of a factor around 10^{-9}.

Project	Status	Web site
Radial Velocity Measurements		
McDonald Obs. S.(a)	Ongoing	www.as.utexas.edu/astronomy/research/research.html
ELODIE	Ongoing	obswww.unige.ch/∼udry/planet/elodie.html
CORALIE	Ongoing	obswww.unige.ch/∼udry/planet/coralie.html
Calif. & Carn. Pl. S.(b)	Ongoing	exoplanets.org
AFOE	Ongoing	cfa-www.harvard.edu/afoe/espd.html
ESO-CES	Closed	www.sc.eso.org/∼mendl/planets/planets.html
Anglo-Austr. Pl. S.(c)	Ongoing	www.aao.gov.au/local/www/cgt/planet/aat.html
Astrometry (from the ground)		
Keck Interferometer	Under study	planetquest.jpl.nasa.gov/Keck/keck_index.html
PRIMA	Under study	obswww.unige.ch/Instruments/PRIMA
STEPS	Ongoing	huey.jpl.nasa.gov/ spravdo/STEPS.html
Astrometry (from space)		
GAIA	Under study	sci.esa.int/gaia
SIM	Under study	planetquest.jpl.nasa.gov/SIM
Transits (from the ground)		
STARE	Ongoing	www.hao.ucar.edu/public/research/stare/stare.html
Tennessee A. P. T.(d)	Ongoing	schwab.tsuniv.edu/t8.html
OGLE III	Ongoing	sirius.astrouw.edu.pl/∼ogle
Transits (from space)		
KEPLER	Under study	www.kepler.arc.nasa.gov
COROT	Under study	www.obspm.fr/encycl/corot.html
Gravitational Microlenses		
MOA	Ongoing	www.physics.auckland.ac.nz/moa
OGLE III	Ongoing	sirius.astrouw.edu.pl/∼ogle

Table 2.1: A summary of the most important searches for planets for the various methods discussed in this Chapter. An indication if the searches are ongoing or on project at present (July 2006), and a web site for consultation, are provided. Where abbreviated: *a*) McDonald Observatory Search; *b*) California & Carnegie Planet Search; *c*) Anglo-Australian Planet Search Program; *d*) Tennessee Automatic Photoelectric Telescope.

Chapter 3

Direct Observation

Direct detection of reflected or emitted light from a planet, although the most difficult, is the most promising method for detection and study of extrasolar planets. In particular, it is the only method that will allow the study of planet atmospheres and surface characteristics, in addition to numerous informations about orbits, masses, radii and temperatures.

As already said, there are two kinds of emissions by a planet: the thermal emission and the reflected light. They have different characteristics, are mainly visible in different spectral bands and can give us various information on the object (see e.g. Tab.3.1).

- **Reflected light**: The planet reflects the stellar light with a flux ratio given by

  $$\frac{F_{refl}(t)}{F_*} = \frac{A_{pl}}{4} \cdot \left(\frac{R_{pl}}{a}\right)^2 \cdot \varphi(t) \tag{3.1}$$

  where φ is an orbital phase factor, sinusoidal in case of circular orbits, a is the separation, R_{pl} is the radius of the planet and A_{pl} is the planet albedo (Schneider, 2003). The signal from the companion peaks at the same spectral range of the star, and the contrast is typically 10^{-9} or 10^{-10}.

- **Thermal emission**: If the planet is young enough, it produces an intrinsic thermal emission in near- and mid-infrared. If it is older, it can anyway be heated by the star at a temperature

  $$T_{pl} = T_* \cdot \left(\frac{R_*}{2a}\right)^{1/2} \cdot (1 - A_{pl})^{1/4}\,. \tag{3.2}$$

Consequently, it emits a thermal flux (integrated over all the wavelengths) given by

$$\frac{F_{th}}{F_*} = \left(\frac{R_{pl}}{2a}\right)^2 . \tag{3.3}$$

The distribution of F_{th} and F_* with wavelength is different, so the ratio is typically about 10^3 times larger in the Near-Infrared than in the visible range, and there is no orbital phase factor here.

From an instrumental point of view, direct detections are very difficult because planets, when observed with a telescope, are embedded in the diffraction halo of the host star, and because of the enormous brightness contrast between stars and planets. Looking for very young planets, not yet so faint, which are not orbiting stars seems to be extremely easier, and some objects have been actually detected (see e.g. Zapatero Osorio et al., 2000) but these objects cannot be considered planets if we follow the definition of planet given in the Introduction.

For all the other cases, imaging efforts are directed at ways of increasing the planet/star intensity ratio, by observing at longer wavelengths for detection of thermal emission, and by reducing the angular size of the stellar image, which is approximately given by $\vartheta \sim \lambda/D$, without considering atmospheric turbulence. To do this, we need to increase the diameter D of the telescope, and an interferometric architecture with several subapertures could be useful; then, we should try to "turn off" the star, using nulling interferometry or a series of coronographic masks; finally, the use of non circular apertures have been proposed in order to give a cross-shaped stellar diffraction halo, and to make the planet visible when it lies on the diagonal of the cross (Nisenson & Papaliolios, 2001; Spergel et al., 2002).

In any case, the technical difficulties related to the direct imaging of planets did not allow many detections till now: actually, at present, we have only one confirmed detection of an extrasolar planet obtained in this way. It is the planet around the Brown Dwarf 2MASSWJ1207334-393254 (see Fig.3.1), found by Chauvin et al. (2004) at ESO VLT using the adaptive optics near-infrared instrument NACO (Lenzen et al., 1998). A preliminary estimation of the mass of this planet is M=5±2 M_J, and the age should be around 8 Myr.

Parameter	Visible	Infrared
Radius		yes
Mass	yes	
Temperature	yes	yes
Albedo	yes	
Day	yes	
Seasons	yes	yes
Clouds	yes	
Rings	yes	
Moons		yes
O_2	yes	
O_3, CH_4, CO_2, H_2O	yes	yes
Vegetation	yes	
Internal heat		yes

Table 3.1: A summary of the best wavelength regime for different planet characteristics. In general, more refined gradations between "yes" or "no" should be considered. From Schneider (2003).

3.1 From space: Problems and advantages

The most promising imaging opportunities exist from space, for the simple reason that from space all problems connected to terrestrial atmospheric turbulences are avoided (see, about this, Sec.3.2). From space the shape of the Point Spread Function (here after PSF) is almost given by diffraction. In order to detect and characterize extrasolar planets, a number of specifications of optical architectures are required (Schneider, 2003):

- **Collecting area**: considering that an Earth-like planet around a main sequence star at 10 parsecs has an apparent magnitude of $\sim$25, a collecting area of at least 15 m^2 is necessary; this means a diameter of 4 m for a mono-pupil telescope. For bigger planets smaller telescopes are enough.

- **Spectral resolution**: in order to obtain some of the informations presented in Tab.3.1, a spectroscopical analysis is needed. To detect the spectral bands of O_2 and, eventually, O_3, a resolution of 20 is enough. To make spectroscopy, anyway, the collecting area of the telescope should be significantly larger than 15 m^2 estimated above, and it has to be a function of the required resolution.

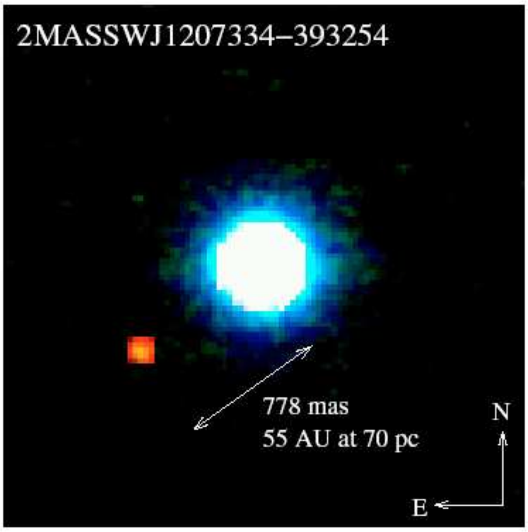

Figure 3.1: Composite image of Brown Dwarf 2MASSWJ1207334-393254 in H (blue), K_s (green) and L' (red). The companion is clearly visible in comparison to the color of the brown dwarf. From Chauvin et al. (2004).

- **Angular resolution**: to separate the planet from the star, an angular resolution λ/D smaller than the star-planet angular separation a/d is required (a is the orbital semi axis, λ the wavelength, D the telescope diameter, d the distance of the star from the Sun). For a planet at a=1 AU at d=10 pc, this leads to a telescope diameter of 2 m at λ=1 μm (reflected light) and 20 m at λ=10 μm (thermal emission).

- **Photometric precision**: albedo variation and moons detection require a photometric precision of $\sim$1%.

Thus, it appears quite clear that there is no need of extremely large space telescopes for detection of extrasolar planets down to Earth-like ones: 4 m of diameter seems to be enough. That is the reason why also the James Webb Space Telescope[1] (JWST), the next generation Space Telescope, has been considered for his planet imaging capabilities. The absence of atmosphere, together with the proportionality of the angular resolution with λ, makes the visible range more suitable for observation than the infrared one. However, above the atmosphere mirror imperfections and thermal flexure are still problems and an Adaptive Optic system can be necessary to cancel the wavefront errors introduced, for example, by corrugations on the mirror surface.

---

[1] *http://www.jwst.nasa.gov/home/*

For the next future, two are the most promising space mission that will be launched:

1. The NASA **Terrestrial Planet Finder**[2] (TPF), whose goal is to image planetary systems and extrasolar Earths and to obtain low resolution spectra (Beichman et al., 2002). Its two designs, the optical coronographic one (TPF-C) or the multi-telescope infrared (5-20 μm) interferometer (TPF-I), would reveal many details of both Earth-like and Giant extrasolar planets.

2. The ESA **Darwin**[3], which is a mid-infrared wavelength space interferometer (Fridlund, 2000) composed by 6 telescopes arranged in hexagonal shape with a baseline of 10s to 100s meters. It will be able to observe Earth-like planets with its "free-flying nulling interferometry".

3.2 From the ground

Prospect for ground-based planetary imaging has concentrated on the use of Adaptive Optics, in order to compensate the loss of information due to atmospheric turbulence. Usually from the ground it is not possible to obtain a diffraction limited PSF, which size is given by a relation $\vartheta \sim \lambda/D$, where ϑ is called the "Airy radius", radius of the first minimum of the diffraction figure. An AO-compensated long-exposure PSF of a star is modeled as the sum of a diffraction limited core and a residual halo (Racine et al., 1999). The total flux in this PSF is

$$F_* = \frac{\pi}{4} D^2 q f_0 10^{-0.4 m_*} t, \tag{3.4}$$

where D is the diameter of the telescope, q the global quantum efficiency, f_0 is the flux density from a zero-magnitude star in the bandpass, m_* is the stellar magnitude and t is the integration time.

Inside the core of the PSF we have a portion $S \cdot F_*$ of the total flux, where S is the Strehl Ratio given by the AO system, distributed following the diffraction profile f_{core}:

$$I_{core}(\vartheta) = S F_* f_{core}(\vartheta). \tag{3.5}$$

The adopted profile for the residual halo contains a fraction $(1-S)F_*$ of the total flux,

---

[2] *http://planetquest.jpl.nasa.gov/TPF*

[3] *http://sci.esa.int/darwin*

$$I_{halo}(\vartheta) = (1 - S)F_{*}f_{halo}(\vartheta), \tag{3.6}$$

and the shape function has a convenient Moffat profile that, from Racine et al. (1999), we decided to express using an index β=11/6:

$$f_{halo}(\vartheta) = \frac{0.488}{W_{halo}^{2}}\left[1 + \frac{11}{6}\left(\frac{\vartheta}{W_{halo}}\right)^{2}\right]^{-\frac{11}{6}}. \tag{3.7}$$

This relation is characterized by a Full Width Half Maximum (FWHM) intensity W_{halo} which contains $\sim$25% of its flux, and by a $\vartheta^{-11/3}$ decay beyond a few W_{halo}, as appropriate to a turbulence-degraded profile (Roddier, 1981).

If a companion is present, its PSF is assumed to contain a fraction S of its total flux F_c within an area corresponding to the solid angle $\pi(\lambda/D)^2$. This fraction is the net signal that must be detected against noise. The sources of noise are different in the core or the halo:

1. The photon noise of the coherent core of the primary;
2. The photon noise of the incoherent halo of the primary;
3. The read noise (here after RON);
4. The sky noise;
5. The speckle noise.

The last one, the speckle noise, has features different from the others and requires a detailed explanation, because it will also result the most important source of noise for detecting planet.

3.2.1 The problem of Speckle Noise

Speckles result from the interference of light from many coherent patches distributed over the full aperture of the telescope. These patches could be bubbles or cells created by atmospheric turbulence, with different refraction index. We call Fried Radius r_0 the maximum diameter of a collector that is allowed before atmospheric distortion seriously limits performances; this parameter can be extremely useful to describe the atmospheric turbulence phenomena.

A single cell would work as a subpupil, creating a diffraction limited PSF with width $\sim \lambda/r_0$. Two subpupils, separated by a distance D, constitute a two-beam interferometer and the result is a pattern of linear interference fringes of width $\sim \lambda/D$. The introduction of a third subaperture non collinear with the first two gives three intersecting patterns of fringes, and where these fringes interfere constructively a bright speckle of width $\sim \lambda/D$ appears. The randomly varying phase difference between the subapertures causes the movement of this speckle within the broad PSF envelope[4].

If the whole pupil is full of these bubbles, it is possible to calculate the number of adjacent speckles within a "seeing" disk of width $\sim \lambda/r_0$:

$$n = k\left(\frac{D}{r_0}\right)^2, \tag{3.8}$$

where k=0.342 when $D/r_0 \gg 1$ (Roddier et al., 1982). The speckle lifetime is

$$\tau_0 \sim \frac{r_0}{\mathit{\Delta} v}, \tag{3.9}$$

and $\mathit{\Delta} v$ is the the velocity dispersion in the turbulent seeing layers across the telescope line of sight. Finally, the number of speckle per unit area is

$$n_s \simeq \frac{k}{\pi\left(\lambda/D\right)^2}. \tag{3.10}$$

In an AO compensated image, a fraction S of the total flux F_* is transferred into a bright central speckle, leaving $(1-S)F_*$ into halo speckles that, by time averaging, produce the smooth long-exposure halo.

The structure of the speckle pattern changes randomly over a interval of time τ_0, which is typically a small fraction of a second. The speckle noise variance is not simply equal to the number of speckle recorded in a given area times the mean speckle brightness, because speckles are not independent events. Speckle noise arises from registration of variations between the evolving speckle pattern in the focal plane and the boundary of a given PSF area in that plane. The variance of speckle noise has been calculated by Racine et al. (1999):

$$var_{speckles} \simeq \frac{F_s^2}{16} \cdot \frac{t}{\tau_0}; \tag{3.11}$$

The speckle brightness F_s varies radially in the image, and can be expressed by the ratio between the halo surface brightness recorded in a speckle lifetime and the

---

[4] More details about speckle formation and statistic can be found in Roddier (1981) and Racine et al. (1999)

number of speckles per unit area[5] (from eq.3.10):

$$F_s(\vartheta) \simeq \frac{\pi\,(\lambda/D)^2}{0.342} \cdot I_{halo}(\vartheta) \cdot \frac{\tau_0}{t}; \tag{3.12}$$

In this equation, it has to be noted that I_{halo} is proportional to t (see Eq.3.4 and 3.6), so this value of F_s does not really depend on the integration time but only on τ_0.

Finally, the relation for the variance of speckle noise in the halo, obtained from Eq.3.6, 3.11 and 3.12, is:

$$var_{speckles} \simeq 1.7\pi \left[\left(\frac{\lambda}{D}\right)^2 (1-S)\, F_* f_{halo}(\vartheta)\right]^2 \frac{\tau_0}{t}. \tag{3.13}$$

At this point, it is possible to evaluate the signal-to-noise ratio of a companion (which signal is SF_c) imposed by speckle noise ($\sqrt{var_{speckles}}$), using Eq.3.7 and 3.13:

$$S/N_{speckles} \simeq 1.2\frac{S}{1-S}\left(\frac{D}{r_0}\right)^2 \cdot \frac{F_c}{F_*}\left[1+\frac{11}{6}\left(\frac{\vartheta}{\lambda/r_0}\right)^2\right]^{\frac{11}{6}} \cdot \left(\frac{t}{\tau_0}\right)^{\frac{1}{2}}. \tag{3.14}$$

A simple calculation of the ratio between speckle noise and photon noise can be useful to understand the importance of speckle noise in detection of companions very close to parent stars. The variance of halo photon noise over a PSF area is $\pi\,(\lambda/D)^2\, I_{halo}(\vartheta)$, while the variance of halo speckles is presented in Eq.3.13. For typical values of the parameters (e.g. see Fig.3.2) it emerges that the ratio is larger than 1 at $\vartheta < W_{halo}$ for a stellar magnitude smaller than 16. The conclusion is that speckle noise dominates shot noise in the halo of bright stars: hence, it is the most important noise source in that region of the stellar PSF.

Anyway, in case of long exposure time, when the speckles form a almost uniform seeing disk, or in case of observations outside the atmosphere, a new class of speckles becomes important: the so-called "super speckles". They are generated by quasi-static aberrations, imperfections of the instrument, and they have a life time extremely longer than the atmospheric speckles one. Since it is not easy to predict this life time, it is also difficult to estimate the impact of these speckles on the total noise.

---

[5] This assumes that at all times the radial profile of speckle brightness follows the same symmetric f_{halo} relation: that is not really true, but it doesn't affect the estimate of speckle noise.

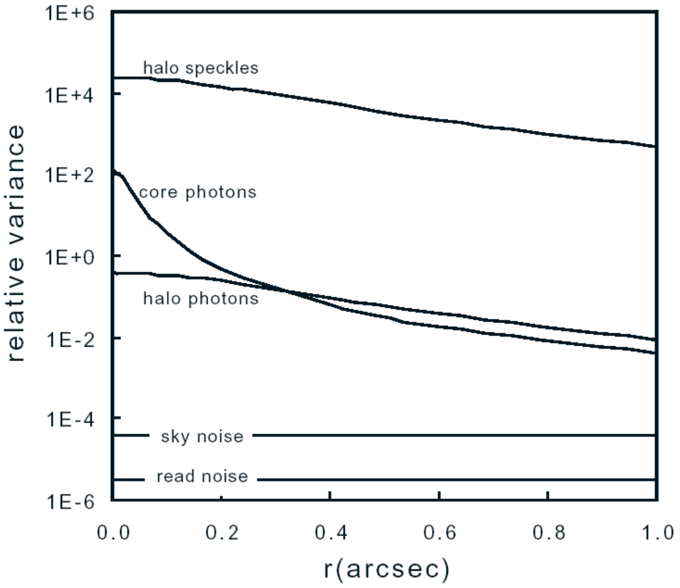

Figure 3.2: Relative importance of the variances for the different noise components. The parameters used are: f_0=3·10^9 photons/(m^2s), q=0.2, D=3.6m, λ=1.6μm, S=0.5, m_*=8, m_{sky}=16, s=30 pixels/arcsec, RON=30 e^-, t=200s, r_0=1m and τ_0=0.1s. Speckle variance dominates by a factor of $\sim 10^4$! From Racine et al. (1999).

3.2.2 Techniques for reduction of Speckle Noise: AO, SDI, etc.

It is clear that an efficient reduction of speckle noise is fundamental in order to detect a planet from the ground, or in general a companion very close to its host star, that, if it is not placed within the Airy Radius, it will be on the halo of the star. As seen from Fig.3.2, if we reduce somehow the total noise to the mere photonic one, we can gain a factor of hundreds to the signal-to-noise ratio: in this case, for instance, a Sun-Jupiter system (Δm $\sim$20) would be detectable with an 8m telescope at a distance of 10pc, which corresponds to an angular separation of $\sim 0''.5$.

From Eq.3.14 we can see that a good way to increase the signal-to-noise ratio is to increase the Strehl Ratio S, reducing in this way the intensity of the halo. At present, the AO systems can reach a value of S around 0.7 in near-infrared, and probably in future we will reach 0.9 or more. But other techniques have been prepared, in order to make faint companions detectable also by telescopes not equipped with extreme AOs. An interesting one is the Simultaneous Differential Imaging (SDI) method. The idea is to subtract the speckle pattern from an image, and this can be done with pairs or groups of images taken simultaneously in different narrow-band filters closely adjacent in wavelength. The spectral bands should be chosen accurately, in order to have very different contrast between primary and

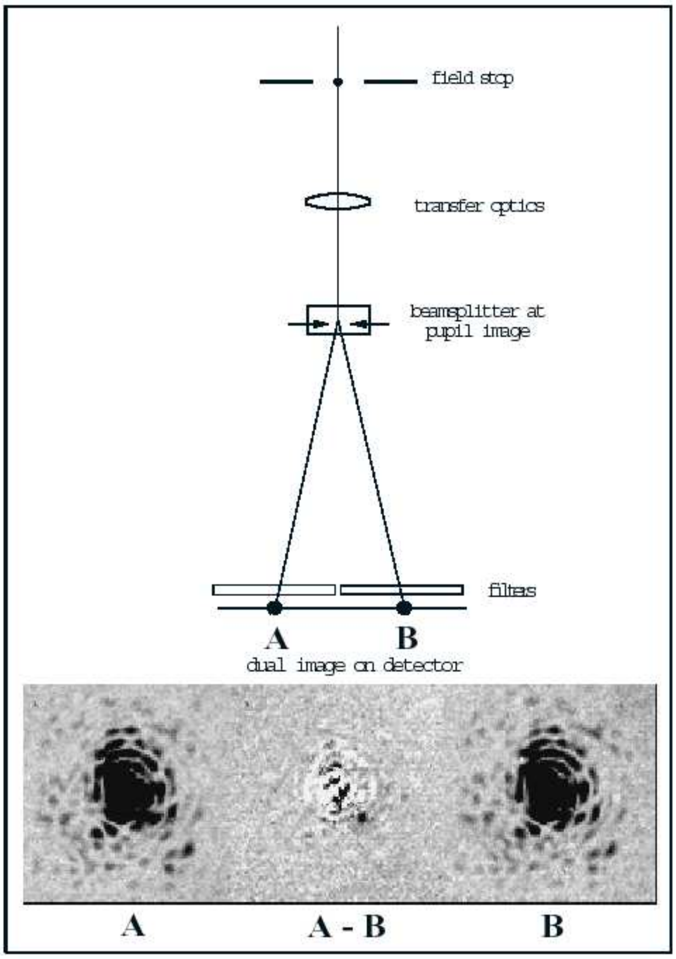

Figure 3.3: The resulting images of a dual-imaging arrangement, and the difference $A - B$, as suggested by Racine et al. (1999). The artificial image of a companion, much fainter than the primary (Δm=5 mag), is clearly visible im the difference image.

companion. For example, if the companion is a cool brown dwarf or a giant planet, it could be useful to work across the methane band at 1.59 μm, as suggested by Rosenthal et al. (1996). This idea has been deeply developed by Racine et al. (1999), and Fig.3.3 shows how it should work in the case of a simple subtraction of two images.

Some precautions are required in order to obtain optimal results (Marois et al., 2000): the geometry of the frames must be rescaled (the dimension of the speckle pattern is proportional to λ), the fractional bandpass of the filters must be closely similar, the fractional difference between filter wavelengths,

$$\frac{\Delta\lambda_{i,j}}{\lambda_i} = \frac{\lambda_i - \lambda_j}{\lambda_i}, \tag{3.15}$$

must be as small as possible, to minimize the residuals caused by the evolution of speckles and PSF with wavelength. Obviously, it can be very difficult to obtain a value very close to zero for this fractional difference, and this is the problem that most limits the effectiveness of the technique. Marois et al. (2000) suggest to use not just two but three different images, I_1, I_2 and I_3, taken at wavelengths $\lambda_1 < \lambda_2 < \lambda_3$, combined into a double difference image:

$$dd = d_{12} - kd_{13} = (I_1 - I_2) - k(I_1 - I_3), \tag{3.16}$$

where the factor k is the mean ratio of d_{12}/d_{13}, and can be expressed as a function of the Strehl Ratios S at different wavelengths:

$$k = \frac{S_1 - S_2}{S_1 - S_3}. \tag{3.17}$$

Considering the approximation suggested by Maréchal (1947) for the Strehl Ratio $S \simeq \exp(-\sigma_\varphi^2)$, where $\sigma_\varphi = 2\pi\delta/\lambda$ is the phase error and δ is the linear size of the optical path errors, we can obtain this new formulation:

$$k \simeq \frac{1 - S_1^{(\lambda_1/\lambda_2)^2 - 1}}{1 - S_1^{(\lambda_1/\lambda_3)^2 - 1}}. \tag{3.18}$$

Using Eq.3.16 the reduction of speckle noise could be extremely more efficient than using the simple difference proposed in Fig.3.3 and a graphical demonstration is given in Fig.3.4, where a companion 10 mag fainter than its primary and 0″.5 away is not visible after a simple differential imaging, but appears with a signal-to-noise ratio of ~ 10 after a double difference.

3.2.3 Other methods for direct detection of planets from the ground

Polarimetry

Polarimetric observations can be useful for the enhancement of the contrast between a planet and its parent star (Stam et al., 2004). In fact, the direct starlight integrated over the stellar disk can be considered to be unpolarized, while starlight reflected by the planet is generally polarized. The degree of polarization depends strongly on the composition and structure of the planetary atmosphere: thus, it can be used for planet characterization. A very sensitive polarimetric accuracy is strongly recommended, in particular for characterization of atmospheres; in any case, for the present polarimeters an accuracy of 10^{-6} can be obtained (Hough & Lucas, 2003), and at least the detection of planets should be feasible.

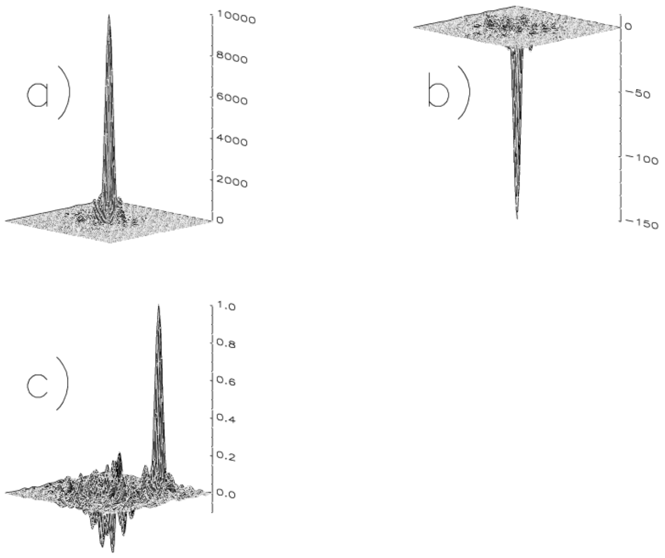

Figure 3.4: Faint companion image extraction from the speckle noise: (a) the original image; (b) after a first subtraction; (c) after double subtraction. The companion is clearly visible only in (c). For more details see Text. From Marois et al. (2000).

An example of an instrument for direct detection of planets using polarimetry is SPHERE (Dohlen et al., 2006, described in detail in Sec.4.3), that will use the well-established and highly accurate Zürich imaging polarimeter ZIMPOL (Povel, 1995). The main idea of SPHERE/ZIMPOL is to image a planetary system in two perpendicular directions: because the stellar light is not polarized, after the difference the polarized source (the planet) should be visible.

Radio emission from Extrasolar Giant Planets

Observations at radio wavelengths can allow direct detection of EGPs, and eventually can provide evidence of the magnetic field of the planets (Stevens, 2004). In fact, observations at decameter wavelengths show Jupiter as an extremely bright source, and the Sun/Jupiter contrast can be $\sim$1. Since radio emission from planets in the Solar System is related to their magnetosphere, it is possible to use radio detections of EGPs also to give direct evidence of extrasolar planetary magnetospheres. However, only very nearby EGPs are likely to be detected by radio emission (the probability of detection is strongly dependent on the distance), and the technique seems to be limited to very massive planets.

3.3 Detection using Integral Field Spectroscopy

From Sec.3.2.2 we have realized that, using the SDI technique, an observation obtained considering a number of wavelengths larger than 2 can considerably help the planet detection and the reduction of Speckle Noise. An interesting consequence of it is suggested by Sparks & Ford (2002): an integral-field spectrograph coupled to a coronograph can produce a data cube, of two space dimensions and one wavelength, that can be elaborated in various ways for detection of planets. From this data cube we can easily extract a number of simultaneous images at different λ in order to apply differential imaging; but on the other hand we can try to recognize the planetary spectrum within the multiple spectra into which the image is divided.

If the spectrum of the star is well known and consistent across the field of view, the study of all the spectra in order to find the differences with the stellar one can be done simply comparing each spectrum with a low-order polynomial fit which reproduces the stellar continuum: but normally the presence of speckle noise strongly disturbs the shape of the continuum of spectra, because speckles are changing position and size with lambda. The same thing happens if the PSF of the coronographic observation is dominated by diffraction. As a consequence of this, the spectrum at a given distance x from the center of the PSF can present

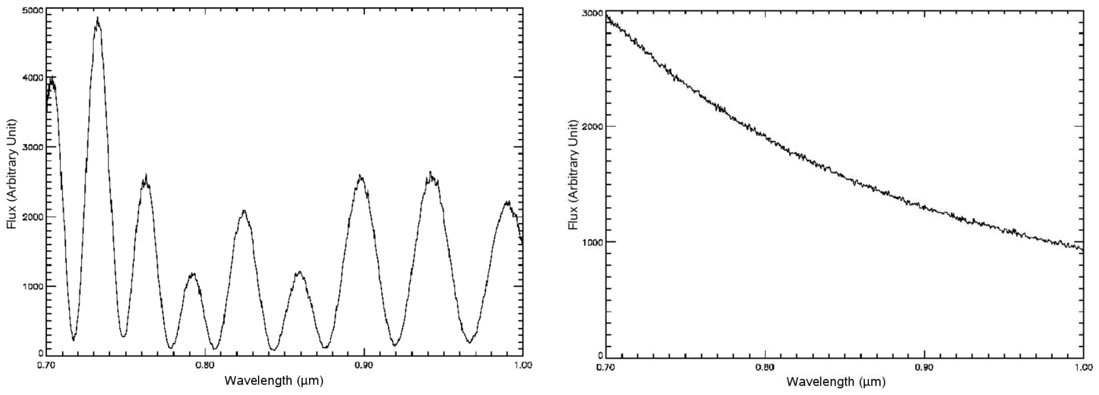

Figure 3.5: Spectral plot for a pixel at 5 arcseconds from the center of the stellar PSF, from a simulated observation with Hubble Space Telescope of a solar-type star at 1 pc (Sparks & Ford, 2002); *At left*: without rescaling of monochromatic images; *at right* after the scale adjustment. The observation is not affected by atmospheric turbulence, and the modulations are caused mostly by diffraction and instrumental speckle patterns: but the technique is valid also to reduce atmospheric speckle noise.

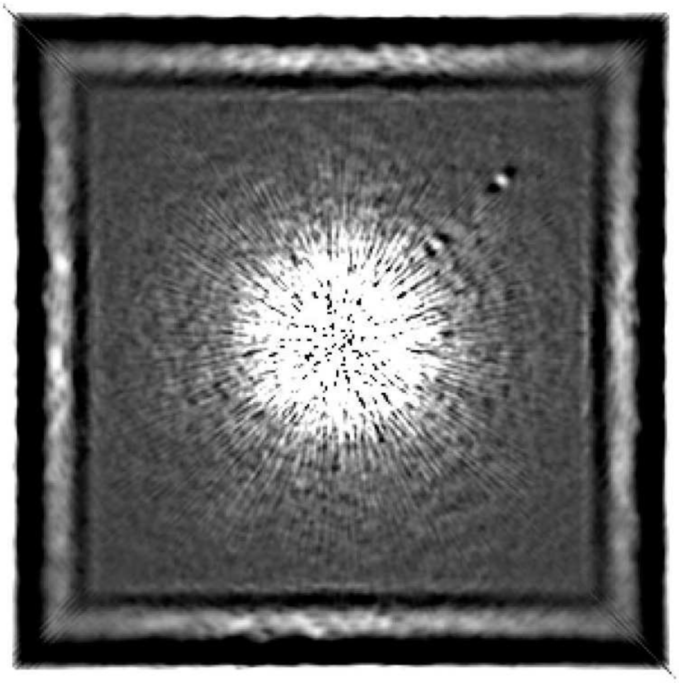

Figure 3.6: Spectrally collapsed image obtained from the simulated data cube of a solar-type star placed at 1 pc from the Sun, observed with HST. A Jupiter-like planet at 5 AU is visible with a signal-to-noise ratio ∼20. Also a closer planet can be seen, at around 3 AU, but with a lower signal-to-noise ratio. From Sparks & Ford (2002).

modulated shapes like the one in Fig.3.5 at left.

In this case the procedure will be this:

- It is needed to apply a "spectral deconvolution" to the data cube, which means that we have to elaborate spectra and images in order to obtain smooth continuum slopes of the stellar spectrum instead of the modulated ones. To do this, we extract a "monochromatic" image for each wavelength and change the image scales inversely to λ. To report an image from λ_1 to λ_2 it should be shrunk (or expanded) by a factor λ_1/λ_2.

- A plot along the spectral dimension at the same pixel as before gives us a smooth profile that can be easily modeled with a low-order polynomial fit (Fig.3.5 at right).

- Such a fit is subtracted from the data cube, in order to remove the supposed stellar spectrum. This operation of fitting and subtracting is repeated for each spectrum of the data cube.

After the subtraction of the stellar emission, it is possible to reconstitute the original data cube by resampling the data onto the original spatial scale. During the scaling procedure the planet has been moved away from its original position along the radius vector from the star to the planet: but now, after the resampling the residual planet flux realigns itself. The planet spectrum has been unaffected by the low-order polynomial fit, because it is a high-order term that the polynomial fit cannot reproduce. Fig.3.6 shows a final image obtained collapsing the data cube along the wavelength dimension, and a Jupiter-like planet appears visible with a signal-to-noise ratio around 20.

An alternative way to use IFS for detecting planet will be explained in detail in the next chapters, and it is the basis of the work done during this research: it is a combination of IFS and Simultaneous Differential Imaging, and it aims to take advantage of the simultaneity of the information provided by IFS both spatially and spectrally. This technique is what we call the IFS-SDI technique.

Chapter 4

IFS-based Simultaneous Differential Imaging (IFS-SDI)

From an image obtained with IFS it is possible, after an appropriate data reduction, to create a set of monochromatic images, as many as allowed by the resolution of the disperser. Using these images we can apply a technique of comparison equal to the SDI described in Sec.3.2.2. Each image can be subtracted from one of the others, or from a combination of some of them, in order to find the best way to reduce speckle noise. Marois et al. (2000) showed that the speckle noise reduction can be much more efficient if observations at 3 wavelengths are available, using a “double-difference”: starting from here, it is reasonable to assume that a larger number of images at different wavelengths, taken with a small regular spectral separation, can result in even better reduction of speckle noise.

This is, briefly, the main idea of IFS-based Simultaneous Differential Imaging. The advantage of such a technique with respect to observation with a single slit spectrograph is clearly the possibility to detect the planet even if its position is not known. The advantages with respect to a filter-based SDI can be summarized in this points:

- First of all, with a whole spectrum available we are not forced to study only one spectral feature of the planet. If we have two filters, or three, chosen to observe a specific absorption band, we lose all information coming from the other features. With spectra we can actually combine the data on and off different absorption bands to increase the signal-to-noise ratio of our detection (if there are other good features).

- Second, the availability of data at many wavelengths can allow the development of various algorithms and specific methods for data reduction to improve the reduction in speckle noise. We tried to quantify this improvement with a test done on simulation explained in detail in Sec.6.2.5.

- Finally, the most important reason for using IFS is the possibility of not only detecting extrasolar planets, but also characterizing these objects. In fact, the data available after the subtraction of stellar light allow the study of the spectrum of the planet and its main features, which can be very different according to mass, age, temperature etc. This argument is fundamental to understand that our method can be very useful also in observing planets already discovered in other ways.

Another potential advantage of an IFS, with respect to a conventional dual band imager, is that one can actually make an all-reflective design up to the point where the image is formed, minimizing chromatic errors.

4.1 Instrumental specifications for IFS-SDI

The scientific case imposes to such an IFS-SDI instrument a series of basic requirements, that are presented as follow:

- The spectral range has to be in the Near-Infrared, like said in Sec.3.2.2, because we are searching for molecular absorption bands, in particular of methane.

- A large diameter of the telescope is extremely important because it allows detections of planets closer to their host star (reducing the FWHM of the diffraction-limited PSF), but at the same time the telescope collects many more photons per second. At present, the largest diameters available are on the 8m-10m class telescopes. The development of future Extremely Large Telescopes (ELTs) will improve significantly the chances of detection with this technique.

  Obviously, even a 100m telescope would be not so useful without an efficient AO system. Since the variance of the speckles is strongly dependent on Strehl ratio (see Eq.3.13), it is extremely important to increase it as much as possible. The IFS-SDI technique becomes useful only in case of a previous reduction of speckles by AO.

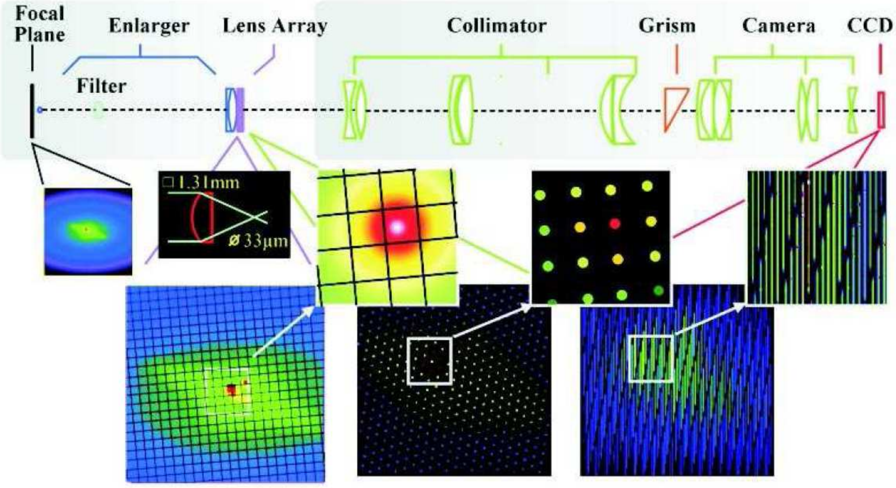

Figure 4.1: Optical layout of SAURON, from Bacon et al. (2001).

- To observe a planet very close to its host star, it will be necessary to obscure the light of the star with a coronograph; so it will be possible to make long exposures avoiding the saturation of the central peak, but also we can reduce the diffraction pattern of the PSF.

- In order to keep the optical design as simple as possible, and to better control non-common path aberrations, a good solution is to use an IFS based on a microlens array, following the ideas of TIGER (Bacon et al., 1995) and SAURON (Bacon et al., 2001). A general scheme of SAURON is presented in Fig.4.1. Every microlens has to cover a portion of sky much smaller than the FWHM of the PSF, in order to sample it in a correct way. A good choice can be to sample this FWHM with at least 4 lenses: this means that the size on sky of the microlens has to be between 0.010 and 0.015 arcseconds, if we are working with a 8m-class telescope. The fore optics of IFS have to be optimized to reach this numbers.

  The optical features of the lenses have to be chosen in order to optimize the spectral area on the detector and to achieve the maximum number of spectra onto it. This means that different shapes and orientations of the array with respect to the detector have to be tested. It has been shown (Antichi J., private communication) that an optimal solution can be to use hexagonal lenses with the diagonal parallel to the dispersion.

- To avoid excessive stray light, circular masks have to be put on the microlens array to cover the borders between the lenses.

- The cross-talk between the spectra must be controlled and kept under a specific level. The separation between the spectra should be chosen following this requirement on cross-talk.
- The choice of the resolution of the disperser should be made very carefully: on one hand it has not to be too high, because the goal of SDI is to enhance at maximum the contrast between the flux on and off the molecular absorption bands (and at the same time, too long spectra would reduce the total number of spectra on the detector). On the other hand, too low resolution creates problems in sampling properly the spectral features (e.g. see Sec.4.2.3). In conclusion, the disperser should provide a very low resolution (we suggest between 20 and 30), constant on the whole spectral range studied.
- Finally, a detector that minimize the various noises (dark current, read-out-noise, etc.) is required. In particular, a very important item is the flat field error.

4.2 Main issues in IFS-SDI detection technique

An IFS-SDI instrument, following the requirements described before, seems to be optically pretty simple and feasible: but at a deep analysis it can present some details that can be sources of troubles in the final realization. In this section we want to focus our attention on some points that required a deep analysis. Each one of these points has to be studied with great attention, because can reduce significantly the chances of detection of the whole instrument.

We introduce here three items: the non uniform illumination of the microlens array associated to diffraction-limited micropupils; the loss of light due to additional masks against stray light; the problem of undersampling of speckles variations with wavelength. In addition, but not discussed here, speckles arising from intermediate planes (out-of-pupil-plane optical aberrations, described in detail by Marois et al., 2006) could be an interesting item for a deep study in the next future.

4.2.1 Impact of not uniform illumination of the lenses

We assume now that each lens of the microlens array generates a diffraction pattern on the micropupil plane: we can approximate this pattern with an Airy disk. But the Airy disk is the result of a uniform illumination of each aperture (microlens), and in general this is not the case, because of speckles. It is expected that a certain number of the diffraction peaks will be quite different from an Airy disk[1] (from simulations: around 10%-15% in case of a single speckle pattern) as a function of the lenslet pitch.

The impact of a not uniform illumination is to increase the wings of the diffraction pattern and to slightly decrease the intensity of the central peak. This means that a certain percentage of lenses will produce a significantly larger cross talk; moreover, a slightly lower value of the central peak mimics a lower transmission of the lens (flat fielding issue). This fraction of "distorted" lenses can generate a significant number of false alarms.

4.2.2 Masks

We have to apply a circular mask to every lens: this mask has the disadvantage of blocking in the best case the 9.2% of light, but its presence is important to avoid stray light at the edges of the lens. This best case is the best geometrically possible: the radius of the circular mask r_m is supposed to be equal to the distance between the center of the hexagon and one of its sides. Mathematically it means that $r_m = (l/4)\sqrt{3}$, where l is the diagonal of the hexagon. But in the real case we expect to use masks with r ~95% of the best possible r_m.

4.2.3 Speckle chromatism and undersampling

With "speckle chromatism" we indicate the chromatic dependence of speckles: they are seen to change size and position as a linear function of the wavelength. In Fig.4.2 is presented a cut of a datacube, showing how the speckles are moving outwards proportionally to wavelength. In order to apply SDI speckles have to be reported to a given size and position, otherwise the subtraction of speckle noise would be not possible. This can be done, as explained clearly in Sec.5.4, rescaling the monochromatic images proportionally to wavelength. In the case of IFS the speckle chromatism creates pseudo-sinusoidal intensity variations along the spectra ("spectral speckles"), whose typical period depends on the inverse of the distance from the field center. Looking at Fig.4.2, we can easily see how a linear cut

---

[1] With the sampling adopted on the detector plane, details of the diffraction patterns are not visible.

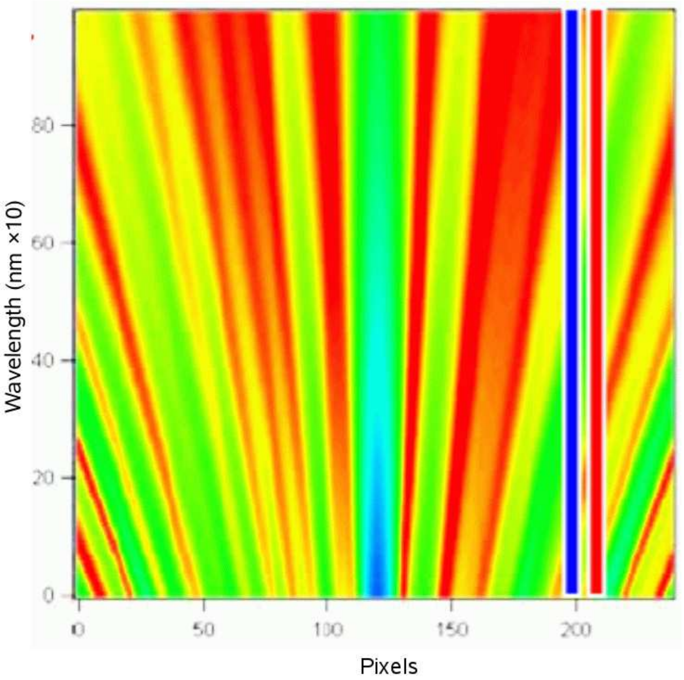

Figure 4.2: Slice of an hypothetical datacube obtained using a coronographic-IFS observation of a star. On the spatial axis the star is placed at x=120. The intensity of speckles is expressed by different colors. It can be seen how speckles maxima (in red) are moving outwards with wavelength. The higher frequency of the pseudo-sinusoidal variation along peripheral spectra (the red and blue vertical lines) can be deduced by the number of speckles maxima passing through it.

parallel to the wavelength axis (which correspond to a linear spectrum) presents a low-frequency variation due to speckles if we cut very close to the center; on the other hand, far from the center the frequency of variation is higher.

Since monochromatic images for IFS are obtained from spectra, an operation of interpolation/rebinning within the spectra is required to go from photons detected per pixel to flux within selected spectral bandpasses. To do this in an appropriate way, spectral speckles have to be sampled according to the Nyquist criterion. We expect that there will be a region, within a certain radius called Nyquist radius (ρ_{NY}), where the spectral speckles can be properly sampled:

$$\rho_{NY} = \lambda_{min}^{2} \frac{R}{D\lambda_c}. \tag{4.1}$$

λ_{min} is the minimum wavelength of the spectra, λ_c the central wavelength of the whole spectral range, R is the resolution, D the diameter of the entrance pupil. Beyond ρ_{NY} spectral speckles will be undersampled and the interpolation of spectra will give wrong results.

Moreover, a good sampling of speckles is possible only if all the micro PSFs (hereafter μ-PSFs) on the detector, at every wavelength, are sampled by at least two pixels. The FWHM of the μ-PSFs depends on the minimum wavelength λ_{min}, on the focal ratio FR_L and the pixel size d_{pix}, on the magnification m_{IFS} of IFS and finally on the $FWHM_{IFS}$ given by the filtering due to the IFS optical quality:

$$FWHM_{PSF} = \sqrt{\left[\left(\lambda_{min} FR_L \frac{m_{IFS}}{d_{pix}}\right)^2 + FWHM_{IFS}^2\right]} > 2. \tag{4.2}$$

In conclusion, an IFS like the one described in this chapter should be strongly affected by speckle undersampling. What is important to know now is how much this can disturb the detection, and if it can be neglected or not.

A more detailed discussion about speckle undersampling can be found on Claudi et al. (2006).

4.3 CHEOPS and SPHERE: Examples of IFS-SDI instruments

As an answer to an ESO call for an instrument finalized to the ground based detection of extrasolar planets, a consortium led by Max-Planck-Institute for Astronomy (MPIA) of Heidelberg proposed in 2001 a project called CHEOPS (CHaracterizing Exo-planets by Opto-infrared Polarimetry and Spectroscopy, Feldt et al., 2003). The CHEOPS instrument aimed to detect extrasolar giant planets using an Extreme Adaptive Optic System assisting two scientific channels: the first was a Polarimetric Analyzer based on ZIMPOL (Povel, 1998; Gisler et al., 2004); the second one was an Integral Field Spectrograph (CHEOPS-IFS, Claudi et al., 2004). A competing project called VLTPF (Very Large Telescope Planet Finder, Mouillet et al., 2004), was at the same time suggested by a consortium led by the Laboratory of Astrophysics of Grenoble (LAOG): this instrument was based on an extreme AO system (Fusco et al., 2006), advanced coronographic devices and the differential imaging camera IRDIS (Mouillet et al., 2004).

After reviewing the two competing phase A studies, ESO has launched a contract for designing and building an instrument benefiting from both studies. This instrument has been called SPHERE, Spectro-Polarimetric High-contrast Exoplanet REsearch (Dohlen et al., 2006). This instrument will include both adaptive optics and coronography from the LAOG project, and all the three scientific channels suggested by the two consortia: IRDIS, ZIMPOL and the IFS.

Three observing modes have been defined for SPHERE:

- A **Near-Infrared survey**, that combines IRDIS dual imaging (mainly in H band) with the imaging spectroscopy given by IFS (in Y and J band). The combination of the two instruments will allow to reduce the number of false alarms and to confirm the potential detections.
- A **Near-Infrared characterization**. IRDIS can be used in various modes to obtain observations with a wide Field of View in all bands from Y to short K either in dual imaging or in broad and narrow-band filters. Spectroscopic characterization will be possible using IFS.
- A **Visible search and characterization** can be performed using the polarimetric capacities of ZIMPOL for reflected light very close to the star. ZIMPOL can provide classical imaging in the visible, offering high-Strehl performance.

SPHERE will be mounted on the Nasmyth focus of the VLT, as can be seen from the model in Fig.4.3. The proposed design of SPHERE is divided into four subsystems: the common path optics, that includes pupil stabilizing fore optics, the SAXO adaptive optics system with a visible wavefront sensor and Near-Infrared (NIR) coronographic devices in order to feed IRDIS and IFS; then each one of the three instrument is a separated subsystem. In this work we are going to study in detail only IFS, while we will not discuss about the other two instruments.

4.3.1 SPHERE-IFS: general description

All the IFS detection ideas described previously in this chapter have been the basis of the development of CHEOPS-IFS. The design of this instrument has been studied in order to satisfy the specifications expressed in Sec.4.1: following the example of SAURON and the considerations made on the possible microlens array structure, the IFS of CHEOPS was composed by 254×254 hexagonal microlenses covering a field of view of $3''.23\times3''.23$. The disperser was an Amici prism, which can give spectra with a nearly constant resolution of R=15 in the spectral region considered, that is included between 0.95 and 1.35μm.

After the CHEOPS phase A study, the project of IFS has been adapted for SPHERE with very few negligible modifications, and the development continued as SPHERE-

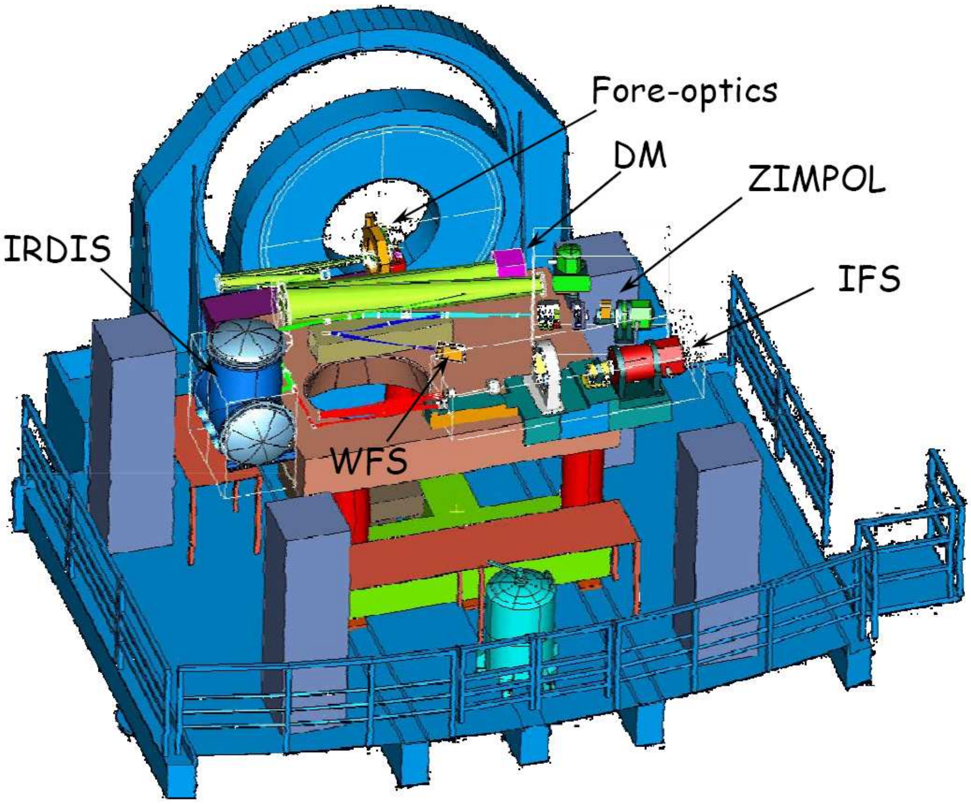

Figure 4.3: Implementation of SPHERE on the Nasmyth focus of the VLT. From Dohlen et al. (2006).

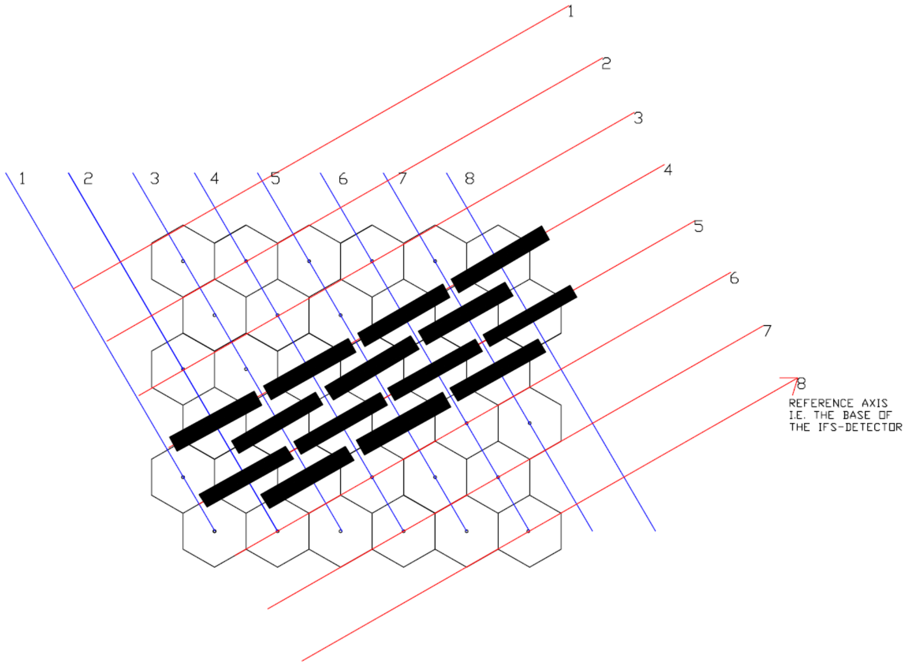

Figure 4.4: Scheme of the disposition of hexagonal microlenses of the simulated IFU. Solid rectangles represent the arrangement of the spectra in the IFS focal plane. This arrangement is the one that optimizes the distribution of spectra over the detector area avoiding a cross talk higher than 10^{-4}. Red and blue lines indicate the orientation of the IFS detector. Figure taken from Claudi et al. (2006).

IFS in the phase B of the project. The work has continued in particular in the details of the optical design.

4.3.2 Optical designs for SPHERE-IFS

The SPHERE IFU is a microlens array composed of hexagonal lenses. The shape and the disposition of the lenslets have been chosen to optimize the spectral area available on the detector (see Fig.4.4). Spectra are parallel to the side of the detector. From Fig.4.5 it is possible to understand the disposition of the optical element in IFS: the microlens array is on the focal plane of the telescope, a collimator introduces the light on the disperser and finally a camera that focuses the light on the detector (inside a cryostat). Different optical designs have been suggested before finding the definitive configuration: for clarity, in this section it is necessary to explain briefly the principal characteristics of these designs.

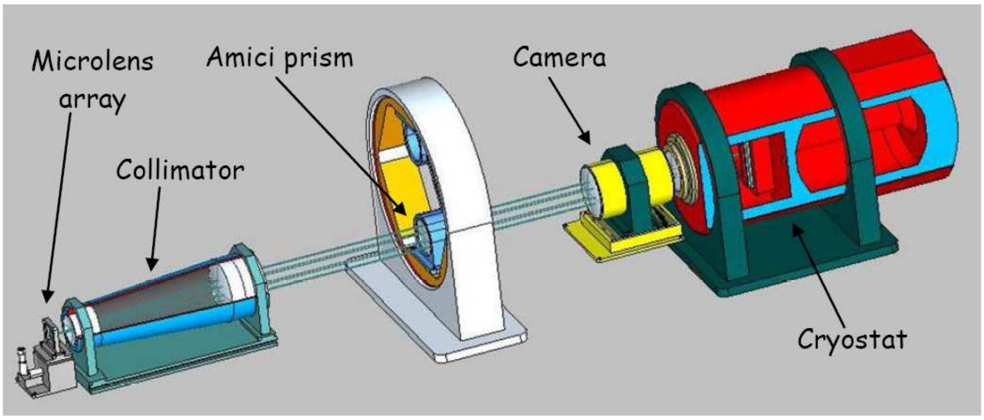

Figure 4.5: Opto-mechanical design of IFS, from Dohlen et al. (2006).

The TIGER design

The original optical design of IFS has been called "TIGER", because of its similarities with the TIGER concept (Traitement Intégral des Galaxies pour l'Etude de leur Raies) described in Bacon et al. (1995). In our case, it presents some modification to optimize it to the high contrast diffraction limited observations. The most important instrumental parameters are reported on Tab.4.1. Summarizing, microlenses are much bigger than the diffraction pattern and provide therefore resolved images of the telescope pupil as entrance slits for the spectrograph. The spatial sampling conditions on the current design impose microlenses smaller than the telescope PSF Airy disk, so the resulting pupil images are no longer resolved, taking themselves the diffraction limited figure of a micro-Airy disk. Since these micropupils are no more spatially limited, this causes cross talk between neighboring pupils and variation of the size with wavelength. The solution suggested during CHEOPS phase A for avoiding this problem was making micropupils much smaller than the detector pixels.

For the TIGER design we used a spatial sampling of 0".0138 per lens, covering a total field of view of 3".23×3".23. The spectral resolution is 15, which means that the spectral region studied is included in around 10 pixels (see Tab.4.1 for the correct values). A schematic description of this optical design is in Fig.4.6.

Such a design has been studied and simulated, but it does not take into account the problems of speckle undersampling described in Sec.4.2. In particular the problems are related to the FWHM of a micropupil, which in this configuration is clearly smaller than 1 pixel and does not satisfy the Nyquist criterium; then to the Nyquist

Radius, that results to be, with the TIGER parameters, around 0.30 arcseconds, according to Eq.4.1: this means that almost every interesting part of the field of view is strongly affected by speckle chromatism and undersampling.

This considerations have brought to the development of a slightly modified optical design, called HYPERTIGER.

The HYPERTIGER design

A comparison between the main features of TIGER and HYPERTIGER is presented in Tab.4.1. Nothing is changing concerning the optical path before the microlens array; the real differences are summarized in few points:

- The **Focal ratio** of the lenses is doubled, passing from 8 to 16;
- The **Magnification of IFS** is no more 1, but becomes 2.16;

Parameter	**TIGRE**	**HYPERTIGER**
Diameter entrance pupil	8.0 m	8.0 m
Spectral range	0.95-1.35 μm	0.95-1.35 μm
Resolution	15	24
Lens pitch	150 μm	150 μm
IFU focal ratio	8	16
Spatial Resolution	0.138 arcsec/lens	0.122 arcsec/lens
IFS magnification	1.00	2.16
Size pixel	18 μm	18 μm
Size Detector	2048×2048 pixels	2048×2048 pixels
Dispersion ($\Delta\lambda$)	0.0382 μm/pixel	0.0181 μm/pixel
Field of view	3″.23	1″.49
Focal ratio of common path	316	316
FWHM of μ-pupil at minimum λ	0.42 pixels	2.08 pixels
Spectral length	10.22 pixels	22.07 pixels
Spectral separation	4.17 pixels	9.00 pixels
Spectral space	14.42 pixels	31.14 pixels
Spectral area	60.07 pixels	280.26 pixels

Table 4.1: Main optical parameters of the two designs presented in Sec.4.3.2. The most important differences are in the focal ratio and magnification of IFS, and on the resolution of the disperser. All the details are described in the text.

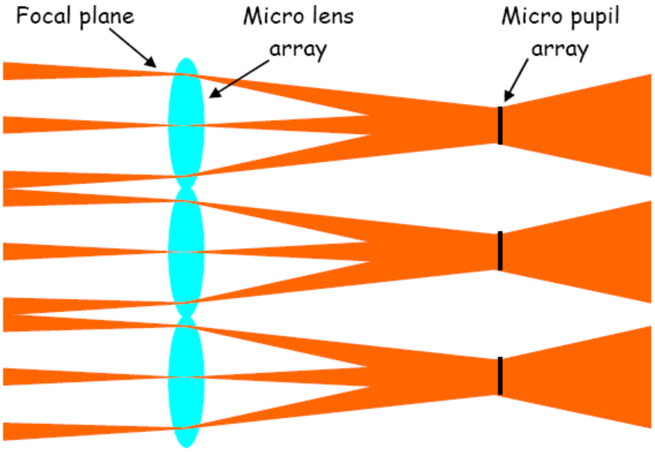

Figure 4.6: Optical concept of TIGER, from Dohlen et al. (2006).

- The **Resolution** and the **Dispersion** change respectively from 15 to 24 and from 0.0382 to 0.0181 μm/pixel.

- Consequently, the **Field of View** of the instrument is reduced: from 3″.23 to 1″.49; this is due to the larger area associated to every spectrum, keeping fixed the size of the detector (2048×2048 pixels).

The new values of magnification and focal ratio are influencing the FWHM of the PSF expressed in Eq.4.2: we pass from the 0.42 pixels at the minimum wavelength in the TIGER case (PSF spatially not sampled), to 2.08 pixels in HYPERTIGER case: the PSF is sampled with at least two pixels as required by Nyquist criterium.

The change in resolution is affecting the Eq.4.1: again at the minimum wavelength, the Nyquist radius passes from 0.303 arcseconds in the TIGER case to 0.486 in the HYPERTIGER case. Since the field of view is reduced because of the large spectral area, in this second case we focus our interest only in the very closest regions to the star, and so the new Nyquist radius is large enough to let us consider the interesting region not affected by speckle chromatism and undersampling[2].

---

[2] The value 1″.49 has to be considered as the diagonal of the square field of view, that will be practically 1″.05×1″.05. In this case the value of 0.486 for ρ_{NY} is not much smaller than half of the FoV (0.527).

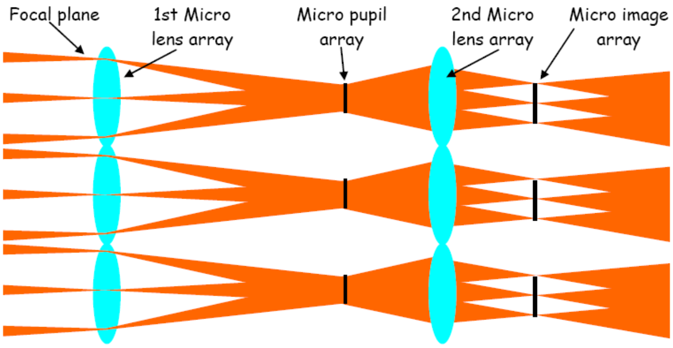

Figure 4.7: Optical concept of BIGRE, from Dohlen et al. (2006).

Other ideas

Another design has been suggested recently, and has been called BIGRE (Dohlen et al., 2006): this concept minimizes speckle aliasing making the spectrograph resolution slit-limited. Practically, a second microlens array, with focal lens shorter than the first one, is added after the micropupil images. This secondary lenses form reduced images of the first lenses, so-called micro images (see Fig.4.7). These micro images are spatially limited, their size does not depend on wavelength, and choosing a pixel scale corresponding to half the micro image width efficiently reduces spectral aliasing with increased pixel efficiency.

This design increase the complexity of the microlens array, but can be a good solution to the problems introduced in Sec.4.2. At present, it needs a better definition by other simulations and additional studies.

4.4 Selection of targets

The direct detection of a faint companion is possible only if the star-planet system satisfies some conditions on distance, separation, age and mass. The possible targets of such a search have to be chosen following specific selection criteria, to exclude all the cases too difficult to achieve. A detailed study about the detection probability can be useful to estimate how many planets we can really expect to detect with an IFS-SDI instrument mounted on a specific telescope.

4.4.1 Selection criteria

In general, the criteria are different if we are looking for cold or warm planets:

Planet	d(AU)	ΔV(mag)	ρ_5	ρ_{10}	ρ_{20}	ρ_{50}	ρ_{100}
Mercury	0.39	24.6	0.078	0.039	0.0195	0.0078	0.0039
Venus	0.72	21.6	0.144	0.072	0.0360	0.0144	0.0072
Earth	1.00	23.0	0.200	0.100	0.0500	0.0200	0.0100
Mars	1.52	26.4	0.304	0.152	0.0760	0.0304	0.0152
Jupiter	5.20	21.3	1.040	0.520	0.2600	0.1040	0.0520
Saturn	9.54	22.9	1.908	0.954	0.4770	0.1908	0.0954
Uranus	19.18	26.2	3.836	1.918	0.9590	0.3836	0.1918
Neptune	30.06	27.4	6.012	3.006	1.5030	0.6012	0.3006
Pluto	39.44	33.7	7.888	3.944	1.9720	0.7888	0.3944

Table 4.2: Magnitude differences with respect to the Sun, semi-major axis of the orbits, and separations (ρ) of Solar System planets as viewed from different distances (respectively 5, 10, 20, 50 and 100 parsecs). Separations are expressed in arcseconds.

- **Cold planets**: The luminosity of the planet is strongly related to the physical separation with its host star ($L \propto d^{-2}$, see Eq.3.1). This means that the luminosity of the planet will decrease with separation, and we can observe it only in the closest region to the star. Considering the PSF given by an 8m-class telescope and an AO able to reach a S of 0.9, and at the same time the faintness of the planet at large separations, we expect to be very difficult the detection of cold planets beyond 5-10pc. In order to make a comparison, we present in Tab.4.2 the list of the Solar System planets, their difference in magnitude with the Sun and their angular separation if seen from 5, 10 and 20pc: it is interesting to notice that only a planet on a Neptune-like orbit can be seen with an angular separation larger than 1 arcsec from 20pc.

  The cold planets, shining by reflected light, are usually part of old systems, which means that they can be found around old (more than 1 Gyr) main sequence star. The advantage of old stars is that they represent the larger fraction of nearby stars. Since the light reflected by the planet is proportional to the light emitted by the star, we do not expect differences in contrast as a function of the stellar type of the host star.

- **Warm planets**: Luminosity of young warm planets is not affected by the sep-

> aration d (unless it is very close to the star, see Eq.3.3). Therefore, the observation of companions at very large separations is not only possible but even easier than at short separations. Our target list is limited then more by the faintness of the planet if it is farther out from the Sun, than by the separation: it can include all the young stars up to 100pc (separations beyond 20-30 AU).
>
> The warm planets are supposed to be found in young planetary systems. Young stars (i.e. 100 Myr old or younger) are rare with respect to the old ones in solar neighborhood. The range of distances we considered includes a series of nearby associations, namely the TW Hya association, the Tucana-Horologium association, and the β Pic moving group; moreover many isolated young nearby stars can be good targets, e.g. the M-dwarf GJ 182.
>
> In the case of warm planets, the luminosity is produced practically only by intrinsic thermal emission: therefore, this emission is not changing with the spectral type of the host star (we are still not considering the Hot-Jupiters or Roasters that are very close to the star and heated by its radiation), and the contrast is lower if the star is faint. Thus, warm planets around young M stars should be easier to detect than around solar-type stars, and they are in principle the most favorable targets.

For CHEOPS and SPHERE a detailed work of selection of targets and estimation of the detection probability has been carried on by Desidera (2006); here we summarize the strategy adopted and the main results of this work.

The target list has been prepared selecting all stars in HIPPARCOS catalog within 20 pc (parallax $\pi > 50$ mas) in the declination range $\delta <$ +20° (to be observed using VLT). The few stars with magnitude $I > 10.0$ have been not included because too faint. Since HIPPARCOS catalog is complete only for magnitudes $V < 7.5$, there are many stars, mostly M dwarfs, sufficiently bright but missing from the list.

On the other hand, a second list of young targets (up to ~100 Myr) has been prepared, selecting from HIPPARCOS catalog the stars up to 100 pc ($\pi > 10$ mas). The limit in magnitude is again $I < 10.0$ and the declination range is $\delta <$ +20°.

4.4.2 Detection Probability

Using the target lists defined in the previous section, it has been possible to estimate the detection probability for SPHERE IFS. This has been done using Monte Carlo simulations considering the statistical data we can derive from radial velocity detections. Two key factors have been included: the probability that the targets host planets in the range of separation observable with SPHERE IFS, and the probability that SPHERE IFS will actually detect these planets. Only single-planet systems are considered in the simulations.

Mass, period and eccentricity distribution

According to Lineweaver & Grether (2003) the period and mass distribution of extrasolar planets found by radial velocity surveys can be described by

$$\frac{dN}{d\,(M\sin i)} \sim (M\sin i)^{\alpha} \quad \text{with} \quad \alpha = -1.8 \pm 0.3 \tag{4.3}$$

$$\frac{dN}{dP} \sim P^{\beta} \quad \text{with} \quad \beta = -0.3^{+0.3}_{-0.4}. \tag{4.4}$$

In the simulation of probability this distribution is adopted, keeping in mind that the range of separation explored by SPHERE IFS lies mostly outside the range explored by radial velocity surveys and therefore the derived extrapolations suffer from fairly large uncertainties.

A cut-off with no planets has been set with $P > 70\,\mathrm{yr}$ ($a > 17\,\mathrm{AU}$ for solar mass stars), and the study is also limited to planets with masses larger than Saturn ($M \geq 0.3\,M_J$), because of the large uncertainties on the frequencies of planets below this limit. The distributions of mass and period are considered to be independent[3].

Finally, the eccentricities are supposed to be uniformly distributed in the range between 0 and 0.6.

Frequency of planets

The absolute frequency of planetary companions given by radial velocity surveys is related mainly to F, G and K stars, and it is a function of time span on the surveys, of radial velocity precision and of the activity level of the star. Anyway, it has been possible to estimate the fraction of stars with planets for different surveys (see e.g. Lineweaver & Grether, 2003; Fischer et al., 2004; Mugrauer et al., 2004). The results led to the adoption of an average frequency of 9% for planets within

---

[3] According to Udry et al. (2003) this is not true: there is, for example, evidence of a paucity of very light planets ($m < 0.75\,M_J$) with $P > 100$ days. This should have impact for this work, but it needs more planet discoveries for a statistical confirmation.

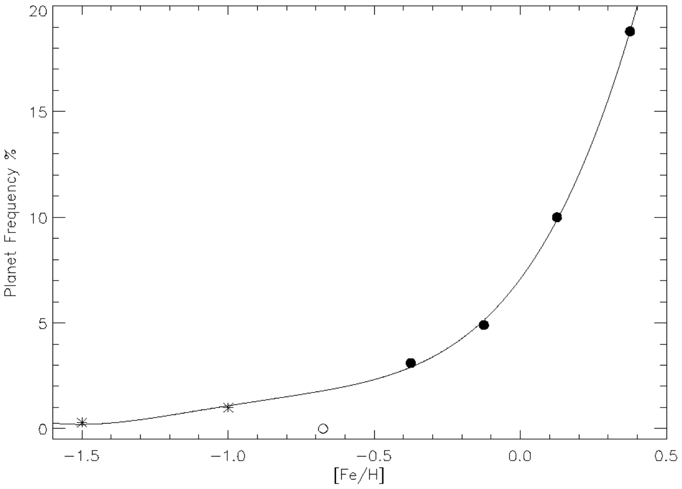

Figure 4.8: Adopted dependence of planet frequency on metalicity (solid line). Circles are the observed points from Fischer et al. (2004). The lowest metalicity bin (empty circle) was not used because of its low significance. Two points at [Fe/H]=-1.0 and -1.5 have been arbitrarily added.

5.5 AU and $M \sin i$ 0.3-15 M_J (Lineweaver & Grether, 2003).

This result seems to be anyway strongly dependent on the metalicity of the star: Fischer et al. (2004) found the dependence shown in Fig.4.8, that has been adopted in the simulations. A dependence on the stellar mass resulted to be negligible for F, G and K stars (Laws et al., 2003), but the paucity of planets detected around M stars with respect to solar mass stars appears to be more relevant. Since in the probability simulations this effect has been neglected for all the stars, and many of the best targets are M stars, the detectability may be overestimated. Finally binary and multiple system have to be considered; we expect to find planets only in stellar systems wide enough to make the gravitation influence of the companion not too much disruptive. Since current data do not allow the derivation of planet frequencies for binary systems, the standard frequency are assumed also for binaries: however, for each planet the dynamical stability can be checked using the results by Holman & Wiegert (1999), and if the planet lies outside the stability boundaries it is not considered detected.

Luminosity contrast

The adopted luminosity contrast is derived summing the intrinsic and reflected contributions from the planet (see Chapter 1). This is an approximation, considering that the additional heat source represented by the stellar irradiation can slow down the cooling of the planet. However, for the large separations considered this effect is small at young ages, and for old planets this intrinsic luminosity is still smaller than the reflected one (at the wavelength of interest for SPHERE).

4.4.3 Monte Carlo simulations

The chance of detecting planets with SPHERE IFS can be estimated using a Monte Carlo simulation which performs the following steps:

1. Normalization of planet frequency for stellar mass and metalicity;
2. Random generation of all orbital elements and masses according to the adopted distributions;
3. Calculation of physical and projected separations;
4. Calculation of the luminosity contrast;
5. Evaluation of detectability, and exclusion of planets whose presence is not allowed according to dynamical stability.

Anyway, a detailed result is possible only combining this Monte Carlo estimation with a simulation of the whole instrument. This should provide the detectability as a function of the separation and the Point Spread Function given by the instrument. This second simulation is presented in Chapter 5 and following.

30 000 planets were generated for each star of the preliminary target list. For example, Fig.4.9 shows the contrast between a 1 Gyr old G2V star at 5 pc from the Sun and the simulated planets: there is a clear separation between planets visible for intrinsic thermal emission (lower part) and for reflected light (upper part). The very sharp increase of the number of planets at cold/warm planets transition makes the reach of this contrast limit decisive for the number of planets to be discovered by SPHERE IFS.

The 20-pc sample consists of more than 650 stars, and the results of simulations, in terms of number of planets detected and probability to detect at least one planet, are shown in Tab.4.3. In conclusion we can say that a detection of about ten planets is actually expected. Half of the chances of finding planets is confined in the best 80 targets.

For the young stars between 20 and 100 pc SPHERE IFS can reach a sensitivity down to masses below 1 M_J. But considering the large distances of the sample, the

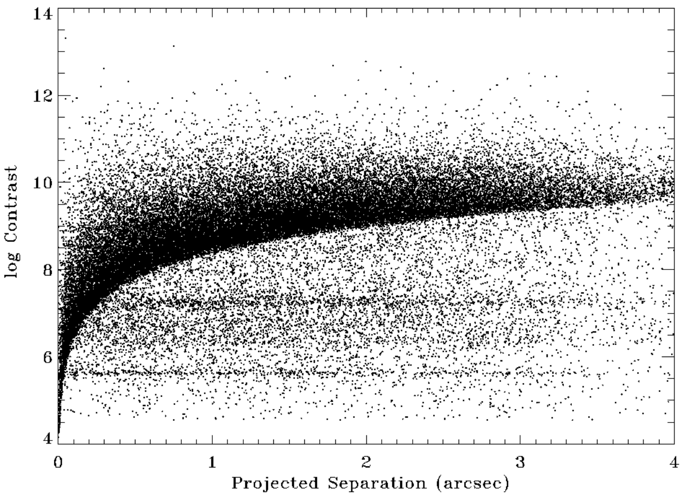

Figure 4.9: J band luminosity contrast vs projected separation for the Monte Carlo simulation of 30 000 planets around a G2V, 1 Gyr old star at 5 pc from the Sun.

N_{stars}	$N_{planets}$	$P_{1planet}$
5	0.95	0.6534
10	1.53	0.8124
20	2.25	0.9119
50	3.93	0.9843
100	5.64	0.9972
150	6.86	0.9992
200	7.73	0.9997
300	8.67	0.9999
400	9.20	0.9999
500	9.61	0.9999
600	9.83	1.0000

Table 4.3: Number of expected planets detections ($N_{planets}$) and probability of detection of at least one planet ($P_{1planet}$) as functions of the number of stars considered in the simulations, sorted accordingly to the probability of planet detection (only for the 20 pc sample).

circumstellar zone explored for the presence of planets is typically beyond 10 AU, where the actual abundance of giant planets is not constrained by current data.

Since only planets up to semimajor axis $a \leq 17$ AU have been included, no more of 5-6 detections are expected (among around 100 stars); if one considers a nearly flat distribution in semimajor axis up to 40 AU the number of expected detections grows to 43, but this distribution appears not very realistic with the current knowledge of planet formation.

Finally, from these detailed estimates of the probability of detecting planets, it results that on the whole the best candidates come from four different groups of objects:

- Planets orbiting very young stars within 20pc, mostly members of the β Pic moving group (Zuckerman et al., 2001): for these stars we have the largest detection probability;
- Rather old planets around very nearby stars: they have to be actually quite close to the parent star to be detected, in order not to be beyond the field of view of the instrument;
- Very young planets, not very close to us: they have to be very far from the central star, otherwise they would fall in the central glare of the parent star.
- Planets around stars at intermediate ages and distances, but members of the Ursa Major cluster (Soderblom & Mayor, 1993), for which an IFS-SDI instrument should be able to reveal planets similar to Jupiter in both mass and separation from the central star.

Chapter 5

Simulation code: goals and main ideas

5.1 Importance of simulations

In the previous chapter we presented briefly the general outline of the Integral Field Spectrograph for SPHERE. Since the technique is quite innovative, to achieve the detection of planets as in the requirements the optical design of the instrument has to be studied in all the details to reduce any source of noise. A complete set of simulations is required in order to:

- Clarify whether our technique, based on integral field spectroscopy, extreme adaptive optics and simultaneous differential imaging, will be able or not to reduce speckle noise enough to allow the detections;
- Establish in a quantitative way what are the physical properties of the objects we can actually observe, in terms of masses, distances, angular separations etc.; determine what should be the result achievable in case of not-so-good or bad seeing;
- Estimate the most suitable parameters of the optical design;
- Quantify the consequences of some secondary effects, e.g. the inhomogeneous illumination of lenses or the speckle chromatism as described in Sec.4.2; to test the agreement between theoretical arguments and simulated results;
- Finally, as already said at the end of the previous Chapter, contribute significantly to the preparation of a target list for the IFS-SDI observations.

The required simulation code must be able to reproduce both the physical features of the observed system and the passage of light through the instrumentation. It must reproduce the IFS exactly as it is going to be in the real case; besides, it must reproduce as many as possible sources of noise, from the photon noise to the atmospheric turbulence and the detector features.

The development of this code, written in IDL, has been started during the phase A of the CHEOPS project and has been named CHEOPS Simulation Program (CSP). The same code is used and implemented in the phase B of SPHERE. It is a "living" software, because it is continuously improved and changed in accordance with the development of the SPHERE optical design; nevertheless, after a set of intermediate steps (Berton et al., 2004a, 2006a,b), we have reached now an almost complete and versatile version.

5.2 Introduction to the code

5.2.1 Input parameters

The code needs many informations that must be defined time by time, and each variation will cause changes of the detectability of the companion. It asks for these information in the beginning, in a ASCII files that can be prepared in advance with a text editor. Anyway, input parameters are splittable in different groups with different features. A summary of all the parameters is in Tab.5.1.

Instrumental parameters

In this first group we must define the features of the telescope and the instrument. Also additional information about the observation has to be provided.

Data about the telescope (primary diameter, secondary obstruction, etc.) and the optical quality of the instrument are used to calculate how many photons are expected to reach the detector. The optical features of IFS lenses are described by some parameters like the pitch, the magnification, the focal ratio and so on. To simulate the dispersion of light some spectral informations are required (dispersion $\Delta\lambda$, preferred to resolution; initial wavelength, etc.).

About the detector, we have to specify which kind of detector we are using (size of a pixel, total collector area, etc.), focusing the attention on the noises like read out noise. An important issue will be the flat field error, at the moment presented as a random factor of multiplication for each pixel: this error is required to be $\leq 10^{-4}$, and this is the value assumed for simulation, even if the feasibility of this result is actually under discussion (see Sec.6.2.1).

All these parameters, which are single floating numbers, will be included in the ASCII general data file.

Atmospheric turbulence and entrance pupil

To represent the atmospheric turbulence and the correction provided by AO, we chose to use a set of phase screens, which means bi-dimensional arrays (.FITS files). Each phase screen refers to a specific moment in time that can be considered instantaneous. The difference in time between the screens has been called *tau* and it is usually shorter than the expected coherence time, to simulate correctly the evolution of the turbulence. This parameter is included in the general data file.

Since the exposure time required is usually larger than or equal to few seconds, and *tau* is of the order of 1 ms, we need to prepare in advance a set of thousands phase screens[1].

A second .FITS file has to be provided to describe the entrance pupil of the telescope (in particular the position of the spiders). Both this pupil, and the phase screens, have to be built with the same pixel-per-meter scale, because they will be combined together to form the telescope PSF (see Sec.5.3.2). This scale (*ppm*) is included in the general data file.

Physical features of the planetary system

Some parameters, like the distance of the system from the Sun, are in the general data file. The position of the planets (physical separations, position angles) are provided by the code as a function of the distance. The spectra of planets and star have to be provided separately in two .ASCII files, preferably as a two-columns table: first column wavelength and second one flux. The chosen units are meters for the wavelength and $\frac{W}{\mu m \cdot cm^2}$ for the fluxes.

The dispersion of these spectra has to be the same, and possibly much smaller than the expected dispersion of IFS. This because we want to be sure to oversample

---

[1] A new approach, that would help reducing the computer time needed, suggests the use of a certain number of completely uncorrelated phase screens, because in simulating hours of exposure time the atmospheric speckles become negligible in comparison to quasi-static aberrations. Anyway, is still not clear what is the correct amount of screens that have to be simulated.

the spectra, avoiding discontinuities (see Sec.5.3.2). The dispersion of these spectra, like the total number of elements, is one of the parameters in the general data file.

A third spectrum, with same dispersion and number of elements, is saved in another .ASCII file and represents the background sky emission lines. The absorption lines of the sky should be better added as a component of the stellar spectrum.

5.2.2 Expected results - Outputs

At the end of the elaboration, the code must prepare an image file showing the final image of spectra (.FITS file) like the one expected by the real instrument. The analysis of this image has not to be done by this code, but by the analysis code presented in Sec.5.4. Besides, the code can temporarily store a set of additional images that can be useful in testing the procedure: this images are

- The monochromatic images of the light passing through IFS, that means images of micropupils not dispersed;
- The monochromatic telescope PSFs obtained without IFS.

These last two sets of images are not relevant for scientific analysis of the results, because they are not really produced by the instrument during the real observations.

5.2.3 Main goals of the CSP code

The work done by the code can be divided in a series of intermediate goals to reach, starting from the input parameters listed in Sec.5.2.1:

1. **Creation of the PSFs of the star and the planet**. In the beginning, star and planets are point-shape sources, with different flux as a function of the wavelength: after fixing a wavelength λ, the entrance pupil of the telescope (characterized by a given diameter D, the secondary obscuration and the spiders), will transform these point-shape sources in diffraction limited PSFs with a characteristic size of $\sim \lambda/D$. But the code must take into account the passage of light through the terrestrial atmosphere: the turbulence of the atmosphere generates the atmospheric speckles and the seeing disk, as described in Sec.3.2. Moreover, additional speckles (called *super-speckles*) are generated by quasi-static aberrations: they appear similar to atmospheric speckles, but they have a much longer life time, and in the worst case they do not change

Parameter	Description	Unit
dmt	Telescope diameter	m
ost	Secondary mirror diameter	m
eff	Total efficiency of the instrument	-
nilx	Pitch of a microlens of IFS	μm
arpitch	Projection of the pitch of IFS as angular sep.	$arcsec$
magnifs	Magnification of IFS	-
fr	Focal ratio of IFS	-
siz	Size of the phase screens	$pixels$
ppm	Pixel-per-meter scale of the phase screens	$pixels/m$
lmscreen	Wavelength associated to the phase screens	m
tau	Life time of a phase screen	s
ti	Integration time	s
tf	Total exposure time	s
bas	Dispersion $\Delta\lambda$ of IFS	$m/pixel$
as	Dispersion $\Delta\lambda$ of the input spectra	$m/pixel$
lmb	Minimum wavelength considered	m
lmq	Maximum wavelength considered	m
lsst	Number of elements in the input spectra	-
dis	Distance of the planetary system from the Sun	pc
pix	Size of a detector pixel	μm
ron	Detector read-out-noise	e^-
gain	Detector gain	e^-/ADU
flf	Detector filling factor	-
fferr	Flat field error	-
qeff	Detector average quantum efficiency	-
dark	Dark current	e^-/s

Table 5.1: Input parameters included in the general data .ASCII file. They are here presented in groups related to: Instrumentation, atmosphere and exposure times, spectral features, physical features of the system, detector. The first column presents the name of the variable in the code; the second one describes briefly the parameter; the third column presents the unit ("-" for multiplicative factors without unit). Details can be found in Sec.5.2.1.

during all the exposure.
The presence of an extreme adaptive optic system (hereafter XAO) will modify the resulting PSFs, reducing the intensity of the speckles and increasing the central peaks of star and planets. Atmospheric turbulence, static aberrations and XAO correction are introduced as phase screens, and the PSF is obtained using Fast Fourier Transforms (FFT). From this procedure the code obtains a set of PSFs each one related to a given λ.

2. **Simulation of the microlens array**. The core of IFS is the array of microlenses. The code, for each image, has to calculate the amount of light passing through every microlens. Because of the optical design of IFS (TIGER and HYPERTIGER designs, see Sec.4.3.2) every lens focuses the light in a diffraction limited PSF which size depends on the focal ratio, the pitch of the lens, the magnification and, obviously, the wavelength. The result is a new set of images, one for each wavelength considered, reproducing the monochromatic micro-PSFs on the focal plane of the array.

3. **Simulation of the disperser**. All the images have to be combined in a single image of spectra. This can be done only at the end, when all the required wavelengths have been considered. The reconstruction of a continuous spectrum from discrete images does not create problems because we use a number of λ's much higher than the number of spectral pixels, as explained in detail in Sec.5.3.2. The final output, that is the image with all the spectra, is then obtained.

4. **Analysis of spectra**. A preliminary procedure of data analysis and reduction is required, at this point, to quantify the actual reduction of speckle noise and the signal-to-noise of the detected planet. This procedure cannot be complete like the real final data reduction pipeline, but has to be accurate enough to allow the understanding of which kind of errors and problems are introduced during the analysis of spectra.
   This part of the software is a secondary code, at the moment called CSP-ANALYSIS, also written in IDL, that will be briefly described in Sec.5.4. This code can be used as a basis for the future data analysis pipeline.

5.3 The code in detail

In this section we present in detail all the passages of the CSP simulation code summarized briefly in the previous section. This version of the code, presented in Berton et al. (2006a), is the one optimized for the TIGER optical design, with a simple Lyot coronograph. For further improvements of the optical design, slight changes of the code have been lately introduced.

5.3.1 Simulation of atmospheric turbulence and AO correction

Data concerning atmospheric turbulence, telescope vibration and Adaptive Optics correction are elaborated as a set of images, phase screens, which represents the wavefronts associated with observations provided by AO. A phase screen of the atmospheric turbulence is produced defining the spatial properties of the screen by a von Kármán spectrum, using a procedure based on Lane, et al. (1992). A single layer atmosphere was simulated corresponding to seeing conditions of 0″.6, 0″.85 and 1″.0 at λ =550 nm. The coherence time τ_0 was always 0.01 s. Telescope vibrations were added as time-dependent tip and tilt terms at 14 Hz and 48 Hz with amplitudes typical for the VLT; an ADC is supposed to be present within the AO system. As this work is not concerned with the details of the AO system, a very simple AO simulation technique was adopted where the wavefront sensor is simulated by re-sampling the input wavefront itself to the sensor resolution of 40 apertures across the 8.0 m primary mirror. This corresponds exactly to the number and geometry of the actuators in the assumed deformable mirror. The "sensor" information was fed into the control loop which uses a simple integrator controller running at a loop speed 2 kHz. This controller produces another 40×40 matrix which represent the mirror commands. Since it is still in the same units as the wavefront itself, the rest of the system is simulated simply by re-expanding this 40×40 matrix to the original spatial scale of the wavefront and subtracting it from the input phase screen appropriate for the moment in time when the mirror signals are applied.

Simulating AO in this way we do not include specific effects of certain wavefront sensor types and other specialties, but we do get a rather optimistic estimate what an XAO system could achieve on an 8 m telescope. Static aberrations are also present. The resulting Strehl ratios vary between 0.4 and 0.8. It should be noted that with this technique we do see a strong dependence of planet detectabilities from seeing values (see Sec.6.2.2), but since the AO simulation is not really detailed, one should rather assume the Strehl number as the input variable of that dependency. How the Strehl ratio depends on seeing has to be determined in detailed AO simulations not included in this work. On the output side of the atmosphere-AO simulation chain, every phase screen represents the wavefront at a precise moment of the observation and it is related to a very short interval of time. This interval is shorter than the coherence time of the turbulence. Each screen differs slightly from the previous one. Phase screens are monochromatic, but they can easily be converted to the required wavelength using appropriate scale factors.

5.3.2 Creation of the PSF and the speckle patterns

Given a phase screen, generated for a certain wavelength λ_0, and the entrance pupil of the telescope, the code transforms the phase screen, a measure of phase φ, in an electric field $E = Ae^{i\varphi}$, where the amplitude A is given by the pupil and φ by the phase screen. The PSF related to that screen is obtained using a Fourier Transform:

$$psf = FT(E) = \iint_{-\infty}^{+\infty} E(x,y)\mathrm{e}^{-i2\pi(f_x x+f_y y)}\mathrm{d}x\mathrm{d}y, \tag{5.1}$$

where f_x and f_y are the coordinates in frequency space.

We simulated a simplified model of Lyot coronograph, in order to avoid the saturation of the central peak. Such a coronograph would also be useful in reducing the effects of diffraction rings and patterns. It is included by applying on the focal plane a central obscuration (with a diameter of 0.55 arcseconds at the shortest wavelength) covering the central stellar peak, and then a Lyot mask on the pupil plane. This has been modeled as an aperture on the pupil plane with transmission equal to 1 within 95$\%$ of the diameter of the pupil of the telescope, and it is slightly apodized beyond this value using a Gaussian function. All these choices have been totally arbitrary because the final configuration of the coronograph for IFS has been not decided yet: actually, it has been shown that a Four-Quadrant Phase-Mask coronograph would be a better choice to allow detections very close to the star (Dohlen et al., 2006). When the definitive structure of the coronograph will be chosen, we will be able to improve the simulation of this part of the code. For the moment, we stick with this simplified model.

Before simulating the coronograph our code introduces the "object" image that is a set of point-like sources, the star and one or more planets, characterized by different intensities. The intensities are provided as a function of the wavelength at which the code is working. In this way the simulated PSFs are related with a specific resolution element of the spectrum.

Every PSF has been obtained from a single phase screen. Therefore, it is related to an interval of time shorter than the coherence time τ_0 and it will be characterized by an instantaneous speckle pattern. In order to simulate a longer exposure time we perform a suitable number of repeats and sum the resulting PSFs into one.

Moreover, every PSF produced in this way is strictly monochromatic, and can be reported from λ_0 to the required wavelength λ using an appropriate rescaling. In principle, we are using at this step only the central wavelengths of the spectral intervals defined by resolution: one can argue that since the resolution is very low and the spectral resolution elements are quite large (concerning TIGER design, with R=15 in the near-infrared we expect a $\Delta\lambda$ ~0.04μm) it will be not possible at the end to build correct continuous spectra using a set of discrete wavelengths separated by ~0.02μm. We solved this problem in a statistical way exploiting the fact that the typical lifetime of a phase screen is a fraction of a millisecond, while a simulated exposure time is usually much larger than 1s. For every phasescreen we calculate the PSF not at the wavelength λ, center of the resolution element, but at $\lambda \pm \lambda_r$, where $\lambda_r \leq \Delta\lambda/2$ is a small random value. After a large number of phasescreens considered, with this procedure we have enough different values of λ_r to sample all the element uniformly. For this reason, we see an elongation of speckles due to their chromaticity even in an image nominally related to a single wavelength (see Fig.5.1).

We also note that the speckles seem to form a sort of bright ring: this is a characteristic feature of XAO: the central part of the image is better corrected than the external region, and the radius of this "ring" is $\sim \lambda/2d$ where d is the distance between the actuators of the deformable mirror. This radius is also called the Control Radius and is ~0".5 at the shortest wavelength (0.95μm) in this application.

The PSF simulated in this way has been compared with real observed data obtained with NACO-SDI at VLT, adapting the input parameters for this specific case. The results showed a good correspondence between the simulated speckle noise and the measured noise, and give confidence in the simulation (Berton et al., 2004b).

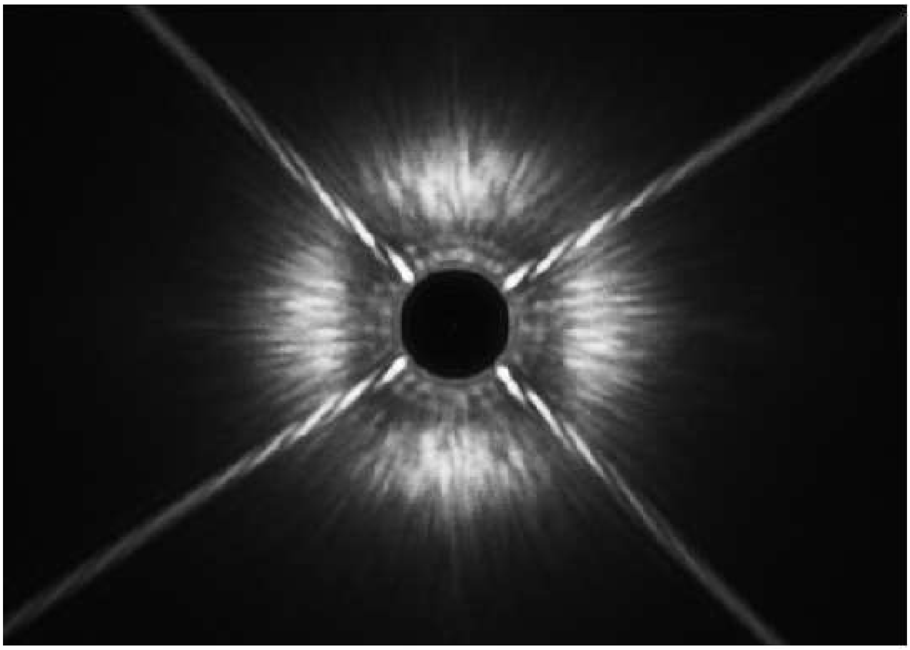

Figure 5.1: Simulated Point Spread Function of a G0 V star at the VLT (prototype of an 8m-class telescope). It corresponds to an integration time of 0.5s, with a Strehl Ratio $\sim$0.8 at λ=1.0μm. The width of the simulated resolution element ($\Delta\lambda$) is 0.04μm. VLT's spiders are clearly visible, as well as the central obscuration with a diameter of 0″.55 due to the coronograph.

5.3.3 The Integral Field Unit and the disperser

The simulated IFU is a microlens array composed of 254$\times$254 hexagonal lenses. The shape and the disposition of the lenslets have been chosen to optimize the spectral area available on the detector (see Fig.4.4). As explained in Sec.4.3.2, for the TIGER design we used a spatial sampling of 0″.0138 per lens, covering a total field of view of 3″.23$\times$3″.23, and to avoid stray light from the gaps between the lenses, we applied a circular mask to every lens.

Each microlens of the IFU array samples a small portion of the PSF, and creates its own small PSF which is imaged onto the detector by the IFS optics[2]. The location of these PSFs depends on the geometry chosen for the array and on the size of the lenslets. In SPHERE IFS the optical design has been optimized to keep the cross talk between the lenses below 10^{-4}, in order to be negligible.

The code considers each lens separately, applying a standard PSF given by the diffraction pattern of a uniformly illuminated circular aperture:

---

[2] After the microlens array the diffraction of the lenslets is dominant: for this reason, we do not have micropupils on the detector but diffraction limited PSFs (see Sec.4.3.2).

Parameter	Used value
Read out noise	10 e^{-}
Gain	1 e^{-}/ADU
Filling factor	0.9
Flat field error	10^{-4}
Bit resolution	14 bit
Average quantum efficiency	0.6
Dark current	0.1 e^{-}/s
Full well	30 000 ADU

Table 5.2: Main detector parameters introduced in the simulations.

$$i(\vartheta) = i(0)\left[\frac{2J_1\big(v(\vartheta)\big)}{v(\vartheta)}\right]^2, \tag{5.2}$$

where ϑ is the distance from the center, J_1 indicates the Bessel function at 1^{st} order and $v(\vartheta) = 2\pi\vartheta/(\lambda F)$ with F being the focal ratio. The next step is the simulation of the disperser. Since the images we simulated up to now (stellar PSF and microlenses) are related to a single resolution element of the spectrum, thus almost monochromatic, we need to repeat the entire procedure in order to simulate all the different wavelengths of the considered spectrum. Every modification in wavelength causes two effects on the speckles on the AO focal plane: a radial shift with respect to the stellar center and a change of the size of both the diffraction figures and the speckles. Moreover, the PSFs of the microlenses will also change. In addition, the fluxes of the star and of the planets must change with wavelength according to their spectra. Final images after the simulation of the IFU for all different wavelengths must then be combined on the detector in order to obtain the observed spectra, shifting the micro-PSF images slightly in a way proportional to their wavelength.

Finally, before concluding the procedure, all noise sources related to the detector are added to the image. These noise sources include read out noise, residual flat field etc. The contributions to noise are computed considering the values appropriate for the most important near-infrared detectors available at present. The used values for the various parameters characterizing the detector are summarized in Tab.5.2. An example of the output of the whole simulation is presented in Fig.5.2.

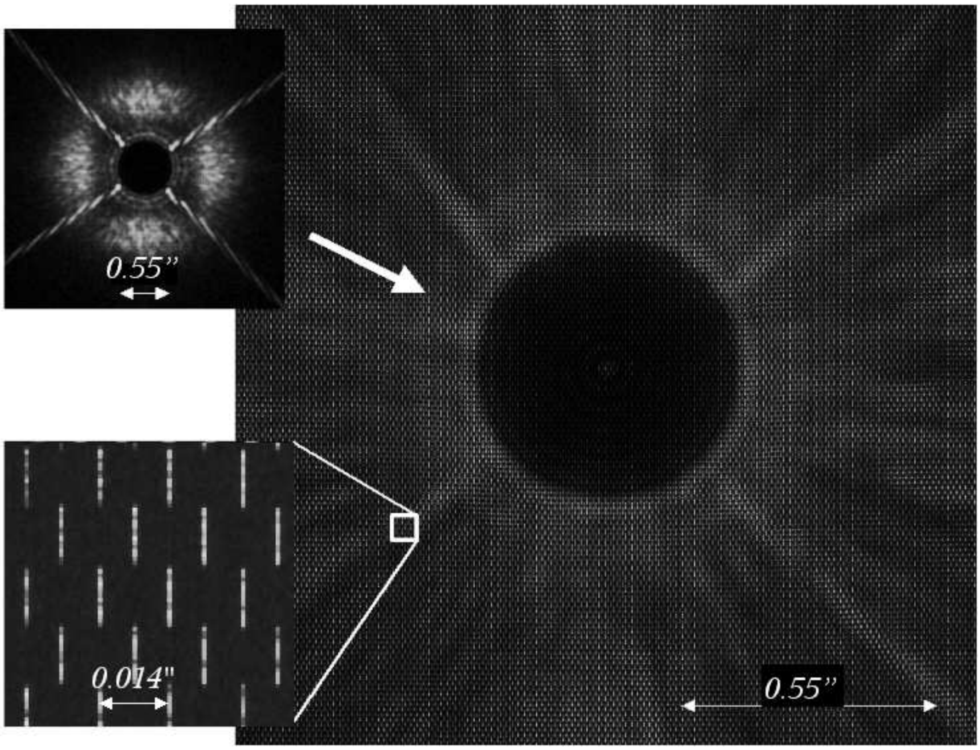

Figure 5.2: Final output of an IFS observation of a star, in the case of the VLT and with the details described in the text. At top left, an example of PSF (with coronographic mask, spiders and AO correction) is presented. After the simulation of IFU and disperser we obtain the large image. At bottom left details of the spectra can be seen. Separations are expressed in arcesconds. The spectra cover the spectral region between 0.95 and 1.70μm, with a resolution of 15, so their spectral length is about 20 pixels.

5.4 Analysis of results

Fig.5.2 clearly shows that the spectra in the final image are not as regular as expected from the model of the stellar spectrum shown in Fig.1.3. The dependence of fluxes on wavelength apparently follows a pseudo-sinusoidal law. This is due to the shift of speckles from one microlens to another with changing wavelength. This effect makes it impossible to do a simple comparison of the spectra for detecting the planet. For this reason, following the example of Sparks & Ford (2002), we must extract all data related to every single resolution element from all the spectra in order to rebuild a set of monochromatic images that can be, at this point, rescaled in size by a factor equal to λ_0/λ. Scaling all the monochromatic images at a specific λ_0 makes the speckles coincide in position and size, so that a subtraction becomes possible. An example of rebuilt monochromatic image is shown in Fig.5.3.

The algorithm for subtraction can be different depending on the nature of the planet. In this first analysis, we decided to follow the idea of double-difference presented by Marois et al. (2000), using three images I_1, I_2 and I_3 obtained by three resolution elements λ_1, λ_2 and λ_3 (Eq.3.16). With a number of wavelengths available larger than 3, we could apply Eq.3.16 to various combinations of images, investigating different spectral features and using the entire information given by the spectra, as explained in Sec.4.

An example of detection of a brown dwarf of $30\,\mathrm{M}_J$, 5 Gyr old, orbiting around a solar-type star, is shown in Fig.5.4. As mentioned above, the mechanism for reduction of speckle noise presented here is useful only if the monochromatic images obtained from the spectra are scaled in an appropriate way: no rescaling (at left) usually makes the companion not detectable, while with a good rescaling procedure (at right) the companion is clearly visible with quite a high signal-to-noise ratio ($\sim$30).

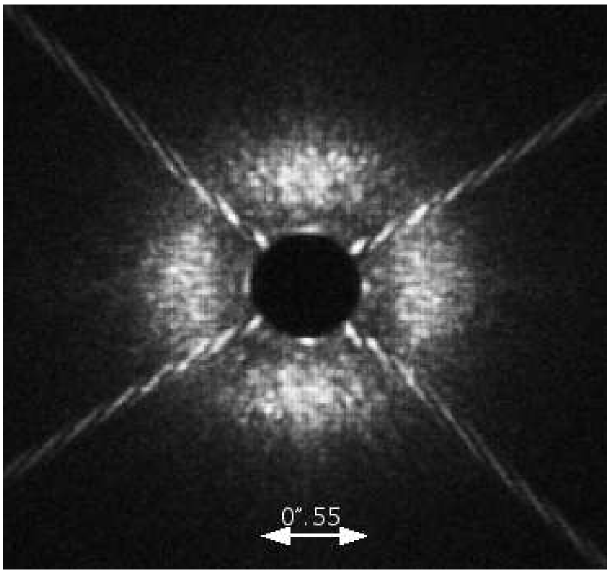

Figure 5.3: A rebuilt monochromatic image obtained by the procedure of data reduction of the simulation code. As explained in the text, from the spectra we obtain a set of images like this that, after a scaling procedure in size, can be compared each other in order to enhance the planetary signal.

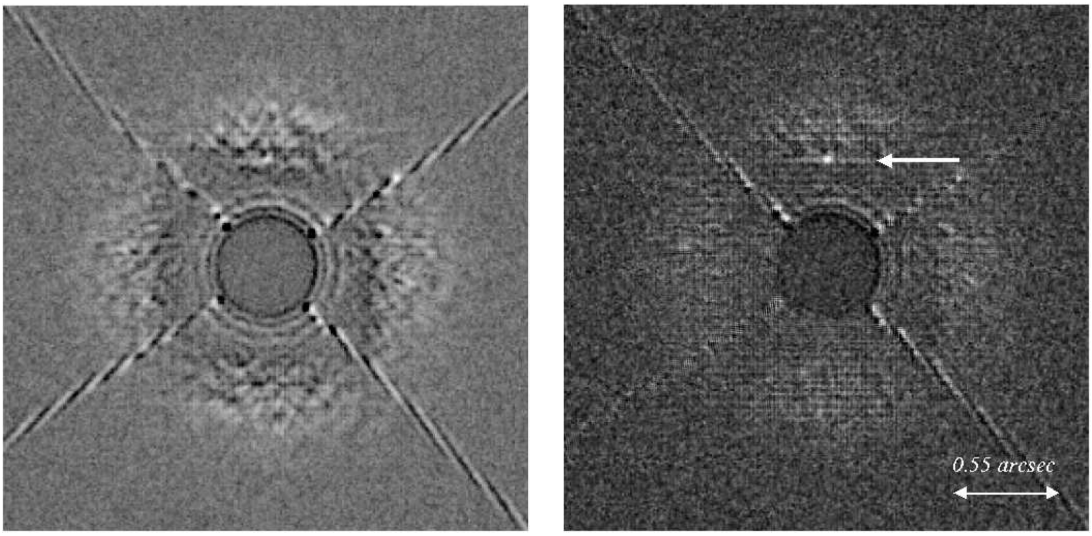

Figure 5.4: Detection of a simulated brown dwarf of 30 M_J after 1 hour of exposure time, around a 5 Gyr old G0V star at 40 pc. Left: three images obtained at different wavelength, on and off a methane absorption band, are combined using Eq.3.16 but without an accurate spatial scaling: the brown dwarf is visible, but at a signal-to-noise ratio low enough to confuse it with a false alarm. Right: the results of the same operation, but now rescaling appropriately the images by a factor λ_0/λ (see Sec.5.4). An appropriate scale factor has been applied also to the fluxes. The result is a clear unambiguous detection of the companion, not possible without application of the rescaling procedure, with a signal-to-noise ratio of $\sim$30.

Chapter 6

Simulations of observations at VLT

6.1 Introduction to the VLT simulations

The simulation code, as it has been described in the previous chapter, has been used for the CHEOPS phase A simulations. At that time, the optical design chosen was the TIGER one, neglecting the problems of speckle chromatism and undersampling (see Sec.4.3.2). This means that the results obtained from these simulations have to be considered a simplification to a perfect case, with very good interpolation of spectra and perfect sampling. After this clarification, the results appear still interesting, but need to be compared to other results taken without these assumptions.

In this chapter we show in detail what has been done and which results have been achieved with CHEOPS simulations. After this description, in Sec.6.3 we present on one side the consequences of non-uniform illumination of lenses, speckle chromatism and undersampling to the simulated results, and on the other side the modifications made during the SPHERE phase B to simulate the HYPERTIGER design.

6.2 Results for CHEOPS phase A

We simulated an observation of various Jupiter-like planets and low-mass brown dwarfs with an 8m-class telescope. For each case we calculated a signal-to-noise ratio, in order to define which kinds of planets are detectable with a signal-to-noise ratio larger than 5, the threshold of detectability. We simulated the following specific cases:

- 4 different planetary masses: 1, 5, 15, 30 M_J.
- 3 values of ages: 0.01, 1, 5 Gyr.
- 3 distances from the Sun: 3, 10, 40 pc.
- 2 types of stars: a G0V and a M0V.
- 3 different seeing conditions: 0.60 (good), 0.85 (median), 1.00 (not so good) arcseconds.
- Various angular separations between the host star and the companion, over a range between ∼0.3 and ∼4 arcseconds.

The exposure time was always assumed to be 4 hours.

In this list of cases we found objects warm enough to be characterized only by intrinsic thermal emission, and at the same time old and small planets that shine only due to reflected light. Moreover, usually the planetary spectra are different as a function of the physical separation between planet and star. Thus, the sample we covered is appropriate for a wide group of targets within the capabilities of an 8-meter telescope. We needed a large set of spectral models, that were taken from Burrows et al. (2004).

The main results of the simulations are presented in this section. As secondary results, we also discuss the frequency of false alarms (Sec.6.2.3), and the general capabilities of this technique in removing speckle noise (Sec.6.2.4).

In Tab.6.1 we compiled the signal-to-noise ratios for all the cases listed above, for good seeing conditions (seeing of 0″.6). The values are expressed as a function of the angular separation from the host star. It is important to note that we tried to be conservative in choosing the various parameters, in order to present a lower limit of the expected signal-to-noise ratios.

For some significant cases we also show plots (Fig.6.1, left) with the level of noise before and after the subtraction of speckles, the photon noise and the expected signal from the planet. Plots of the measured signal-to-noise ratios versus separations are also shown (Fig.6.1, right).

Because of the expensive calculations to simulate observations of 4 hours with our code, some of these results have been obtained using scaling laws and a faster

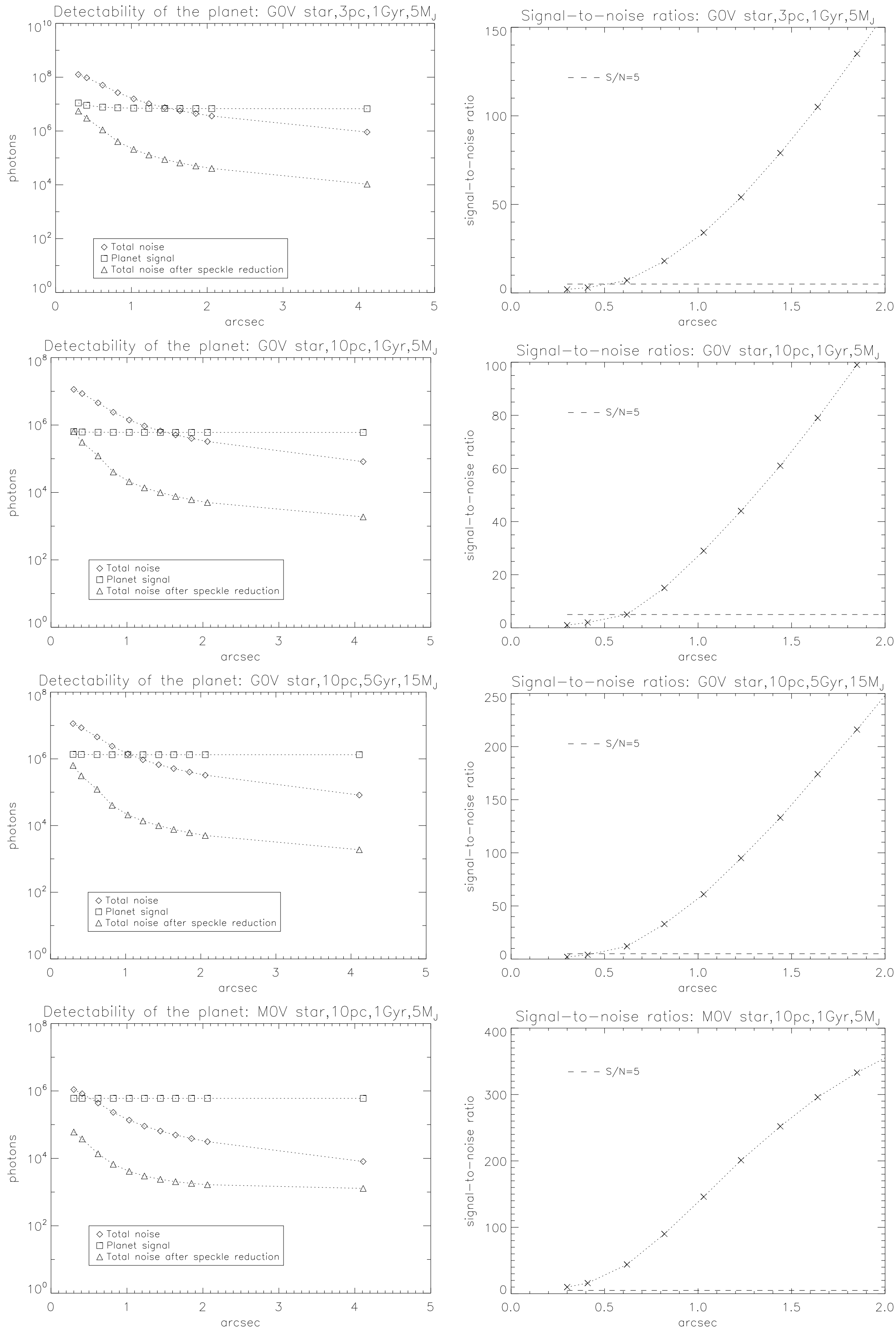

Detectability of the planet: G0V star,3pc,1Gyr,5M$_J$

Signal−to−noise ratios: G0V star,3pc,1Gyr,5M$_J$

Detectability of the planet: G0V star,10pc,1Gyr,5M$_J$

Signal−to−noise ratios: G0V star,10pc,1Gyr,5M$_J$

Detectability of the planet: G0V star,10pc,5Gyr,15M$_J$

Signal−to−noise ratios: G0V star,10pc,5Gyr,15M$_J$

Detectability of the planet: M0V star,10pc,1Gyr,5M$_J$

Signal−to−noise ratios: M0V star,10pc,1Gyr,5M$_J$

Figure 6.1: Left: The levels of signal and noise are shown, before and after SDI, for four cases. Right: The derived signal-to-noise ratios. The cases are, from top to bottom: G0V star, 3 pc, 1 Gyr, 5 M$_J$; G0V star, 10 pc, 1 Gyr, 5 M$_J$; G0V star, 10 pc, 5 Gyr, 15 M$_J$; M0V star, 10 pc, 1 Gyr, 5 M$_J$.

spreadsheet which computes the signal-to-noise of a planet image at different separations from the star as expected at the output of a simultaneous differential imager like the one we simulated. This spreadsheet, called CSS (CHEOPS Simulation Spreadsheet) is based both on theoretical estimates and on the simulated PSFs and noises. Many cases presented in Tab.6.1 have been obtained using both the simulation code and the spreadsheet: the good coincidence of the results allowed us to use it for the detections not easy to simulate (for instance, the objects at angular separation of 4″.21 which cannot be simulated because it is out of our field of view). A description of the CSS spreadsheet is presented in Appendix A.

Table 6.1: Signal-to-noise ratios of the simulated planets and Brown Dwarfs for seeing 0″.6 (Strehl ratio 0.8). The symbol > indicates a ratio larger than 10^3, and it means a sure detection. ST is the stellar type; the distance is in parsecs, the age in Gyr and the mass in M_J.

Angular separations (arcseconds):				0.3	0.41	0.62	0.82	1.03	1.23	1.44	1.64	1.85	2.06	4.21
ST	Dist.	Age	Mass											
G0V	3	0.01	1	29	52	163	427	845	>	>	>	>	>	>
G0V	3	0.01	5	>	>	>	>	>	>	>	>	>	>	>
G0V	3	0.01	15	>	>	>	>	>	>	>	>	>	>	>
G0V	3	0.01	30	>	>	>	>	>	>	>	>	>	>	>
G0V	3	1	1	1	1	1	1	2	2	2	2	2	2	2
G0V	3	1	5	2	3	7	18	34	54	79	105	135	167	634
G0V	3	1	15	42	79	268	802	>	>	>	>	>	>	>
G0V	3	1	30	442	812	>	>	>	>	>	>	>	>	>
G0V	3	5	5	1	1	1	1	2	2	2	2	2	2	3
G0V	3	5	15	3	5	14	37	72	117	170	228	292	364	>
G0V	3	5	30	23	42	133	351	695	>	>	>	>	>	>
G0V	10	0.01	1	27	50	155	388	726	>	>	>	>	>	>
G0V	10	0.01	5	>	>	>	>	>	>	>	>	>	>	>
G0V	10	0.01	15	>	>	>	>	>	>	>	>	>	>	>
G0V	10	0.01	30	>	>	>	>	>	>	>	>	>	>	>
G0V	10	1	1	0	0	0	0	0	0	0	0	0	0	0
G0V	10	1	5	1	2	5	15	29	44	61	79	99	120	320
G0V	10	1	15	41	78	253	692	>	>	>	>	>	>	>
G0V	10	1	30	430	771	>	>	>	>	>	>	>	>	>
G0V	10	5	5	0	0	0	0	0	0	0	0	0	0	0
G0V	10	5	15	2	4	12	33	61	95	133	174	216	261	650
G0V	10	5	30	23	41	126	318	598	915	>	>	>	>	>
G0V	40	0.01	1	24	41	101	196	305	403	486	548	596	631	733
G0V	40	0.01	5	>	>	>	>	>	>	>	>	>	>	>
G0V	40	0.01	15	>	>	>	>	>	>	>	>	>	>	>
G0V	40	0.01	30	>	>	>	>	>	>	>	>	>	>	>
G0V	40	1	1	0	0	0	0	0	0	0	0	0	0	0
G0V	40	1	5	1	1	4	7	12	16	20	23	26	29	35
G0V	40	1	15	35	60	147	286	439	574	681	762	820	864	981
G0V	40	1	30	388	650	>	>	>	>	>	>	>	>	>
G0V	40	5	5	0	0	0	0	0	0	0	0	0	0	0
G0V	40	5	15	2	3	8	16	26	35	44	50	57	61	78
G0V	40	5	30	20	34	82	160	250	333	404	458	500	532	626
M0V	3	0.01	1	286	525	>	>	>	>	>	>	>	>	>
M0V	3	0.01	5	>	>	>	>	>	>	>	>	>	>	>
M0V	3	0.01	15	>	>	>	>	>	>	>	>	>	>	>
M0V	3	0.01	30	>	>	>	>	>	>	>	>	>	>	>
M0V	3	1	1	1	1	1	1	1	2	2	2	2	2	1
M0V	3	1	5	11	20	60	152	288	446	619	793	970	>	>
M0V	3	1	15	416	759	>	>	>	>	>	>	>	>	>
M0V	3	1	30	>	>	>	>	>	>	>	>	>	>	>
M0V	3	5	5	1	1	1	1	2	2	2	2	2	2	3
M0V	3	5	15	24	45	147	409	821	>	>	>	>	>	>
M0V	3	5	30	234	432	>	>	>	>	>	>	>	>	>
M0V	10	0.01	1	262	456	>	>	>	>	>	>	>	>	>
M0V	10	0.01	5	>	>	>	>	>	>	>	>	>	>	>

M0V	10	0.01	15	>	>	>	>	>	>	>	>	>	>	>
M0V	10	0.01	30	>	>	>	>	>	>	>	>	>	>	>
M0V	10	1	1	0	0	0	0	0	0	0	0	0	0	0
M0V	10	1	5	10	16	44	90	146	201	252	296	333	364	469
M0V	10	1	15	377	643	>	>	>	>	>	>	>	>	>
M0V	10	1	30	>	>	>	>	>	>	>	>	>	>	>
M0V	10	5	5	0	0	0	0	0	0	0	0	0	0	0
M0V	10	5	15	22	38	101	208	333	447	547	626	687	736	884
M0V	10	5	30	212	364	903	>	>	>	>	>	>	>	>
M0V	40	0.01	1	139	199	355	524	628	681	707	722	730	736	748
M0V	40	0.01	5	>	>	>	>	>	>	>	>	>	>	>
M0V	40	0.01	15	>	>	>	>	>	>	>	>	>	>	>
M0V	40	0.01	30	>	>	>	>	>	>	>	>	>	>	>
M0V	40	1	1	0	0	0	0	0	0	0	0	0	0	0
M0V	40	1	5	5	7	14	22	29	31	34	34	35	35	37
M0V	40	1	15	203	288	507	729	860	921	952	968	978	985	997
M0V	40	1	30	>	>	>	>	>	>	>	>	>	>	>
M0V	40	5	5	0	0	0	0	0	0	0	0	0	0	0
M0V	40	5	15	11	16	30	48	61	68	73	75	76	78	80
M0V	40	5	30	113	162	292	435	529	577	601	615	623	628	639

Flux contrasts for the cases considered

In Tab.6.2 and in Fig.6.2 and 6.3 we report an analysis of the flux contrasts between the intensity peaks of the planets and stars considered for the simulations, calculated in J band. In the four plots of Fig.6.2 these contrasts have been represented as a function of the angular separation, always expressed in arcseconds. The contrast are also plotted with respect to the mass of the planet and to the age of the system. The contrast are calculated for a distance of 3 pc from the Sun; moreover, in both Fig.6.2 and Fig.6.3, at bottom right, the contrasts for a 1 M_J and 1 Gyr old planet at different distances are presented. The magnitudes of the planets in J band are taken from Baraffe et al. (2003), and the fluxes at various separations are computed used the CSS spreadsheet described in Appendix A.

From the plots we can see the different behavior of the contrast of reflecting planets, if compared to thermally emitting planets: the formers present a decrement in flux at large separation, due to the dependence of the flux on the distance a^{-2} (Eq.3.1); the latters present the same decrement but only very close to the host star, while at larger separations the reflection of stellar light becomes negligible with respect to the intrinsic emission, and the contrast becomes a constant.

Even if in the plots the main results are presented for a distance of 3 pc, the values of contrast obtained for warm thermally emitting planets are expected to remain the same also at different distances (except for a small region close to the star). For less massive or older planets this is not true, because the flux depends

St. Type	Mass: Age	$1M_J$	$5M_J$	$15M_J$	$30\ M_J$
G0V	0.01Gyr	$1.60{\cdot}10^{-6}$	$1.08{\cdot}10^{-4}$	$6.16{\cdot}10^{-4}$	$9.33{\cdot}10^{-3}$
G0V	1Gyr	$3.71{\cdot}10^{-8}$	$9.41{\cdot}10^{-8}$	$2.34{\cdot}10^{-6}$	$2.52{\cdot}10^{-5}$
G0V	5Gyr	-	$3.71{\cdot}10^{-8}$	$1.63{\cdot}10^{-7}$	$1.31{\cdot}10^{-6}$
M0V	0.01Gyr	$1.62{\cdot}10^{-5}$	$1.12{\cdot}10^{-3}$	$6.39{\cdot}10^{-3}$	$9.68{\cdot}10^{-2}$
M0V	1Gyr	$3.71{\cdot}10^{-8}$	$6.40{\cdot}10^{-7}$	$2.39{\cdot}10^{-5}$	$2.62{\cdot}10^{-4}$
M0V	5Gyr	-	$3.77{\cdot}10^{-8}$	$1.35{\cdot}10^{-6}$	$1.32{\cdot}10^{-5}$

Table 6.2: Flux contrasts between the intensity peaks of the planets and stars considered in Tab.6.1, for a fixed separation of 1 AU between the two objects. For planets characterized by intrinsic thermal emission we don't expect a significant decrement of their fluxes for larger separations; so the contrasts calculated for 1 AU can be assumed to be valid also further away from the star. This is not true for planets shining by reflected light, whose brightness strongly depends on the physical separation (see e.g. the 1 M_J planet in Fig.6.2 at top-left).

on the physical separation between star and planet, and at a larger distance this separation appears under a smaller angular separation. For this reason, the plots for different distances have been drawn only for planet shining by reflecting light (1 M_J, 1 Gyr old).

Tab.6.2 summarizes these contrasts for all the studied cases, for planets at 1 AU from their host star. Since the physical separation is fixed, these results are valid at every distance from the Sun.

6.2.1 Notes on the flat field errors and the thermal background

Flat field errors were included as multiplicative terms to the total number of photons detected by each pixel of the detector. Accurate flat fielding is foreseen and images will be obtained using a dithering procedure that spread the signal of the planet over a large number of pixels by allowing the field to rotate from one exposure to the following one (typically, a few thousands of exposures are summed up to provide the total exposure). Therefore it is reasonable to assume that the residual flat field error in a detector pixel can vary between 10^{-3} that can be achieved using an accurate dithering procedure, and the goal of 10^{-4} . This value is assumed in our computations, although it is certainly not easy to achieve. Flat field errors are important for bright sources and for the regions closer to the stars, limiting sometimes the possibility of observing planets by reflected light when using the

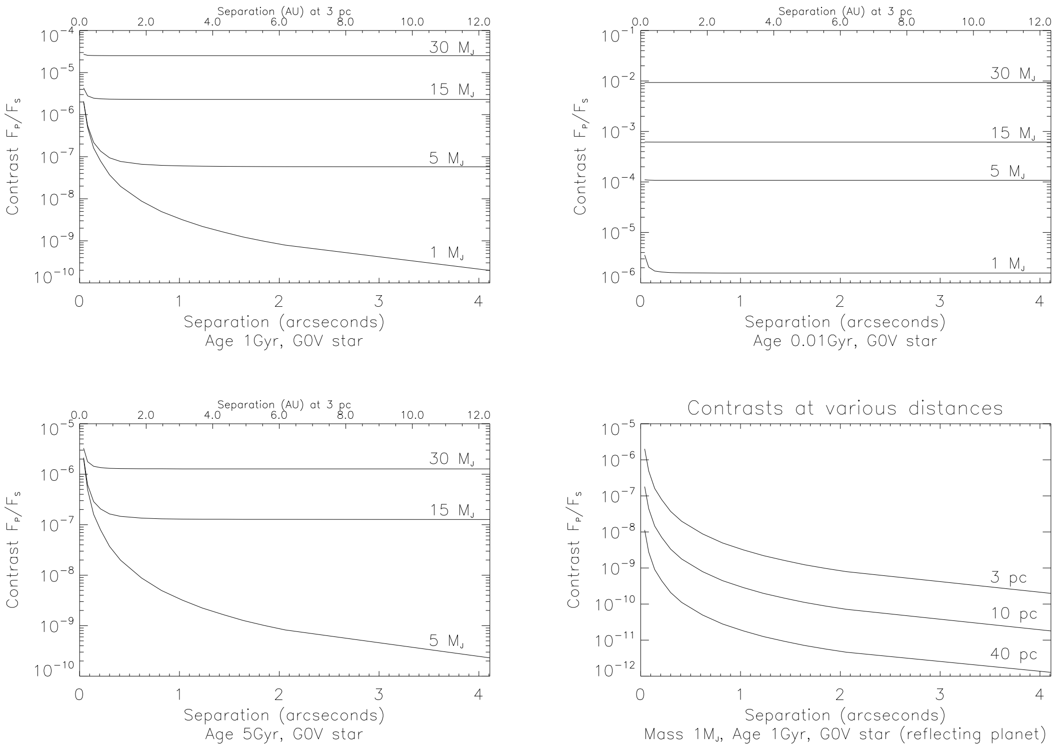

Figure 6.2: Contrasts between the flux of the central peak of a planet (F_P) and the flux of the central peak of the host star (F_S) as function of the angular separation, calculated in J band for the planets simulated. The star is always a G0V star and the distance 3 pc, the ages of the system are 1 Gyr (top-left), 10 Myr (top-right) and 5 Gyr (bottom-left). In each plot the results are computed for four different masses (1, 5, 15, 30 M_J). The physical separation in AU is also reported. At bottom-right: the contrasts as function of the angular separations for a 1 M_J, 1 Gyr old planet in a system at 3, 10 and 40 pc from the Sun. Data taken from Baraffe et al. (2003).

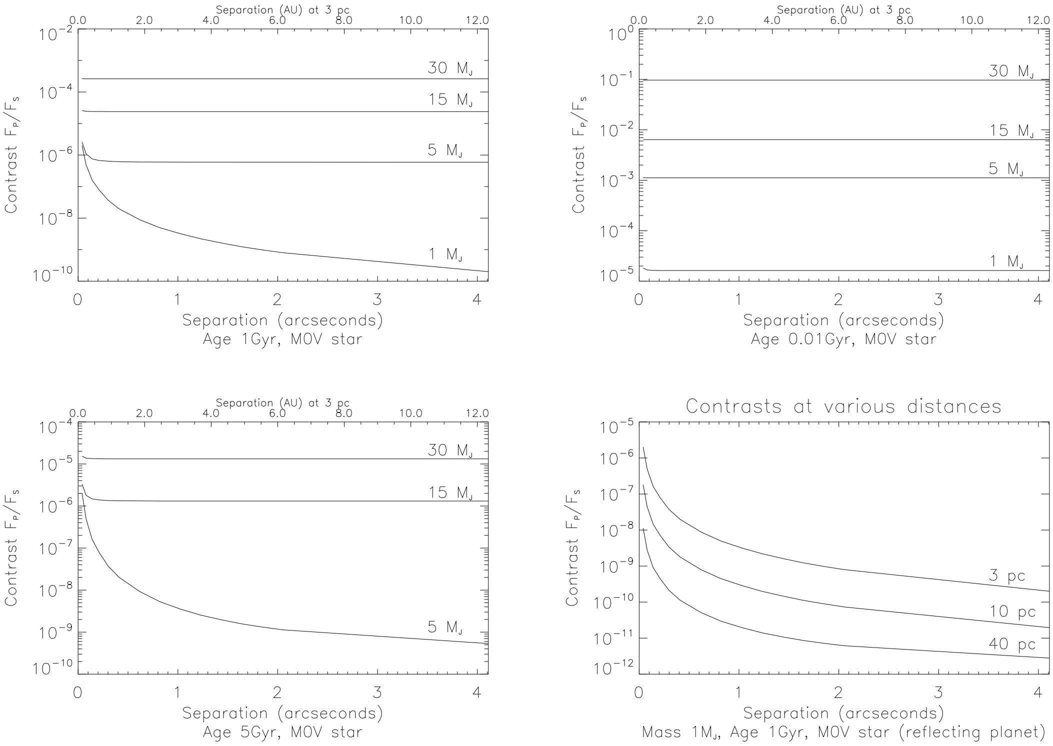

Figure 6.3: Contrasts between the flux of the central peak of a planet (F_P) and the flux of the central peak of the host star (F_S) as function of the angular separation, calculated in J band for the planets simulated. These plots are equivalent to the one in Fig.6.2, but the star is a M0V star. Data taken from Baraffe et al. (2003). See text for details.

SDI-IFS. Fig.6.4 shows this comparison in terms of measured signal-to-noise ratios for a 15 M_J object orbiting a G0V star at 1 Gyr age at 10 pc from the Sun: the detections within 0.3 and 0.6 arcseconds, which was possible without considering flat field errors, are shifted below the threshold of S/N=5 in case of error $\sim 10^{-4}$.

Concerning the thermal background, which is also a source of errors, we assume that cold edge filters are placed in front of the IFS detectors. These edge filters will reduce the thermal background flux by a factor between 10^{-4} down to 10^{-5}. We adopted this last value in our computations. The thermal background flux is not a serious concern in the $J-$band but it may be of some importance for the faintest sources in the $H-$band.

6.2.2 Different seeing conditions

To show the effect of median (0″.85) or relatively bad (1″.00) seeing conditions in comparison with the good case described above, we repeated the simulations for a

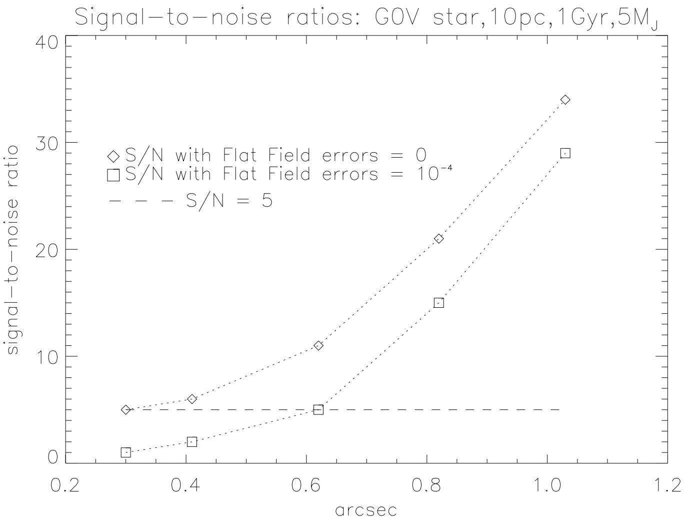

Figure 6.4: Importance of flat field errors in detecting companions. In the case of a 15 M_J object, around a G0V star (age 1 Gyr and at 10 pc from the Sun), the signal-to-noise ratios decrease below 5 (dashed line) in the region closest to the star.

few specific planets, selected in order to avoid too bright or too faint planets. From these simulations it becomes obvious how important it is to work with the best atmospheric conditions when using our method to detect planets.

We show here the results for four significant cases:

- A 5 M_J planet, 1 Gyr old, around a G0V star at 3 pc.
- A 5 M_J one, 1 Gyr old, around a G0V star at 10 pc.
- A 5 M_J one, 1 Gyr old, around a M0V star at 10 pc.
- A 1 M_J one, 0.01 Gyr old, around a M0V star at 40 pc.

The resulting signal-to-noise ratios are presented graphically in Fig.6.5. The plots show that the quality of detection decreases as the FWHM increases. This is due to the fact that the Strehl Ratio (S) achievable by the AO system is different in the three observing conditions. While the achievable signal-to-noise ratio does not change too much when going from optimal (seeing 0″.60, Strehl ratio of 0.80) to good (seeing 0″.85, Strehl ratio of 0.75) conditions, planet detection is clearly much more difficult in the not-so-good condition (seeing 1″.00, Strehl ratio of 0.40)[1].

---

[1] As explained in Sec.5.3.1, our AO simulator is not detailed enough to claim a true significance of the dependence of signal-to-noise ratio on seeing. Rather, the Strehl numbers themselves should be seen as independent parameters.

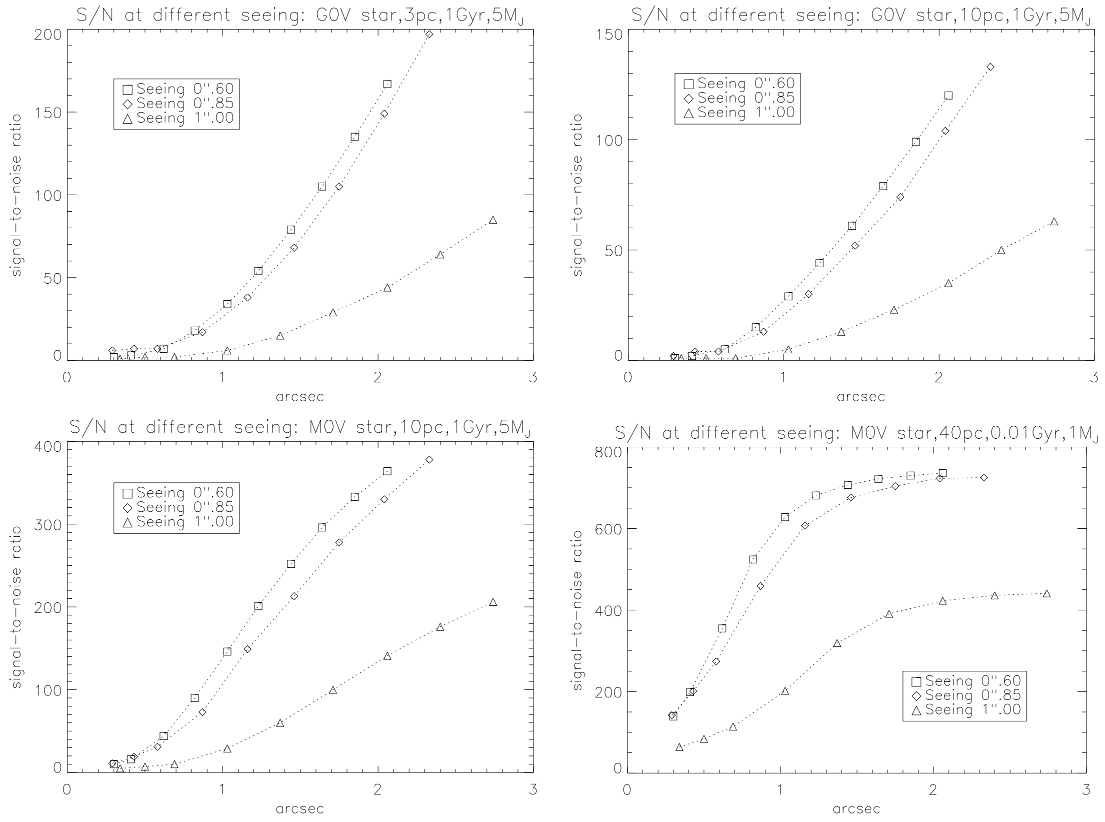

Figure 6.5: Signal-to-noise ratios for detection of four planets at three different seeing conditions and at different angular separations. The four cases are described in Sec.6.2.2. Every value of seeing have to be associated to a Strehl Ratio S as explained in the text: S=0.80 for the best seeing (0″.60), S=0.75 for the median (0″.80) and S=0.40 for the worst case (1″.00). While the ratios are quite similar between S=0.80 and S=0.75, they decrease dramatically in case of a seeing of 1″.00, because of the Strehl ratio achievable by the optical system, which is only 0.40.

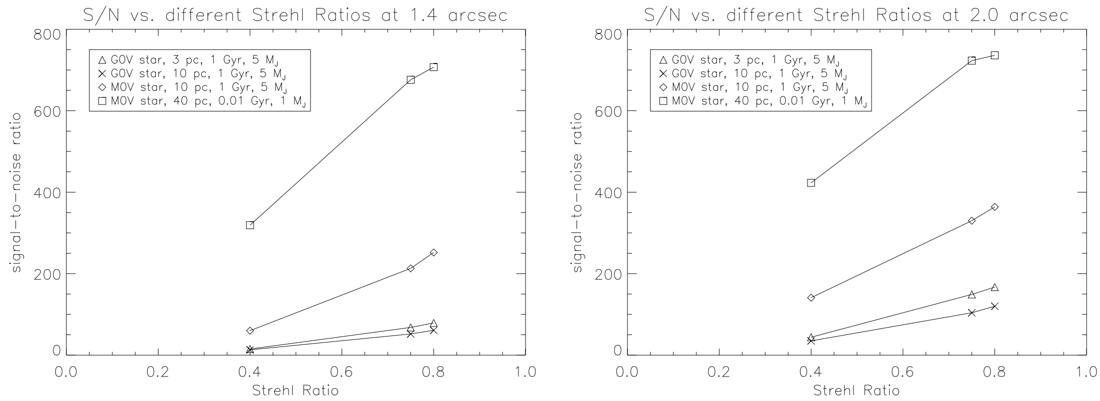

Figure 6.6: Signal-to-noise ratios as a function of the achieved Strehl ratio under the three seeing conditions, measured at 2 angular separations: 1″.4 and 2″.0. The four planets studied are described in Sec.6.2.2. The Strehl Ratios are strongly dependent on the seeing and on the capabilities of the AO system.

Signal-to-noise	Probability	Number of events
1	0.3504	1347
2	0.0921	354
3	0.0099	38
4	$4.405 \cdot 10^{-4}$	1.7
5	$8.007 \cdot 10^{-6}$	0.031
6	$5.974 \cdot 10^{-8}$	$2.30 \cdot 10^{-4}$
7	$1.829 \cdot 10^{-10}$	$7.03 \cdot 10^{-7}$

Table 6.3: Probability of detection of false alarms, and expected number per final differential image.

In Fig.6.6 the signal-to-noise ratio is presented as a function of Strehl ratio for two angular separations. The signal to noise ratios, going from S=0.80 to S=0.75 and S=0.40, are reduced by a factor of $\sim$2. Since the value of S depends not only on the atmospheric turbulence and seeing but also on the performances of the AO systems, these plots show in a more general way how important is to work both with a good seeing and with a very efficient AO to detect extrasolar planets.

6.2.3 Estimation of false alarm frequency

We estimated the probability of detecting a false signal with a signal-to-noise ratio between 1 and 7, with a sampling aperture corresponding to $\sim 2 \times 2$ spatial resolution elements[2]. Using this probability, we could extrapolate the expected number of events in the final differential image. The results are presented in Tab.6.3. These probabilities clearly demonstrate that the threshold signal-to-noise of 5 is high enough to avoid false alarms. Therefore, we choose this value in an evaluation of detecting planets with the IFS. Moreover, a more confident confirmation of detections can be done repeating the observations under the same conditions if possible, and at different angles. Comparing the position of the detected candidates, we can easily confirm or not if it is a false alarm.

In the case of a large number of observations the number of false alarms can become more important. With a S/N of 5, we expected one false alarm within 30 observations. This means that a "detection" always has to be checked by additional observations.

---

[2] We suppose a Gaussian distribution of noise.

6.2.4 Factor of reduction of Speckle Noise

A crucial result of these simulations is the determination of a value characterizing the effective reduction of speckle noise achieved using the IFS-SDI technique. We know from theory the behavior of speckle noise as a function of time, flux and Strehl ratio (Eq.3.13). Applying SDI to the obtained data reduces the noise by a certain factor which we call ϵ. The expression for the reduced speckle noise N would be this:

$$N = N_{sp}\epsilon = \sqrt{1.7\pi\frac{\tau_0}{t}} \left[\left(\frac{\lambda}{D}\right)^2 (1-S)\, F_* f_{halo}(\vartheta) \right] \epsilon(\vartheta), \tag{6.1}$$

where N_{sp} is the original level of speckle noise and the other variables are as explained in Sec.3.2.1. In order to calculate ϵ, we considered first one of the monochromatic images, before the SDI procedure, scaled to the wavelength λ_0 of the original image. In this image we analyzed the level of noise N_{sp} in a set of small regions placed in a radial sector, at different angular separation from the central peak. This radial sector has been chosen to avoid spiders, artifacts and also the simulated planets. We repeated the procedure using the image resulting from the SDI, obtaining a resulting noise N_d. While in N_{sp} the speckle noise is strongly dominating, in N_d the contributions of photon noise N_{ph} and of other background noise sources (B, that are detector noise, background sky, etc.) become important. These contributions can be easily derived from the average intensity in the regions analyzed before subtracting for N_{ph}, and by measuring the level of noise in a peripheral region not affected by speckles.

The formula we used to calculate ϵ is finally, for each portion:

$$\epsilon(\vartheta) = \sqrt{\frac{N_d^2(\vartheta) - N_{ph}^2(\vartheta) - B^2}{N_{sp}^2(\vartheta)}}. \tag{6.2}$$

The quantity ϑ indicates the distance between the center and the different region of the image. Since the regions are chosen on a radial sector at different separations from the center, ϑ is expressed in arcseconds. We repeated the procedure for different sizes of the regions and for different radial sectors. The results obtained are sometimes quite different because the simulated PSF is not perfectly symmetric. They were averaged in a final $\epsilon(\vartheta)$.

From Fig.6.7 we can easily see that the final noise using this technique becomes comparable with the photon noise for the three cases considered (M0V star at 10 pc,

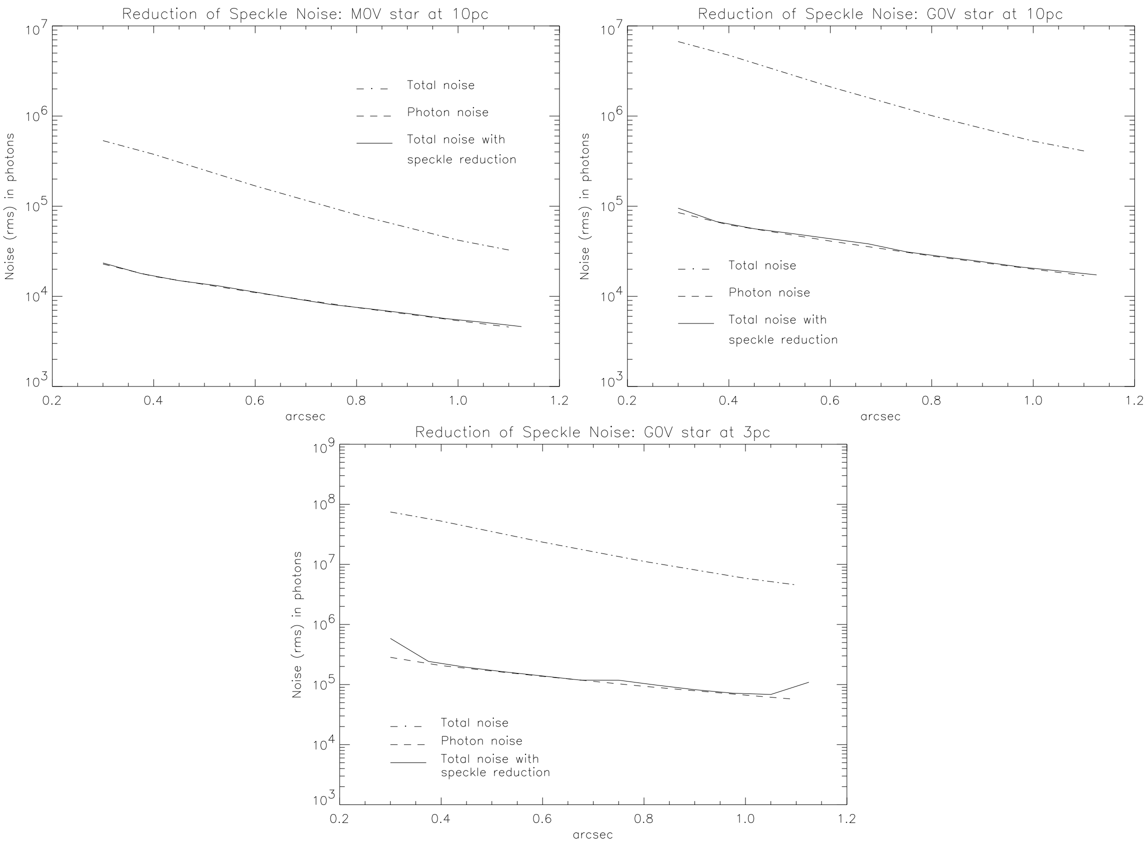

Figure 6.7: Reduction of the speckle noise as a function of the angular separation from the star: Dash dotted line represents the total level of noise before SDI, dominated by speckle noise. The dashed line is the photon noise. The solid line is the total noise after application of SDI. Top left: the case of an M0V star at 10 pc from the Sun. Top right: a G0V star at 10 pc. Bottom: a G0V star at 3 pc. In all cases we obtained reductions of a factor around 10^{-3}, and the final level of noise is very close to the photon noise.

G0V star at 10 pc, G0V star at 3 pc). The factor of reduction changes with the separation, but it is $\sim 10^{-3}$ between $0''.3$ and $1''.0$. This value for ϵ is an indicator of a good suppression of speckle noise.

This result shows that using the SDI technique is actually possible to reach a level of noise comparable with the photon noise. Similar conclusions, in terms of dual band imaging SDI, have been achieved for NACO-SDI in Biller et al. (2006).

6.2.5 Combination of multiple images

We present in this section a test made on the simulated images in order to verify the reasons for which IFS-SDI is preferable to the filter-based differential imaging technique; in particular we want to demonstrate that the analysis of a number of wavelengths larger than 2 or 3 gives us a gain in signal-to-noise ratio and noise reduction. To do this, we applied four different operations to the monochromatic images obtained from the spectra, accurately rescaled to a given wavelength. The four operations combine 2, 3, 6 and 9 different resolution elements. The images are indicated by I_n.

1. Single difference, with 2 elements: $I_2 - I_1$.
2. Double difference, with 3 elements, which is Eq.3.16.
3. 3^{rd} difference, with 6 elements, is given by

$$\begin{aligned} DDD = & \left[(I_1 - I_2) - k_1 (I_1 - I_3)\right] + \\ & -K \left[(I_4 - I_5) - k_2 (I_4 - I_6)\right]. \end{aligned} \tag{6.3}$$

4. The 4^{th} difference is a combination of two 3^{rd} differences:

$$\begin{aligned} DDDD = & \; DDD_1 - \kappa DDD_2 = \\ & \left[(I_1 - I_2) - k_1 (I_1 - I_3)\right] + \\ & - K_1 \left[(I_4 - I_5) - k_2 (I_4 - I_6)\right] + \\ & - \kappa \left[(I_4 - I_5) - k_3 (I_4 - I_6)\right] + \\ & + \kappa K_2 \left[(I_7 - I_8) - k_4 (I_7 - I_9)\right]. \end{aligned} \tag{6.4}$$

The values k_n, K_n and κ are constants that have to be defined case by case in order to subtract the speckles and their residuals as best as possible. Every subtraction, other than reducing speckle noise, introduces a slight increment of the other sources of noise (photons, sky background, detector noises etc.) that has to be considered carefully.

At first, we measured the total level of noise in a specific region of the stellar PSF normally dominated by speckles (in our case, for an 8m-class telescope, we worked between 0.4 and 0.6 arcseconds, avoiding spiders and artifacts). We used different simulations of the same object, and we obtained averaged values of residual noise in this region using all the four different algorithms. All these calculations of noise have been done without planets. We calculated then the signal of a planet, chosen bright enough to be detectable clearly (signal-to-noise ratio $\sim$5) with the single difference method, and with all but one of the resolution elements considered in absorption bands: practically, the signal of the planet is significant only in one of the nine cases. In this way, we simulated a detection using nine different wavelengths but only one of the three "peaks" of the planetary spectrum shown in Fig.1.2. We calculated the signal-to-noise ratios of the detection, as a function of the operation used for subtracting speckle noise.

In a second step, we tried to elaborate the results a little more in order to also use the other "peaks" of the spectrum of the planet. Practically, considering that the signal of the planet in SDI is given by the contrast in flux of the planet on and off an absorption band, we combined the contrasts in two of the three peaks to increase the signal-to-noise ratio. We used the spectrum of a $1\,M_J$ planet at 1AU from a solar-type star (Fig.1.2 at right), where we have two peaks of very similar maximum intensity. The results are shown in Fig.6.8.

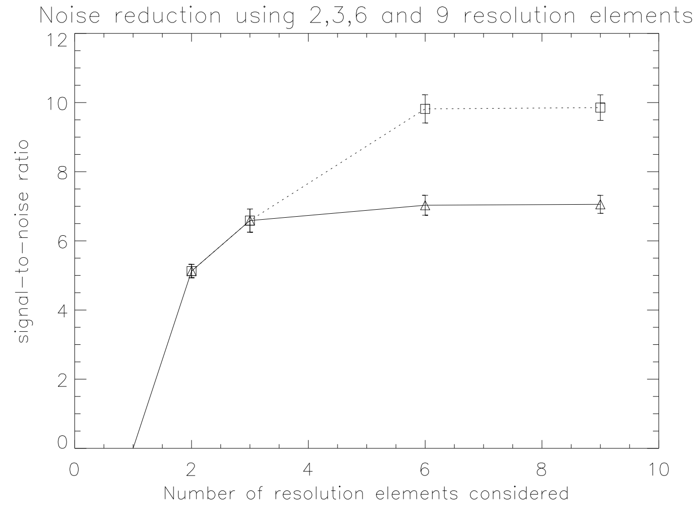

Figure 6.8: Improvement of signal-to-noise ratio of a detection using combinations of different numbers of resolution elements. The triangles connected by the solid line are the results obtained considering a single planetary spectral features; the squares, connected by a dotted line, are obtained considering simultaneously two similar features, which is possible only with IFS-SDI and only considering more than 3 resolution elements. More details are explained in the text. The noise level for this plot has been calculated in various regions of the images and using various simulations of the same object, so the result shown are averaged signal-to-noise ratios with error bars given by the standard deviations. Although the improvement in detection is not very dramatic using only one spectral feature and a number of resolution elements larger than 3, the possibility of using two spectral features instead of one can be really significant, as shown by the dotted line in the plot.

It appears obvious from this plot that a number of resolution elements larger than 3 can actually improve the signal-to-noise ratio of the detection. In fact the improvement is significant, but not dramatic, because just after the double difference the total noise is less dominated by speckles and more by photons. The photon noise represents a limit that cannot be over passed just combining more elements.

Moreover, with 9 resolution elements the signal-to-noise ratio does not increase. To conclude, a combination of six elements seems to be the best solution for reducing speckle noise, keeping all the other sources of noise under control.

On the other hand, the simultaneous use of other planetary features, represented by the three "peaks" of Fig.1.2 at right, provides an interesting improvement of the signal of the planet, and consequently of the signal-to-noise ratio. Actually, we used only the two highest peaks at $\sim$1.25 and $\sim 1.60\mu$m, because the contribution of the third peak (at $\sim 1.05\mu$m) is negligible if compared with the increment of noise combining it with the other data. As shown in Fig.6.8, we actually improved the signal-to-noise ratio by a factor of $\sim\sqrt{2}$, because the contrast for both peaks is very similar. Since a dual band imager can enhance some specific spectral features depending on the used filters, it is not easily achievable to observe at the same time many of these different features, while to have all the peaks in a single simultaneous exposure is possible with IFS.

6.2.6 Conclusion from CHEOPS simulations

From the data shown in Tab.6.1 we can see that most of the targets we simulated to observe are actually detectable. In particular, it is clear that very massive objects (30 M_J) and very young ones (0.01 Gyr) are detected at every considered distance with very high signal-to-noise ratios (usually higher than 1 000). In the other cases, the signal-to-noise ratios are strongly dependent on the age and on the mass of the planet, as shown in Fig.6.9. From these plots we can conclude that the detection is easier in the case of larger masses, or, if the mass is fixed, for young objects.

The less massive objects (from 1 to 5 M_J) are more interesting targets, but they are also much more difficult to detect. Their potential detection is more sensitive to the distance of the planetary system (they are almost unobservable at 40 pc) because of their faintness in the near-infrared region. In some cases they are shining by reflected light, namely the 1 M_J planets older than 1 Gyr, but also the 5 M_J 5 Gyr old. Systems with planets shining by reflected light are the most interesting cases, because of the similarities with the Solar System. Detection of a planet like Jupiter (1 M_J, 5 Gyr old) around a star almost like the Sun, at a separation around 5 AU, means to observe something so similar to our system to allow us to suppose the presence of terrestrial planets in inner orbits, perhaps even in the habitable zone. All reflected light cases simulated are not detectable with 4 hours of exposure time, even if they were only at a distance of 3 pc from the Sun. This kind of object is

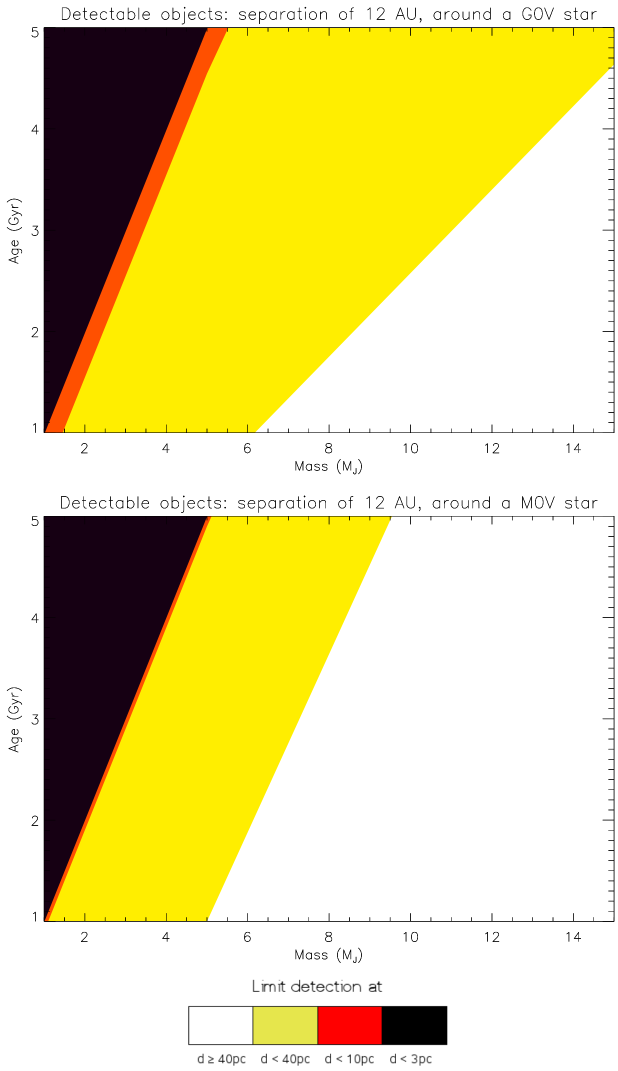

Figure 6.9: Planets detectable with a signal-to-noise ratio higher than 5, as function of mass and age, in the case of a G0V (at top) and a M0V (in the middle) host star. The different colors indicate the combinations of mass and ages that give us a detection ($S/N \geq 5$) at 3, 10 and 40 parsecs. The meaning of the colors is explained in the legend at bottom. The most massive objects ($30\,M_J$) and the youngest planets (0.01 Gyr) are not included in the plot because they can always be detected at the 3 distances considered. The physical separation between the star and the planet has been kept at 12 AU, but this is changing the angular separations, which are respectively 4″.0 at 3 pc, 1″.2 at 10 pc and 0″.3 at 40 pc. These plots have been obtained using data from Tab.6.1.

still a challenging goal for such an instrument, at least if it is mounted on an 8m-class telescope. They can be better detected using different strategies dedicated to reflected light, for example the SPHERE project with the polarization analyzer ZIMPOL.

From the plots in Fig.6.9 we can also conclude that the SDI-IFS technique allows detection of planets of a few Jupiter masses (around 5), with ages of ∼1 Gyr, within a distance of 10 pc. Passing from 10 to 3 pc we are not enlarging dramatically the range of planets detectable, as shown by the very thin dark-gray region in both plots. Planets of a few Jupiter masses, up to now, have been directly detected only if they are very young, while we can consider a 1 Gyr planet to be reasonably old. The direct detection of such an object would be a very important result in the present contest of searching for extrasolar planets.

Finally, comparing the two plots, we note that around an M star it is possible to detect more objects at a distance larger than 10 pc. At 40 pc in this case we can detect some interesting old planets down to $\sim$10 M_J. The reason of these better detections for an M star are simply related to the better contrast due to the lower brightness of the M star with respect to a G star at the same distance. The spectral differences between the two stars at this resolution are less important than the differences in flux. Less flux means less photon noise and less speckle noise. In the case of less flux, beside an improvement of the signal-to-noise ratio, we have also an increment in importance of the photon noise of the planet, that becomes predominant in case of very bright planets and at large angular separation of the star: this can be seen, for example, in Fig.6.5, bottom right, when the signal-to-noise ratio is stabilizing at a given level beyond ∼2 arcseconds.

Although these results showed that many detections are possible, if we compare them with the detection probability described in Sec.4.4 we have to notice that the list of observable targets is not very long, because in the considered ranges of distances (3, 10 and 40 pc) there are only few stars that can harbour planets which are at the same time detectable with our IFS-SDI.

It should not be forgotten that all these results and considerations are related to the case of an 8m-class telescope. It is natural to expect very different results for different instrumental parameters. We suppose that the detection of faint planets, specially those shining by reflecting light, would be significantly easier with a larger telescope, in particular one of the new Extremely Large Telescopes (ELTs) on project, which cover a range of diameters between 20 and 100 m. The structural and technical differences between an ELT and a 8m-class telescope are sometimes not easy and immediate to consider (e.g. segmentations, spiders, AO systems, etc.), so we need new sets of specific simulations to quantify the improvement in signal-to-noise ratios passing from an 8 meter telescope to an ELT. These simulations will be discussed briefly in Chapter 7.

6.2.7 Limitations of the CHEOPS simulations

The CSP code, although it takes into account a large number of parameters and noise sources in order to simulate real observations, can be improved. As said in Sec.4.2 some particulars have been neglected or underestimated for various reasons, sometimes because going too much into details was not the purpose of the work presented here (e.g. the AO system structure), and sometimes because we were interested in immediate performances estimates while a more accurate study would have required excessive computer time.

In particular we want to focus our attention on:

- The problem of non-uniform illumination of lenses described in Sec.4.2, that is not well simulated: at present, this procedure supposes all the lenses to be identical and it associates a standard perfect PSF to each lens, but in reality the phase screen over the entrance pupil of a microlens is not constant.

- Another phenomenon that is currently not well accounted for is the interference between the microlenses. This interference could modify the shape of the PSFs, making them sometimes too faint to obtain a clear spectrum. An accurate simulation of this effect is very expensive in terms of computer resources, and had to be neglected in this first version of the code. However this has been studied in order to determine whether omitting this effect is significant when achieving accurate detections, and from the first results this seems to be a negligible problem.

- To be included in our simulations, and consequently in the procedure of analysis of spectra, is a calibration error due to the fact that in the real observations the central wavelength related to every spectral pixels of each spectrum cannot be perfectly known but requires a calibration; in our code this error is underestimated, and new studies have now shown its importance in the final signal-to-noise ratio of the detections. Since we know perfectly the central wavelength to be associated to any spectral pixel, in this version of the code we do not have any problem at all with speckle chromatism and undersampling: in Sec.6.3 we will show that this semplification has important consequences on the final results.

Concerning the flat field, one should note that the whole process of generating noise is not simulated in detail. We simply calculated a residual noise of 10^{-4}, as explained in Sec.6.2.1. A complete analysis of the flat field process could be important for understanding their effect on the final signal-to-noise ratio achievable.

Finally, during or between the real observations we will need to apply some rotations to the field of view. The level of noise introduced by these rotations and the following corrections should be similar to the one due to the other interpolations, in particular resizing. Moreover, anisoplanatism can also introduce some reductions to the Strehl Ratio of the planet that should be not very significant but have to be studied in detail.

6.3 The HYPERTIGER simulations for SPHERE

The items described in the previous Section appeared in a first moment to be negligible semplifications, but a set of tests were anyway required to validate this impression, and to really understand the feasibility of a TIGER design for SPHERE-IFS. As anticipated in Sec.4.2, the two points that more need a deep analysis (impact of non uniform illumination of the lenses, speckle chromatism and undersampling) are not taken into account on the code. Therefore the simulation code for TIGER had to be modified.

6.3.1 Detailed simulation of TIGER: the non-uniform illumination of lenses

To test how significant this effect can be we used a modified version of the simulation code that exactly computed the diffraction pattern at a selected wavelength (1.25 μm) as given by each lens, for a 32×32 lenslet array (a total of 1024 lenses). In illuminating the array we took into account a variable speckle pattern appropriate for observing conditions at VLT, for 2 integration times: 0.5 ms, shorter than the expected life time of a speckle pattern (supposed to be ~3 ms), and 1 s; conclusions have been obtained also for a time of 4 h. The micropupil plane was sampled with pixels of 18 μm, as expected for SPHERE-IFS detector.

We considered the ratio between the light falling onto the 2×2 central pixels (P) of each μ-PSF and the total light falling on the corresponding lens (T). Fig.6.10 at top shows the distribution of P/T for all the 1024 lenses for the "quasi-instantaneous" exposure (0.5 ms): we can see that while for the majority of the lenses the values cluster around 0.77, which is the value for a uniformly illuminated aperture, there

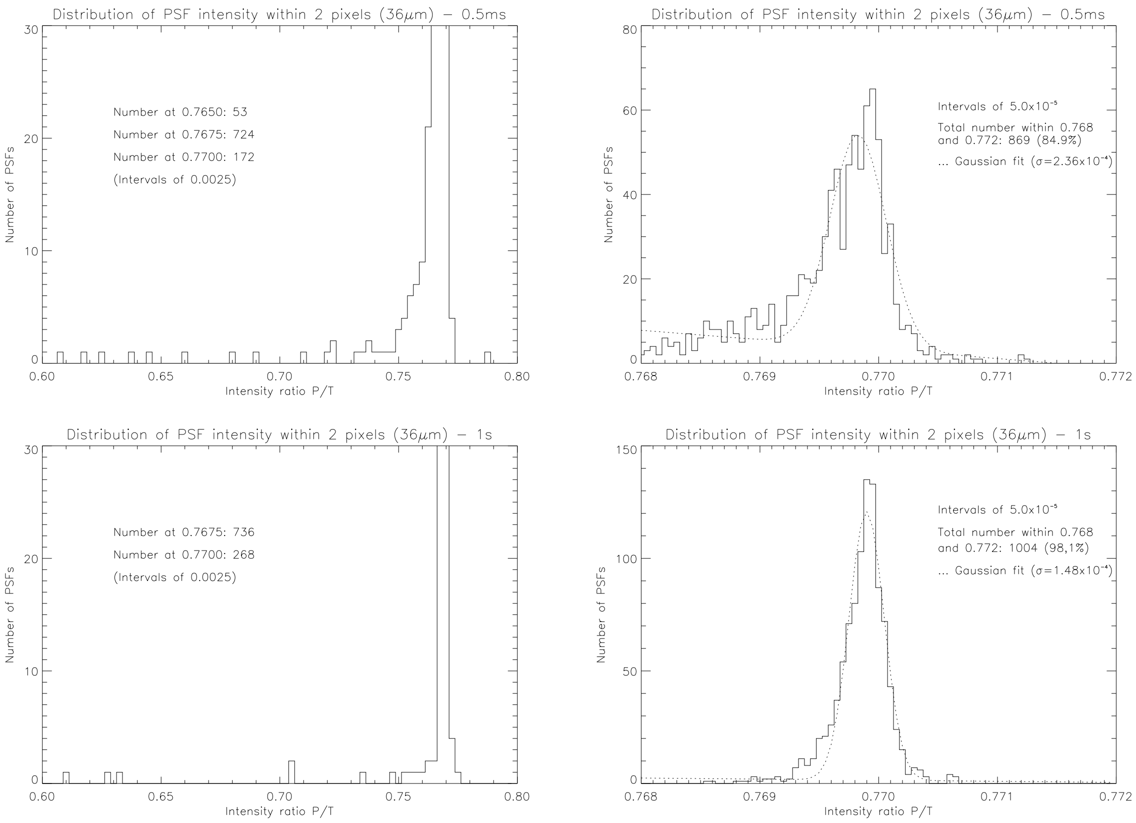

Figure 6.10: Distribution of the intensities within the 2×2 central pixels of the PSF provided by each lens, normalized to the total flux incident on the lens (P/T). At top left: Results for a quasi-instantaneous exposure (0.5 ms); at bottom left: Results for a 1 s of exposure. In these plots the range on the y-axis has been cut to 30 to make them readable: the values larger than 30 are labeled in the figure. The plots at right are enlargements of the peaks of the distribution shown at left, with overimposed the Gaussian fits. All details are written in the text.

is a significant minority of the cases in which the central peak contains a substantially smaller fraction of the light falling onto the lens. These cases of anomalous μ-PSFs systematically resulted to correspond to cases in which the lenses have a very low illumination level.

In the case of 1 second exposure (Fig.6.10 at bottom) the vast majority of lenses provide very similar values of P/T, and the distribution can be represented by a Gaussian curve centered at 0.7695 with σ of $1.5{\cdot}10^{-4}$. Only a small minority (20 out 1024, less than 2%) of lenses have values of P/T strongly deviating ($|\Delta P/T| > 0.002$), always in the negative direction.

The wings of the PSF (i.e. the cross talk) are supposed to be, for the μ-PSFs generated by lenses not uniformly illuminated, on average about 2-3 times higher than for the other PSFs. Cross talk from one spectrum appears at different wavelength

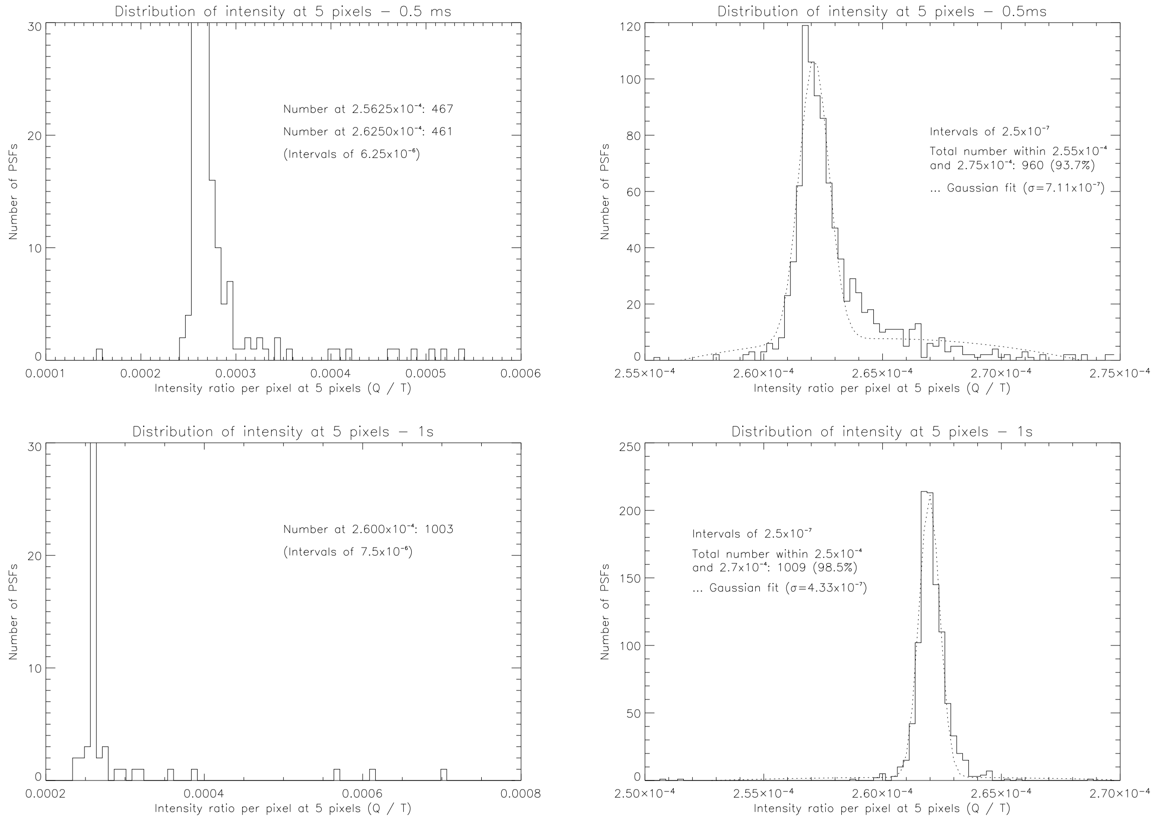

Figure 6.11: Distribution of the mean intensities at 5 pixels from the center of PSF (cross talk) provided by each simulated lens and normalized to the total flux incident on the lens (Q/T). At top left: distribution for 0.5 ms; at bottom left: Distribution for 1 s. As explained for Fig.6.10, the plots have been cut on the y-axis at the value of 30. At right the peaks of the distributions are enlarged and fitted by Gaussian curves. All details are described in the text.

in the neighbouring spectrum, generating a spectral signal: for this reason it has to be kept small ($\leq 10^{-4}$). To test the r.m.s. of the cross talk due to this effect, we simulated again 1024 μ-PSFs and we computed the distribution of the mean intensities at 5 pixels from the center of each PSF (Q), normalized to the total flux incident on the lens (T). These distributions are shown in Fig.6.11 for 0.5 ms and 1 s of exposure. For quasi-instantaneous exposure (0.5 ms) we note that most of the lenses produce a cross talk of $2.62 \cdot 10^{-4}$, very close to that given by a uniformly illuminated aperture. There are few outliers, at larger values of Q/T. Again, these outliers correspond to lenses having lower than average illumination. For 1 second, the distribution of cross talk is much narrower, can be fitted by a Gaussian centered in $2.62 \cdot 10^{-4}$ (σ=$4.55 \cdot 10^{-7}$) and the number of outliers ($|\Delta Q/T| > 10^{-5}$) is smaller but still not negligible (15 of 1024).

A typical Planet Finder exposure will consist of several hours of integration time (around 10^4 seconds): an exact simulation over such a long exposure time is beyond our technical capabilities. But we can make some assumptions on the nature of speckles and their life time to make possible a statistical approach.

If we suppose that speckles are generated only by atmospheric turbulence, which means that we neglect static aberrations or suppose the life time of static aberration very short (few milliseconds), then an exposure of 10^4 seconds will be the sum of $>3{\cdot}10^6$ typical speckle patterns (assuming the life time of a speckle pattern <3 ms). In this case we can simulate the effects of the random speckle pattern over such long exposure times using a boot-strap procedure: for each lens we constructed a series of 14400 (4 hours) values of T and P by using random extraction from the observed distribution of values obtained in 1 second exposure[3]. Fig.6.12 shows both the distributions of P/T and Q/T obtained in this way for a 4 hours exposure: they are now well represented by Gaussians, with no outlier. About P/T, the peak of the distribution is at 0.76954 with σ=$4.2{\cdot}10^{-5}$, and since this σ is smaller than the value of the target flat field accuracy (10^{-4}), we conclude that the effect of not uniform illumination of a lenses over the average intensity of the central peak of the diffraction pattern is negligible in these conditions.

A similar conclusion can be achieved for the cross talk. With non-uniform illumination, the peak of the distribution of Q/T is at $2.6284{\cdot}10^{-4}$, with σ=$8.87{\cdot}10^{-8}$. Again, we can conclude that the effect of not uniform illumination of the lenses over the average value of the cross talk is small for long exposures.

Very different is the case of not negligible static aberrations life time: these aberrations are expected to create speckle patterns that do not change within several minutes. Actually, we do not know with precision how long this life time can be: the best thing to do at this point would be to assume the worst case as a conservative hypothesis, and this is the case of completely static aberrations, with infinite life time. The procedure of boot-strap suggested before are no more possible now: the "atmospheric" speckle patterns become negligible with respect to the "static" one, and the result for 4 hours should be comparable to the one simulated at very short exposure times (0.5 ms).

Even if this is a very conservative hypothesis, we should conclude that the presence of quasi-static aberrations can generate, in case of a 4 hours exposure time, significant variations to a fraction (between $\sim$10% and $\sim$15% in the worst cases) of the μ-PSFs.

---

[3] This procedure is appropriate, because the speckle pattern characteristic of a 1 second exposure is independent on the next one.

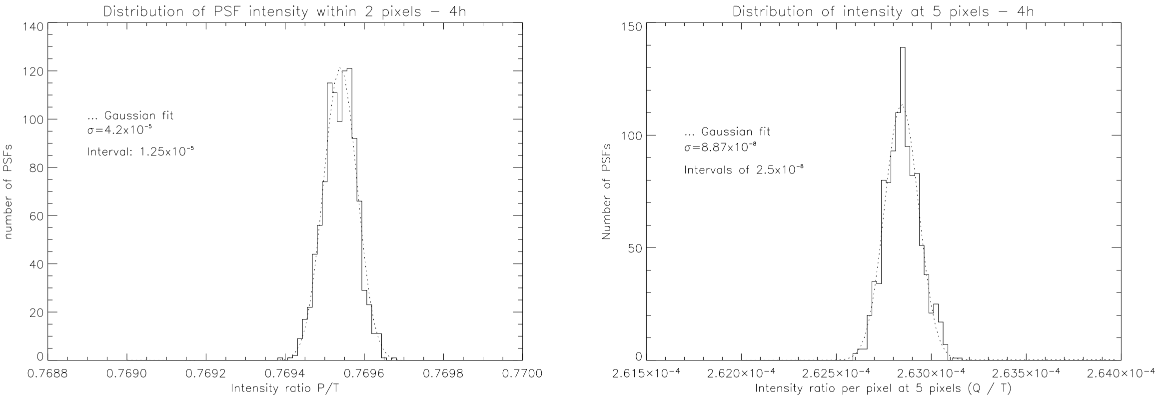

Figure 6.12: At left: Distribution of the ratio P/T (as defined in the text) for an exposure of 4 hours, estimated using a boot-strap procedure. At right: Distribution of the ratio Q/T for an exposure of 4 hours, again obtained using a boot-strap procedure. In both figures the Gaussian fit is overplotted. All details are explained in the text.

It is important to note that the main consequence of this effect is the generation of false alarms in the final detection. An accurate strategy for identifying false alarms can be extremely helpful in reducing the impact of this problem.

6.3.2 Detailed simulation of TIGER: the speckle chromatism and undersampling

To correctly simulate an IFS, we should inrtroduce an uncertainity on the central wavelength that has to be associated to every pixel of the spectra. Practically, we have to take into account that the position of the micro-PSFs generated by the lenslets cannot be always the same with respect to the grid of pixels of the detector, but we have to associate at every pixel of the spectra a different central lambda λ_c that can be known only after a procedure of calibration. The difference is arbitrarily expected to be in absolute value less than or equal to half of the dispersion of the spectrograph, in the TIGER case it is $\leq 0.02\,\mu$m.

In the simulation, when the code calculates the position of the PSFs as a function of the current wavelength λ, we apply at all the lenses a specific additional dispersion $\delta\lambda$ different from lens to lens. This $\delta\lambda$ is fixed to the lenses, which means that even changing λ the $\delta\lambda$ remains the same. The result is that at the end the central wavelength that we have to associate to the central pixel of the PSF is $\lambda_c = \lambda \pm \delta\lambda$.

The procedure of calibration has to be added in the CSP-ANALYSIS code, because is part of the data-reduction procedure. It is made in three steps:

- First of all, we simulate the observations of three lamps (one observation for each lamp). These lamps are supposed to present a gaussian response in wavelength, centered on well known λ_A, λ_B and λ_C. The three wavelengths are chosen in order to be one on the red side, one on the center and one on the infrared side of the spectral range of IFS (we used respectively λ_A=1.0131, λ_B=1.1429 and λ_C=1.2776 μm). The FWHM of these gaussians is not narrower than 3-4 spectral pixels, so they can be considered well sampled by our IFS. The lamps are illuminating uniformly all the lenses of the IFU.

- The code reads all the spectra generated in this way from the three images A, B and C: for each spectrum it reconstructs the original gaussian shape, in order to find the position of the center with respect to the detector pixels. From the combination of the three wavelengths we can write a table presenting, for each spectrum, the determination of $\delta\lambda$ and its residual error.

- Finally we take the observation of the stellar system, and considering the table of $\delta\lambda$ previously calculated we can interpolate all the spectra in order to transform the counts per pixel information we have in a flux per wavelength interval.

The interpolation made at the last point is the most delicate process in the data-reduction procedure, because, if the spectral variations are not well sampled, it introduces the problems presented in detail in Sec.4.2.

At this point, a dedicated simulated observation has been analyzed to study the reduction of speckle noise that can be achieved. As explained in detail in Sec.4.3.2 we expected, with the TIGER optical design, a small Nyquist Radius (0″.30). Since in our simulation the coronograph is covering all the region between 0″ (the center of the star) and ∼0″.25 (the border of the Lyot stop), we conclude that the region not affected by undersampling is very small.

In Fig.6.13 at top it is shown the ratio between the residual noise, obtained after subtraction of the spectra, and the initial value of noise (speckle noise), as a function of the angular separation from the center of the field[4]. On the same plot also the ratio between photon noise and the initial speckle noise is presented. We can easily see that in these conditions it is not possible to reach a noise level comparable to the photon noise, at any distance from the center. The level achievable of noise is larger than 1/10 of the initial speckle noise, while to be at the same level of

---

[4] The center of the FoV corresponds always, in our simulations, with the position of the star.

the photon noise we need a factor of ∼1/1 000. This factor was actually achievable in the old simulations presented in Sec.6.2. In conclusion, we need to improve the capabilities of this technique of a factor ∼100, as shown clearly in Fig.6.13 at bottom. It is also important to notice that there is no evidence of an improvement at very short distances (within the Nyquist radius).

From these results, it is possible to have an idea of the limit contrast reachable between the noise level after subtraction and the intensity of the stellar peak, and we found that it cannot be much better than $\sim 10^{-6}$, that is the minimum requirement for SPHERE-IFS, but the goal was 10^{-8}.

In conclusion, this first test demonstrated clearly that the problem of speckle undersampling in the TIGER design is significant and must be taken seriously into account.

6.3.3 Detailed simulations of HYPERTIGER

The studies presented in the previous sections demonstrated, as expected, that the TIGER concept has to be substituted by a new concept, that does not present so strong problems of speckle undersampling. At the same time, we suppose that the choice of micro-PSFs with FWHM smaller than a pixel on the detector is no more appropriated, because to avoid undersampling we need to sample the PSFs with at least 2×2 pixels. For this reason the new simulations followed the HYPERTIGER optical design, as described in Sec.4.3.2. The code has been not modified to simulate the HYPERTIGER, we only changed some input parameters. We remind here the three important differences between TIGER and HYPERTIGER: the resolution is now 24 (and consequently the field of view is reduced to 1".49), the focal ratio is 16 instead of 8, the IFS magnification is 2.16 instead of 1.00 (see Tab.4.1 for the other parameters).

The results obtained have been analysed exactly like the ones for TIGER. In this way we can present, in Fig.6.14, a direct comparation between the two cases, in terms of speckle noise reduction with respect to the photon noise in logarithmic scale. The spatial ranges are different, since the two concepts have different field of view. It can be seen that the reduction of speckle noise given by HYPERTIGER is roughly a factor 3 lower than in the TIGER case.

Even if the improvement of the speckle noise subtraction is clearly not as good as expected (we are still far from the photon noise), this results are enough to reach the required limit contrasts between planet and star ($\leq 10^{-6}$). We can summarize

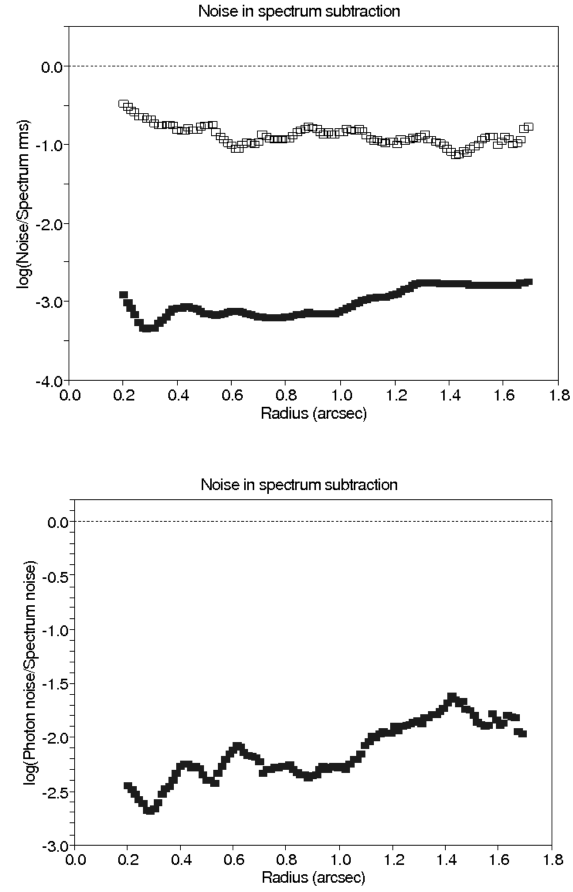

Figure 6.13: At top: Run of the logarithm of the ratio between the photon noise and the spectrum r.m.s. (filled squares) as a function of angular separation. The same run but using the reduced noise in the subtracted spectrum is shown with empty squares. The dotted line represent the case of no improvement of the noise level using subtraction. Therefore, the reduction of speckle noise in this case can not be, in this situation, larger than a factor of 10, when it is necessary, to reach the photon noise, a factor of 1 000. At bottom: Run of the logarithm of the ratio between the photon noise and the reduced noise. It is evident that the difference between the two levels of noise is still of a factor of 100.

the achievable contrasts in Tab.6.4: at certain separations (larger than 0.5-0.6 arcseconds) we are below 10^{-7}.

With the results given by the new simulation it has been possible to re-draw the plots in Fig.6.9. Even if at a first glance the new plots (Fig.6.15) do not differ very much from the previous ones, we can notice a significant decrease of the number of companions detectable at more than 10 pc, with strong consequences on the possible target list.

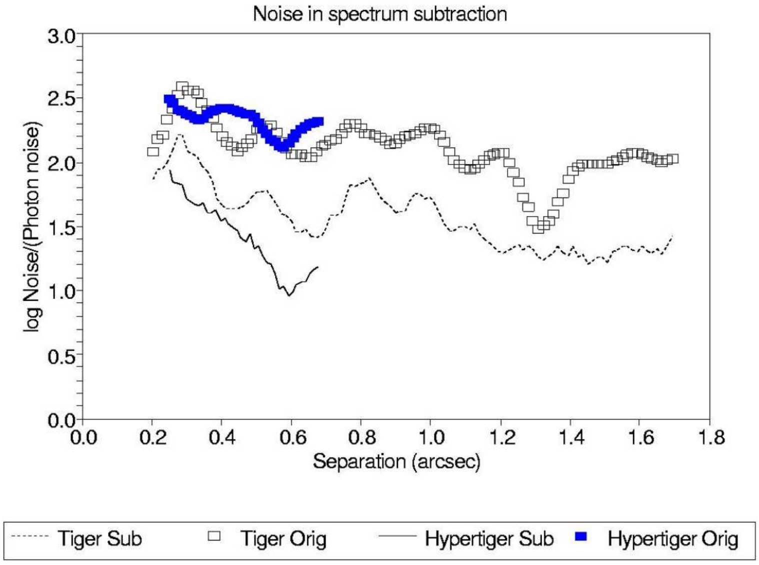

Figure 6.14: Comparison between the IFS solutions simulated: the squares (blue and white) represent the noise of the simulated spectra before speckles subtraction, respectively for HYPERTIGER and TIGER; the lines (continuous for HYPERTIGER and dotted for TIGER) represent the level of noise after the subtraction. The noise is presented as a ratio between the total noise and the photon noise.

Radial coordinate (arcsec)	TIGER	HYPERTIGER
0.5	$4.55{\cdot}10^{-7}$	$2.13{\cdot}10^{-7}$
0.6	$2.78{\cdot}10^{-7}$	$5.56{\cdot}10^{-8}$
0.7	$3.70{\cdot}10^{-7}$	$9.09{\cdot}10^{-8}$

Table 6.4: Limit contrasts (5 sigma over the central 4 pixels of the planet image) for different distances from the field of view center, adopting the two simulated solutions for IFS.

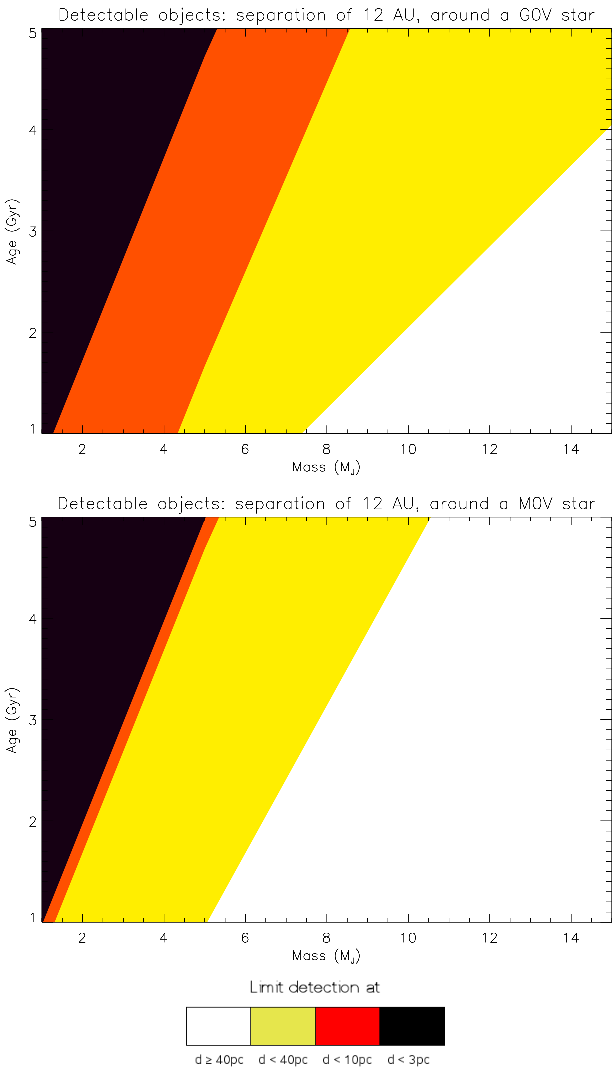
Detectable objects: separation of 12 AU, around a G0V star

Detectable objects: separation of 12 AU, around a M0V star

Figure 6.15: Planets detectable with a signal-to-noise ratio higher than 5, as function of mass and age, in the case of a G0V (at top) and a M0V (in the middle) host star. This are the same plot as in Fig.6.9, but considering a speckle subtraction of a factor of ~10, as provided by HYPERTIGER simulations. Passing from the old CHEOPS results to these new ones, the red region appears larger, which means that many objects visible at 10 pc previously now are detectable at 3 pc. The black region, with planets not detectable even at 3 pc, does not change significantly.

Chapter 7

Simulations of observations at an Extremely Large Telescope

7.1 Simulations of IFS on an ELT

Since in the CSP simulations the main features of the telescope are introduced as input parameters, the code can be easily used to simulate observations obtained with any kind of telescopes. Therefore it can be helpful to understand what is the improvement on the planet detections achievable changing telescope.

In particular we focused our attention on the new generation of telescopes under project now, known as Extremely Large Telescopes (ELTs): these telescopes are characterized by a diameter larger than 10 m, that is the maximum present size, up to a hundred meters. An IFS-SDI instrument mounted on such a telescope will take advantage of the large diameter D in two ways:

- Increasing the spatial resolution, because the FWHM of a diffraction limited PSF is proportional to D^{-1}. This means that planets physically very close to the host star would be observable, in other words that we can investigate the central part of far planetary system, outside the limitations of VLT presented in Sec.4.4.1. Anyway this advantage requires, in order to be really useful, an extreme AO system with high performances, that can be difficult to provide for very large D;

- Increasing the number of collected photons per second, proportional to D^2. The large amount of light will make possible in few minutes observations that on VLT would have required many hours. Therefore, keeping an exposure time of hours like in the VLT case, it would be possible to detect very faint planets.

With the work presented in this chapter we wanted to demonstrate, via simulations, that this new generation of telescopes, combined with the IFS-SDI technique, can drastically improve our knowledge about extrasolar planets. In particular, we wanted to estimate the chances of detection of Earth-like planets, and the signal-to-noise ratio we can expect.

The parameters that has been changed in the simulations, as a function of the telescope, have been: the telescope diameter, the diameter of the secondary mirror, the pitch of a lens in angular units, the pixel-per-meter scale of the phase screens (see Tab.5.1). Obviously the pupil mask has been substituted by the entrance pupil of the new telescope.

Then particularly important has been the preparation of the phase screens: in these screens were included both the correction of AO and the static aberrations of the telescope. We chose, in our simulations, to base in general these instrumental features on the present experience on 8-10 m class telescopes. Knowing the difficulties of adapting a XAO system to an ELT, we not expected the Strehl Ratio to be larger than 0.65 in all the cases. In the next future, maybe the technology will be able to give us more stable instruments with a better control of noise sources: in that case, the Strehl Ratio would be higher, but in this simulations we chose a conservative approach.

7.1.1 Detecting planets with segmented mirrors

An important difference between small telescopes and large telescopes is that the latter, for practical reasons, have not monolithic mirrors but in general segmented mirrors. Expecially when we are in presence of a large number of segments, some diffraction effects arise that have to be taken into account. As clearly explained in Yaitskova et al. (2003), a segment surface acts as a giant bidimensional diffraction grating, producing an interference pattern with regular peaks: practically we can analytically consider the PSF generated by a segmented telescope as the product of two factors, a grid factor GF, which is the Fourier transform of the segmentation grid and is a periodic function of sharp peaks, and the PSF of an individual segment (PSF_s). As visible in Fig.7.1, a segmented mirror with hexagonal grid produces high-order peaks with a $\pi/3$ symmetry.

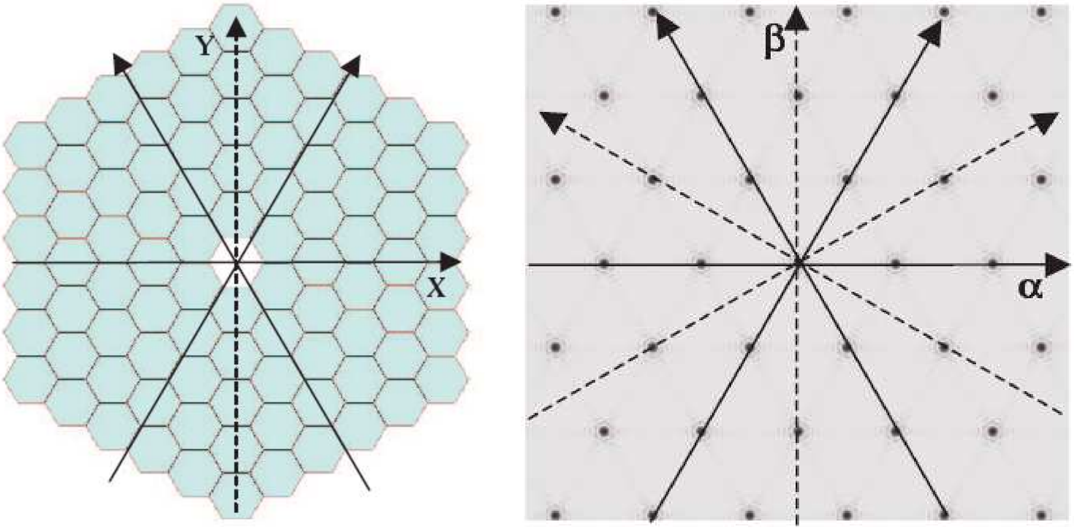

Figure 7.1: At left: example of a segmented mirror; the solid arrows illustrate the hexagonal symmetry. At right: the geometry of the grid factor GF; the $\pi/3$ symmetry is maintained in the Fourier plane, and the peaks are located equidistantly along the solid and dashed arrows. Both figures are taken from Yaitskova et al. (2003).

Although the intensity of the high-order peaks is always 10^{-4}, 10^{-5} times the intensity of the central peak, in the search of extrasolar planets, where the intensity ratios can reach 10^{-9} or 10^{-10} for Earth-like planets, the presence of these peaks can be a significant source of false alarms.

Almost all the ELTs we simulated present segmented mirrors with hexagonal symmetry, and the only exception, the Giant Magellanic Telescope GMT, has a structure that can be considered practically as a hexagonal grid. Therefore, our simulations can be used also to test the influence of these peaks in the detection of planets and estimation of false alarms frequency.

7.2 A 100 m telescope: OverWhelmingly Large telescope OWL

The OverWhelmingly Large telescope (OWL, see e.g. Dierickx & Gilmozzi, 2000) was a concept of a 100-m class ground-based optical telescope, with multi-conjugate adaptive optics capability. The science objectives of OWL are an angular resolution around 0.001 arcseconds or less in the visible range, and a sensitivity to faint fluxes ideally affording the detection of Cepheids out to redshift $z \leq 1$, or supernovas at $z \geq 10$. This requirements translate directly into a collecting area between 6000 and

7000 m^2, and therefore into a diameter $D \geq 100\,\mathrm{m}$. The optical quality requirement is set to Strehl Ratio $>20\%$.

The design of the telescope optics is constrained as follows: Segmented surfaces must be spherical; the monolithic mirrors must have diameters not exceeding 8.2 meters; the structure height must be minimized. These constraints imply a fast spherical mirror; consequently we need a large, spherical and segmented secondary, that will result to be 35 m wide. Segments should have a diameter of around 2 m, and consequently the primary mirror would be made of about 1500 segments and the secondary of about 200 segments. Fig.7.2 shows the entrance pupil, in which is visible the segmentation of both primary and secondary mirror, and the diffraction limited PSF expected.

Anyway, the concept of a 100-m telescope resulted to be too complicated and expensive for the present technology (Monnet & Gilmozzi, 2006); so its design would be probably adapted for a smaller size, of the order of 50 m.

Simulations of 100-m OWL have been made using the entrance pupil in Fig.7.2. Some preliminary results, obtained with the IFS TIGER design, have already been presented in Berton et al. (2006c), while the new simulations presented here are all obtained with HYPERTIGER design. The pixel-per-meter scale was 10 (instead of 100 used for VLT); the resulting field of view covered by a single lens had a size of 0.00122 arcseconds, to properly sample the FWHM of the diffraction limited PSF. To allow results at 0.1 arcseconds or beyond, we simulated more lenslets than in the VLT-HYPERTIGER case, covering a field of view much larger than expected (0.18×0.18 arcseconds): therefore, the size of the simulated detector is double than the VLT case (4096×4096).

A series of simulations have been done also using an hypothetical 50 m OWL, simply scaling the entrance pupil of a factor of 2: in this case the features of the instrument remain the same, but the size of the primary and secondary mirrors, of all the segments, of the spiders, etc., have been divided by 2. The field of view is not changing, and so the spatial and spectral sampling: but the spatial resolution (i.e. the size of the Airy disk) and the number of photons collected are very different from the 100 m case.

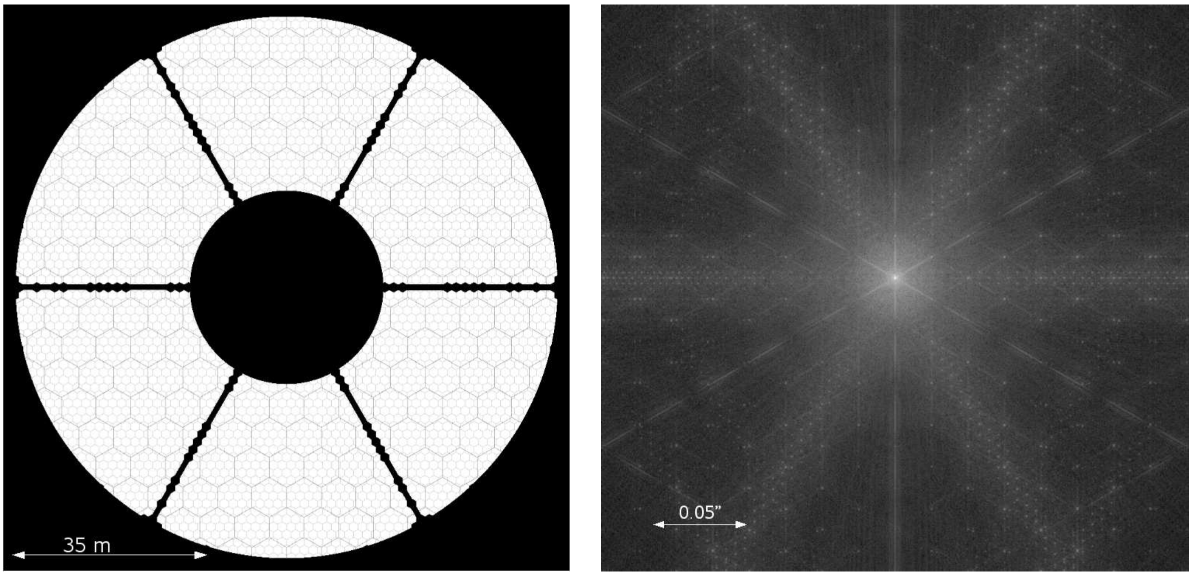

Figure 7.2: At left: entrance pupil of OWL, considering the segmentation of both the primary and secondary mirrors and the spiders (from Yaitskova et al., 2003). At right: the diffraction limited PSF of OWL; two grids of high order peaks are visible, because the secondary mirror is also segmented. The PSF is in logarithmic scale.

7.3 A 30 m telescope: the TMT Thirty Meter Telescope

The Thirty Meter Telescope TMT (Crampton & Ellerbroek, 2006) aims to provide a 30-m ground based facility capable of delivering diffraction limited images as well an order of magnitude increase in raw light gathering power, compared to the current 8-10 meter telescopes. It will be composed by a 30 meter highly segmented primary mirror and a 3.6 m monolithic secondary, in a Gregorian configuration. The size of the segments is expected to be around 0.5 m. The spatial resolution will be in visible around 0.0035 arcseconds. The particular shape of the spiders is visible in the pupil in Fig.7.3 at top left, that we also used for the simulation. This time the lenses are covering a pitch of 0.00366 arcseconds, to properly sample the FWHM of the diffraction limited PSF.

7.4 A 21 m telescope: Giant Magellan Telescope GMT

The Giant Magellan Telescope (GMT, McCarthy, 2006), by virtue of its dilute aperture, is not easily characterized by a single diameter, but its primary mirror is actually a combination of seven primary mirror segments that produce a total collecting area equivalent to a filled aperture 21.45 m in diameter. For diffraction limited work, and therefore to estimate the FWHM of the diffraction limited PSF, the edge-to-edge diameter of 25.4 m is more relevant. The segments are circular, 8.4 m in diameter, the optical configuration is an aplanatic Gregorian, the secondary mirror will consist of seven segments aligned with the seven primary mirrors (diameter of 1.06 m each), with a total size of 3.5 m, and it will be adaptive. The particular secondary configuration results in a PSF almost free of diffraction spikes associated with conventional secondary supports.

For the simulations, we used the entrance pupil in Fig.7.3 at bottom left. The expected angular resolution is ∼0.004 arcseconds, so the angular size to be associated to every lens remains 0.00366 arcseconds like in the TMT case.

7.5 Results

In this section we present the results obtained with simulations of the four considered cases: 100 m OWL, 50 m OWL, TMT and GMT. The main results are summarized as follow:

Factor of reduction of speckle noise in the OWL case (100 m)

The reduction of speckle noise can be calculated as already done for TIGER and HYPERTIGER in Sec.4.3.2. The level of the noises before and after the differential imaging have been studied in detail, and from Fig.7.4 we can see that the reduction of speckle noise is comparable to what obtained for HYPERTIGER on VLT, but at completely different angular separations (here much smaller). In conclusion, we have a reduction of speckle noise of around 1/10 in the whole range between 0.02 and 0.18 arcseconds[1].

Simulations of a very young Jupiter-like planet detection

For all the four telescopes considered we simulated a planet of 1 M_J, 10 Myr old, placed, when possible, at two different separations from the host star (a solar-type star, placed 10 pc from the Sun): 1 AU and 3 AU, corresponding to angular separations of 0.1 and 0.3 arcseconds. For OWL, in both cases, the separation of 0.3 arcseconds is outside the field of view, and for this reason it was not simulable.

---

[1] It is important to note that the lower Strehl Ratio simulated in the ELT cases (∼0.65 instead of ∼0.80 of the VLT case) is affecting the performances of IFS-SDI in a direct comparison to the VLT case, in particular because of the brighter PSF halo that means higher photon noise.

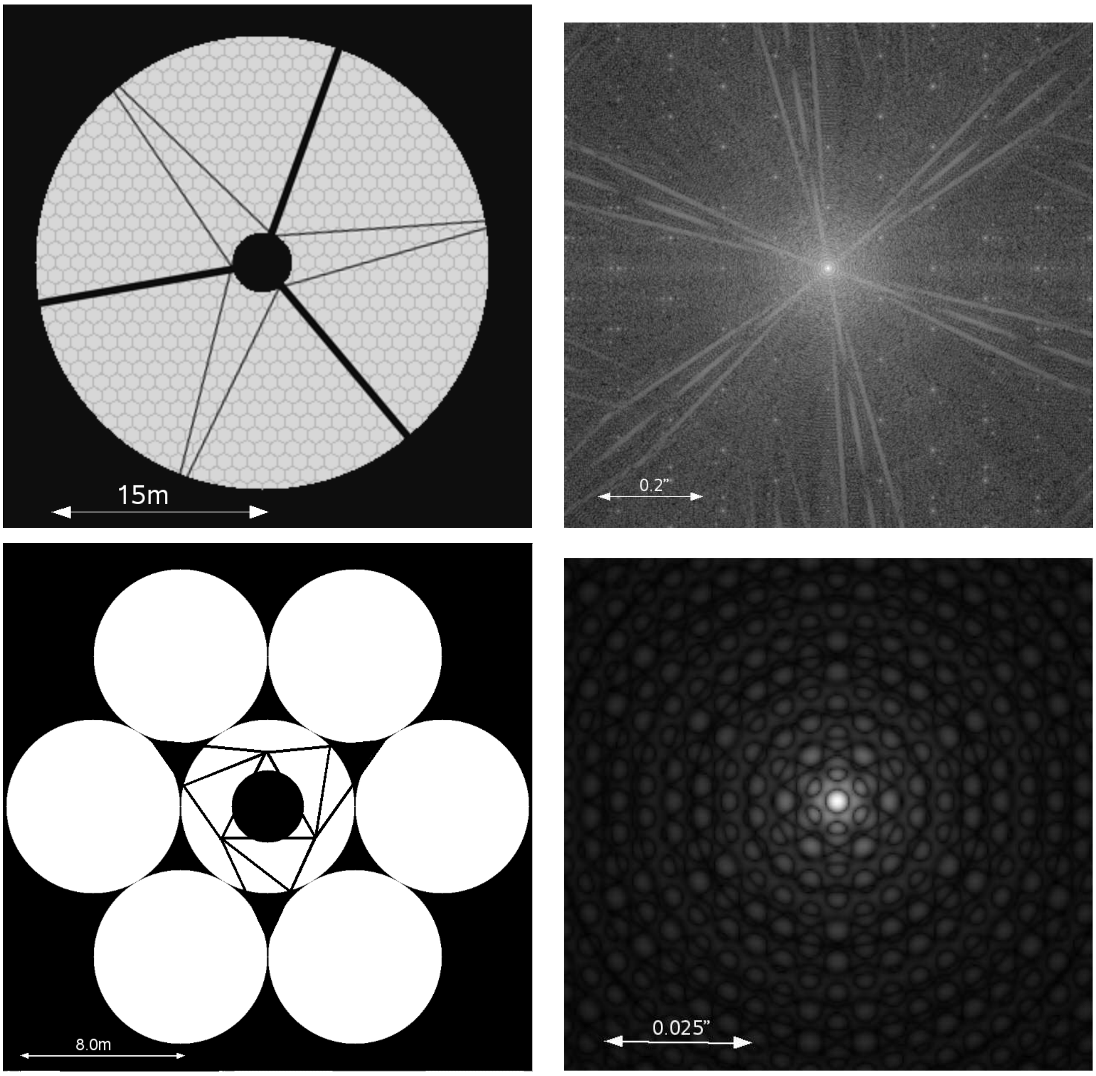

Figure 7.3: At top left: simulation of the entrance pupil of TMT. At top right: the diffraction limited PSF of TMT. At bottom: entrance pupil and diffraction limited PSF for GMT. All PSFs are in logarithmic scale.

The planet has been detected in all cases with the signal-to-noise ratios reported in Tab.7.1, second column. From this number we calculated the time needed to achieve the minimum S/N to consider the planet detected, that is supposed to be 5. For the 100 m telescope we found that 1 second is enough, while for a 50 m we need around 1 minute, and 25 minutes for 30 and 25.4 m.

Limit contrasts achievable

It has been an interesting test, at this point, to derive what is the limit contrast achievable at each separation with each telescope. It could be done in two ways:

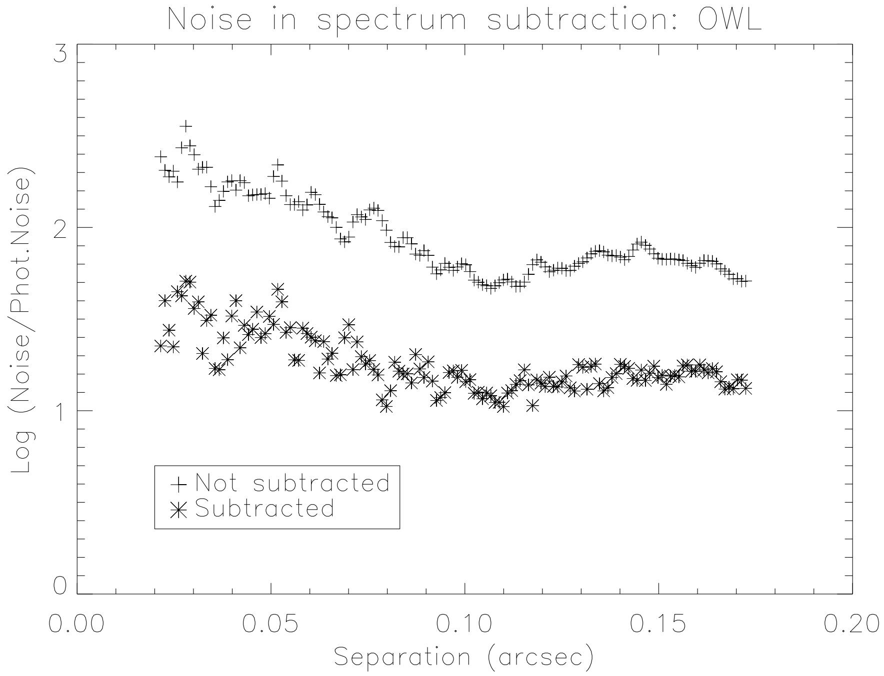

Figure 7.4: Ratios between the noise of the simulated spectra and the photon noise, before speckles subtraction (crosses) and after speckle subtraction (asterisks). Data taken from the simulated observations of OWL with IFS (HYPERTIGER design). If compared with Fig.6.14, these curves present more or less the same factor of reduction of speckle noise of the HYPERTIGER case for VLT, but for different separations.

the first is to use the S/N obtained in the case considered (where the contrast I_p/I_s, flux from the planet divided by flux from the star, is around 10^{-6}) to determine for which I_p/I_s the signal-to-noise would have been 5 in 4 hours of exposure. The second way is an analysis detailed of the residual noise after subtraction (like in Fig.7.4) to estimate the contrast between the central peak of the stellar PSF and the noise at the requested separation. The numbers presented in Tab.7.1, fourth column, are an average of the results used in the two cases.

Discussion of the results, and considerations on a Earth-like planet detection

At a first glance, we can notice from these results that the considered planet, surely very young and consequently much brighter than a old-cold Jupiter-like object, is easily detected in all the cases. But the limit contrast LC is higher than what actually expected. In fact, except for the 100 m telescope, this values are not much lower than what predicted by the VLT simulations (see Tab.6.4). Obviously, the separations and the profile of the PSFs are different, but if we consider the dimen-

Telescope	S/N	t_5	LC	λ/D
	Separation 1 AU			
OWL (100 m)	640	<1 s	$\sim 5{\cdot}10^{-9}$	42.2
OWL (50 m)	85	50 s	$\sim 4{\cdot}10^{-8}$	21.1
TMT (30 m)	15	1500 s	$\sim 2{\cdot}10^{-7}$	12.6
GMT (25.4 m)	15	1500 s	$\sim 2{\cdot}10^{-7}$	10.7
	Separation 3 AU			
OWL (100 m)	*Out of the Field of View*			126.5
OWL (50 m)	*Out of the Field of View*			63.2
TMT (30 m)	75	65 s	$\sim 5{\cdot}10^{-8}$	37.9
GMT (25.4 m)	70	75 s	$\sim 6{\cdot}10^{-8}$	32.1

Table 7.1: Simulations of observations of a 1 M_J, 10 Myr old planet around a solar-type star, at 10 pc from the Sun. For two different separations, 1 AU and 3 AU (corresponding to angular separations of 0.1 and 0.3 arcseconds), we report the signal-to-noise ratio (S/N) of the detection in 4 h of exposure time, the time needed to reach S/N=5 (t_5), and the expected limit contrast LC reachable in 4 h of exposure. The value of LC is evaluated taking into account the S/N and a more detailed analysis of residual noises (see e.g. Fig.7.4). In the last column we report the two separations expressed in unit of λ/D.

sion λ/D, reported on the last column of Tab.7.1, and that is equal to $\sim$20 in case of 0.6 arcseconds on VLT, we conclude that the LC obtained with VLT at 0.6 arcseconds can be compared to the one obtained with a 50 m telescope at 0.1 arcseconds (λ/D=21.1), and the two LCs are actually of the same order of magnitude (few units of 10^{-8}).

Moreover, The time needed to reach a 5-σ detection, hereafter called t_5, is shown for the various cases (including a 10-m class telescope) in Fig.7.5. We know from theory that it should be proportional to D^{-4}, but in our case we see that for 25, 30 and 50 meters t_5 is clearly higher than expected from VLT simulations.

The reason of this high limit contrasts has probably to be found in our choice to make simulations based on some input parameters neither extremely optimistic nor pessimistic, because the AO correction, the static aberrations, the detector noise and in general all the instrumental features have been simulated basing on the present experience with 8-10m-class telescopes. In particular, the use of an AO system with an expected Strehl Ratio around 0.65 is a big limitation if compared with the Strehl Ratio for VLT that was around 0.8. We think that if it would be possible in the future to reach a goal of 0.8 or higher we can reduce significantly the inten-

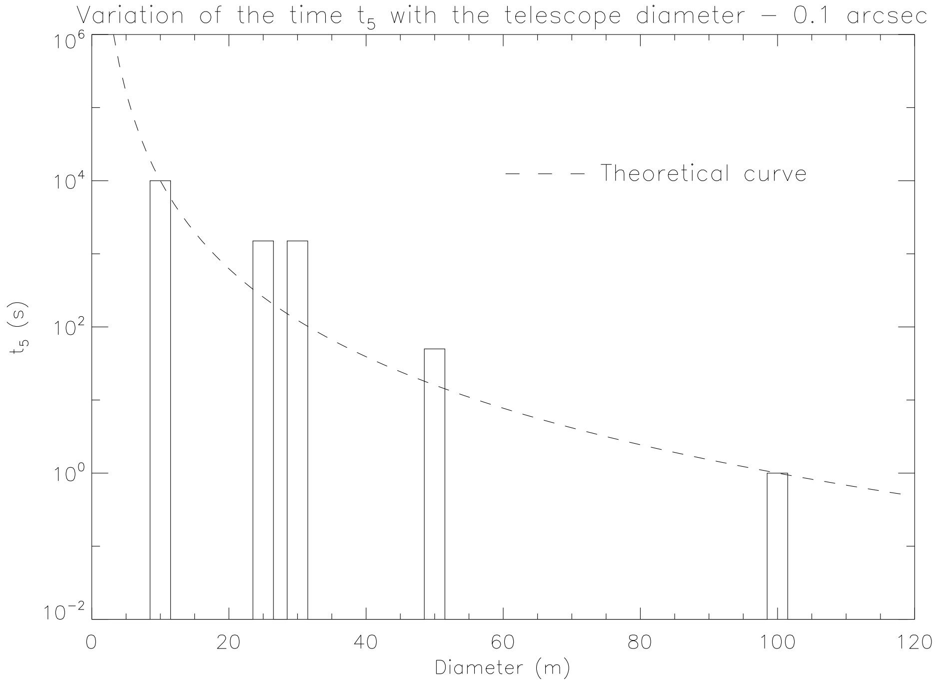

Figure 7.5: Time needed to reach a 5-σ detection (t_5) as a function of the telescope diameter. The data are obtained by simulations of a $1\,M_J$, 10 Myr old planet around a solar-type star, at 10 pc from the Sun (see Tab.7.1). The separation between star and planet is 0.1 arcseconds. The value of t_5 for a 10-m telescope is extrapolated from the simulated data for VLT, using the CSS spreadsheet (see Sec.6.2). The dashed line represents a theoretical curve, proportional to D^{-4}, that shows the predicted variation of t_5 for different diameters, normalized to the VLT result. The values obtained for 25, 30 and 50 meters are clearly higher than expected.

sity of the seeing disk, and furthermore a coronograph device can be considered to reduce the photon noise. Only in this case the 2 sets of results (for VLT and ELTs) would be really comparable.

The detection of an Earth-like planet would be possible only if we can reach a limit contrast of 10^{-10}. From the results expressed above, it is not possible to reach this contrast within an exposure of 4 hours. A new calculation has been done, taking into account the differences in spectrum between an Earth-like planet and a Jupiter-like one (no more CH_4 bands, but water and molecular oxygen). It is important to note that the atmospheric features we want to observe on the planet are exactly the same present in our atmospheric spectrum, which means that some corrections have been applied, adding noises in the data analysis phase. The result is that to detect this kind of planet, at 1 AU, we need around 1000 hours, and the observation is practically not feasible (Berton et al., 2006c).

Finally, we can also notice that the results obtained for GMT and TMT are very similar. Apparently, the advantages of using a 30 m with respect to a $\sim$25 m telescope are not visible. This is something that can be due to, on one hand, some statistic fluctuations on our simulations (that means that probably more than one simulations should be done in each case, and the various results should be used to have a more statistically correct value: this could not be done in our case, because of the long computer time required by the IDL software); on the other hand, it would be interesting to investigate more in detail on the impact of the two completely different structures of the primary and secondary mirrors for GMT and TMT on the final detection of the planet. This consideration can lead to a new detailed work in the future.

Conclusion

At the end of this work we want to come back to the initial questions expressed in the Introduction. Is the IFS-SDI technique actually a valid technique for trying to detect directly extrasolar planets? Moreover, does it allow us a better result than a simpler, and well tested, double band SDI? We can now give an answer, with the results we obtained.

First of all, our simulations showed that IFS-SDI is a good method to reduce speckle noise. Even if we are not able to reach the photon noise level, that was the most optimistic goal, we can measure a factor of reduction of speckle noise around 10 or more, that is enough for detecting planets with a intensity contrast down to $\sim 6 \cdot 10^{-8}$ at 0.6 arcseconds from the star, in J band, in case of observation with VLT (see Chapter 6, in particular Tab.6.4). Concerning a comparison with a double band SDI, the requirement of limit contrast below 10^{-6}, that is an optimistic estimation for the capability of a double band SDI mounted on the same telescope and with the same AO corrections, is clearly fulfilled. Furthermore, we should not forget that there are some not negligible advantages from this technique: the possibility to detect many absorption bands in a single exposure, and in different positions of the spectral range; the possible combination of more than two wavelengths to better reduce the speckle noise; the characterization of the planetary spectrum.

There are anyway some things, at this point, that it is important to notice. In particular, an IFS-SDI instrument resulted to be a very complicated instrument, at least from the conceptual point of view. Some technical details have been not very easy to simulate, but at the same time they can influence in a strong way the final result. Just to make an example, in this thesis we spent some pages on describing the differences between the results obtained with TIGER and HYPERTIGER (see Chapter 6). This differences, very significative at the end, show clearly how a detail apparently not particularly important like the speckle chromatism and undersampling, and for sure not conceptually easy to understand, when simulated in the right way could affect the results. A first conclusion we can draw is, therefore, that the simulation of such an instrument, where "the devil is in the detail", requires an extreme attention. Consequently, we think that to reach an accuracy as good as possible, it will necessary in the next future to improve the software continuously, comparing the results with laboratory tests on prototypes.

Concerning the method, we want to stress again that the advantage of IFS-SDI with respect to other methods is achievable, even if it is not particularly impressive, and this advantage can allow the detection of some groups of planets otherwise hidden. But this is possible only under the condition to build up an instrument with a perfect, or almost perfect, control over static aberrations, stray light, cross talk between lenses and in particular flat field. For some of these parameters, the values we assume in simulations are not easy to achieve. In addition, this technique requires a software of Data Reduction and Data Analysis quite complicated, where new errors can be introduced. So it is easy, at the end, to find that the initial advantage had been lost.

This is true, and even more important, in the case of ELTs: we have seen how a decrease of the AO Strehl ratio have caused a significative increase of the limiting contrast of the detection, reducing strongly the usefulness of an extremely large diameter and making definitively impossible the revelation of Earth-like planets. Only with perfect control of the instrument, and a very extreme AO system, the capabilities of an ELT can be fruitfully used.

Summarizing, we think that the simulation software presented here gave us an important confirmation of the capabilities of an IFS-SDI based instrument; at the same time the software contributed in finding not expected problems and difficulties important in developing such an instrument. We conclude that this technique can bring significant improvements to the direct search for extrasolar planets, but it will require a great effort to keep under control all the sources of noise of such a complex instrument.

Appendix A

The CSS Cheops Simulation Spreadsheet

CSS calculates a set of signal-to-noise ratios of a monochromatic planet image (assumed to have the size of the Airy disk) at different separations from the star, as expected as output of a simultaneous differential imager like the CHEOPS IFS channel. Adapting the instrumental parameters to various cases, it can be used for IFS instruments other than the specific CHEOPS case. The signal is computed in physical units in different bands (R, I, J, H, K, L' and $M-$bands) for both the star and the planet. Various choices are possible for the basic parameters: stellar luminosity and distance, various planet ages and masses, planet-star separation, etc. Both intrinsic emission and reflected stellar light are considered. The intrinsic emission from planets is estimated using magnitudes from Baraffe et al. (2003) COND models. Since a flat spectrum is assumed within each band, fluxes at the ”emission peaks” in the J and H bands are underestimated by a factor of 2-3. For the reflecting light, it is assumed that the planet is at quadrature, so that the projected physical separation is the real star-planet distance divided by the distance of the star from us; and that only a fraction A_λ of the light is reflected, A_λ being the geometrical albedo from Sudarsky et al. (2000), dependent on wavelength, and has to be multiplied by the phase factor φ (0.41 for a specific phase angle of 80°) to include the geometrical effects:

$$F_{ref} = F_* \frac{\varphi A_\lambda R_p^2}{d^2}, \tag{A.1}$$

where F_{ref} is the reflected flux from the planet, F_* is the stellar flux, d is the distance between star and planet and R_p is the planetary radius.

Noise estimates include the contributions of the star and planet photon statistics, sky background, detector, and speckles, this last possibly suppressed by any predefined value. The photon noise N_{ph} is computed assuming a Poisson distribution. The sky background (B) is computed using values appropriate for Paranal, in dark sky conditions. Multiple exposures are explicitly taken into account to estimate the contribution of detector read-out noise (RON). Speckle noise is estimated as the photon noise times the square root of the total number of photons per speckle. This is obtained by dividing the number of detected photons (in the selected pass bands) by the number of speckles n, which can be obtained by Eq.3.10:

$$N_s = N_{ph}\epsilon\sqrt{\frac{F_*}{n}}. \tag{A.2}$$

The factor of reduction of speckle noise ϵ, that was in Sec.6.2.4 a function of angular separation, is here an average value for all the separations. Its value, previously calculated to be around 10^{-3}, is here enlarged to 10^{-2} to have more conservative results. The total noise N_t can be expressed in this way:

$$\begin{aligned} N_t &= \sqrt{N_{ph}^2 + N_s^2 + N_p^2 + B + RON^2} = \\ &= \sqrt{f_{seeing}(\vartheta)\left(1 + \epsilon^2\frac{F_*}{n}\right) + f_{diff}(\vartheta) + F_p + B + RON^2}. \end{aligned} \tag{A.3}$$

We indicated with f_{seeing} and f_{diff} the different contribution given to the total flux by the stellar halo and core, this one being a diffraction-limited PSF. N_p, the noise due to the planetary flux, is expressed as the square root of the flux coming from the planet, F_p, which is the sum of both reflected and intrinsic emission.

Various instrumental parameters can be defined, including spectral bandwidth, instrument efficiency, adaptive optics Strehl ratio, stray light level, etc. Various options are also possible for the atmospheric conditions (represented by the coherence time τ, usually adopted to be 3 ms in this paper, and by the seeing FWHM). The seeing PSF is assumed to be of the form defined by Racine et al. (1999). The diffraction PSF is given by a power law (with exponent -2.8), which fits well the PSF produced by detailed simulations.

Bibliography

Allard F., Hauschildt P.H., Alexander D.R., et al., 1997, Annu. Rev. Astron. Astrophys., 35, 137-77

Alonso R., Brown T.M., Torres G., et al., 2004, ApJ, 613, L153-L156

Angerhausen D., Krabbe A., Iserlohe C., 2006, Proc. SPIE, 6269, in press

Arribas S., Gilliland R.L., Sparks W.B., et al., 2006, PASP, 118, 21-36

Bacon R., Adam G., Baranne A., et al., 1995, A&AS, 113, 347

Bacon R., Copin Y., Monnet G., et al., 2001, MNRAS, 326, 23

Baraffe I., Chabrier G., Barman T.S., et al., 2003, A&A, 402, 701

Beichman C.A., Coulter D.R., Lindensmith C., et al., 2002, Proc. SPIE, 4835, 115-121

Benedict G.F., McArthur B.E., Forveille T., et al., 2002, ApJ, 581, L115-L118

Berton A., Gratton R.G., Feldt M., et al., 2004a, Proc. SPIE, 5490, 672-682

Berton A., Kellner S., Feldt M., et al., 2004b, Proc. SPIE, 5490, 661-671

Berton A., Gratton R.G., Feldt M., et al., 2006a, PASP, 118, 1144B

Berton A., Gratton R.G., Antichi J., et al., 2006b, Proc. SPIE, 6269, 192B

Berton A., Feldt M., Gratton R.G., et al., 2006c, IAU Symposium, 232, 339-343

Biller B., Close L., Lenzen R., et al., 2006, IAU Colloquium, 200, 571-576

Bond I.A., Udalski A., Jaroszyński M., et al., 2004, ApJ, 606, L155-L158

Brunini A., Benvenuto O.G., 1996, MNRAS, 283, L84-L88

Burrows A., Hubbard W.B., Lunine J.I., et al., 2001, Reviews of Modern Physics, 73, 719-765

Burrows A., Sudarsky D., Hubeny I., 2004, ApJ, 609, 407

Butler R.P., Marcy G.W., 1998, ASP Conference Series, 134, 162B

Chabrier G., Baraffe I., 2000, Annu. Rev. Astron. Astrophys., 38, 337-77

Charbonneau D., Brown T.M., Latham D.W., et al., 2000, ApJ, 529, L45-L48

Chauvin G., Lagrange A.M., Dumas C., et al., 2004, A&A, 425, L29-L32

Claudi R., Turatto M., Antichi J., et al., 2006, Proc. SPIE, 6269, 93C

Claudi R., Turatto M., Gratton R., et al., 2004, Proc. SPIE, 5492, 1351-1361

Crampton D., Ellerbroek B., 2006, IAU Symposium, 232, 410-419

Deeg H.J., Doyle L.R., Kozhevnikov V.P., et al., 2000, A&A, 358, L5-L8

Desidera S., 2006, in preparation

Dierickx P., Gilmozzi R., 2000, ESO conference and workshop proceedings, 57, 43

Dohlen K., Beuzit J.L., Feldt M., et al., 2006, Proc. SPIE, 6269, 24D

Feldt M., Turatto M., Schmid H.M., et al., 2003, ESA Publication Division SP-539, 99-107

Fischer D., Valenti J, Marcy G.W., 2004, IAU Symposium, 219, 29F

Fridlund C.V.M., 2000, IAU symposium, 202E, 113F

Fusco T., Petit C., Rousset G., et al., 2006, Proc. SPIE, 6272, 17F

Gisler D., Schmid H.M., Thalmann C., et al., 2004, Proc. SPIE, 5492, 463-474

Holman M.J., Wiegert P.A., 1999, AJ, 117, 621

Hough J.H., Lucas P.W., 2003, ESA Publication Division SP-539, 11-17

Jenkins, J.M., Doyle, L.R., 2003, ApJ, 595, 429-445

Lane, R.G., Glindemann, A., Dainty, J.C., 1992, Waves in Random Media, 2, 209

Laws C., Gonzalez G., Walker K.M., et al., 2003, AJ, 125, 2664

Lenzen R., Hofmann R., Bizemberger P., et al., 1998, Proc. SPIE, 3354, 606-614

Lineweaver C.H., Grether D., 2003, ApJ, 598, 1350

Marcy W.G., Cochran W.D, Mayor M., 2000, Protostars and Planets IV Conf., 1285M

Maréchal A., 1947, Rev. d'Opt., 26, 257

Marois C., Doyon R., Racine R., et al., 2000, PASP, 112, 91-96

Marois C., Phillion D.W., Macintosh B., 2006, Proc. SPIE, 6269, 114

Mayor M., Queloz D., 1995, Nature, 378, 355

McArthur B.E., Endl M., Cochran W.D., et al., 2004, ApJ, 614, 81-84

McCarthy P.J., 2006, IAU Symposium, 232, 420-428

Monnet G., Gilmozzi R., 2006, IAU Symposium, 232, 429-431

Mouillet D., Lagrange A.M., Beuzit J.L., et al., 2004, ASP Conference Proc., 321, 39

Mugrauer M., Neuhäuser R., Günther E., et al., 2004, Science with Adaptive Optics, 158

Nisenson P., Papaliolios C., 2001, ApJ, 548, L201:L205

Okamoto Y.K., Kataza H., Honda M., et al., 2004, Nature, 431, 660

Perryman M.A.C., 2000, Report Progress in Physics, 63, 1209

Povel H.P., 1995, Optical Engineering, 34, 1870

Povel H.P., 1998, in Astronomische Gesellschaft Meeting Abstracts, 7-+

Racine R., Walker G.A.H., Nadeau D., et al., 1999, PASP, 111, 587, 594

Roddier F., 1981, Progress in Optics, 19, 281-376

Roddier F., Gilli J.M., Lund G., 1982, J. Opt., 13, 263-271

Rosenthal E.D., Gurwell M.A., Ho P.T.P., 1996, Nature, 384, 243

Saar S.H., Butler R.P., Marcy G.W., 1998, ASP Conference Series, 154, 1895S

Sackett P.D., 1999, Planets Outside Solar System Conf., 189S

Santos N.C., Bouchy F., Mayor M., et al., 2004a, A&A, 426, 19-23

Santos N.C., Israelian G., Mayor M., 2004b, A&A, 415, 1153

Schneider J., 2003, EAS Publication Series, Vol.8, 1-15

Seager S., 2003, Earth and Planetary Science Letters, 208, 113-124

Seager S., Sasselov D.D., 1998, ApJ, 502, 157

Soderblom D.R., Mayor M., 1993, AJ, 105, 226

Sparks W.B., Ford H.C., 2002, ApJ, 578, 543-564

Spergel D.N., Kasdin J.N., Vanderbei R.J., et al., 2002, AAS, 201, 2104S

Stam D.M., Hovenier J.W., Waters L.B.F.M., 2004, A&A, 428, 663-672

Stevens I.R., 2004, MNRAS, 356, 1053-1063

Sudarsky D., Burrows A., Pinto P., 2000, ApJ, 538, 885-903

Telesco C.M., Fischer R.S., Wyatt M.C., et al., 2005, Nature, 433, 133

Trimble V., 2004, Bull. Astr. Soc. India, 32, 87-98

Udalski A., Szymański M.K., Kaluzny J., et al., 1993, Acta Astronomica, 43, 289U

Udalski A., Szymański M.K., Kubiak M., et al., 2004, Acta Astronomica, 54, 313U

Udry S., Mayor M., Santos N.C., 2003, A&A, 407, 369

Vidal-Madjar A., Désert J.M., Lecavelier des Etangs A., et al., 2004, ApJ, 604, L69-L72

Wolszczan A., 1997, ASP Conference Series, 119, 135

Wolszczan A., Frail D.A., 1992, Nature, 355, 145

Yaitskova N., Dohlen K., Dierickx P., 2003, Proc. SPIE, 4840, 171-182

Zapatero Osorio M.R., Béjar V.J.S., Martín E.L., et al., 2000, Science, 290, 103-107

Zuckerman B., Song I., Bessell M.S., et al., 2001, ApJ, 562, 87

I would like to express my gratitude, at this point, to a large number of people who helped me in these three and a half years in Heidelberg. Life has been not always easy and there were, for me, many things to learn before concluding this thesis. Of course, this would have not been feasible if I was alone.

First of all, I want to thank my supervisor Prof. Thomas Henning and my direct "boss" Dr. Markus Feldt, for the constant help during my PhD research. A special thank to Prof. Reinhard Mundt, Prof. Ralf Klessen and Prof. Bernd Jähne for reading and making comments about this thesis. Thanks also to all the people here at the Max-Planck-Institute for Astronomy who continuously tried to answer to my questions and to lead me out of the problems. I cannot forget then all the colleagues in Europe who worked and work today at the CHEOPS and SPHERE projects, in particular I want to cite here Prof. Raffaele Gratton in Padua Observatory for introducing me to the search for extrasolar planets, together with Dr. Silvano Desidera and many others, when I was still a student at the university. Many thanks particularly to my office mates, and to all the students here at the MPIA, with my best wishes for their work and life.

Then, I am impressed by the number of friends that I have met in these years in Heidelberg. Some of them have been present from the beginning and they are still here; others stayed in Heidelberg only for a short time, but I can't forget them; others again are just entered in my life in the last months and are still on my side. I really want to thank all of them, for the great time we had together (and we will have in the future). I don't want to make a list of names, as I told they are many; but in my mind I don't forget anybody of them.

Great thanks to my oldest friends in Italy, because they still would like me to return at home (I hope). Actually I don't know when I will be back, but please wait a little more! Then I remember with pleasure all the people I met during my travels around the world, whom I promised I will visit them again sooner or later. The promise is still valid! Going back to Heidelberg, I want to thank at this point Mr. Horst Tritz, for his extremely kind help during the difficult moments.

A big hug to my marvelous family, that is always present, even if it is eight hundreds kilometers away: my father Gigi, my mother Isa, my brother Luciano, my sister Valeria. Then my grandmother, my uncles and my cousins: thanks to everybody to be a part of my life. A great part of my life.

Thanks God, who made me a good person.

*Alessandro